New Insights Into the Structure of Neutron Rich Nuclei ^{157}Sm, ^{163}Gd, and ^{163}Tb

By

Christopher Jason Zachary

Dissertation

Submitted to the Faculty of the

Graduate School of Vanderbilt University

in partial fulfillment of the requirements

for the degree of

DOCTOR OF PHILOSOPHY

in

Physics

May 10, 2019

Nashville, Tennessee

Approved:

J. H. Hamilton, Ph.D.

A. V. Ramayya, Ph.D.

R. F. Haglund, Ph.D.

S. A. Umar, Ph.D.

To my family, teachers, and friends who fueled my interest in physics,

To my advisors who made that interest into a profession,

and

To all who have continued beyond failure, unwilling to give in or suffer defeat.

ACKNOWLEDGMENTS

If you are reading this you are likely aware that one does not simply receive a doctorate. Fortunately, it is rare that one sets out to achieve this or any like goal and does not have some kind of support for their efforts, and I must say that I have received quite a lot of assistance in attaining my goals. Specifically, I would like to recognize those people and organizations without whom I would never have attained this doctorate and point out those simple interactions and basic respect that enabled me to succeed where previously I had failed. While my pursuit of physics has been a long one, the path that led me to this program began with my work at K&S Associates. I would like to thank all of the people at K&S, from the day I accepted a position working in their lab, they were supportive of me and my career as a whole and allowed me the flexibility of schedule and access to equipment I needed to enhance my career. When I decided it was time to continue beyond my last attempt at a doctorate, I contacted Professor Lloyd M. Davis of the University of Tennessee Space Institute. He took the time to meet with me and consider how having failed before in the effort to obtain a doctorate one should proceed. Upon the recommendation of Professor Davis, I turned to the Department of Physics and Astronomy of Middle Tennessee State University. There I studied to build a more complete background in physics, electronics and scientific programing with Professors R. Henderson, D. Erenso, and E. Klumpe. All the while K&S demonstrated full support of my continued education and allowed me to use equipment in their lab to complete electronics lab work as part of my classes at MTSU.

It was during my time studying at MTSU, while working at K&S, that at a company outing I was introduced to my friend and masters program mentor Professor Michael Stabin. It was his persistence on my coming to study at Vanderbilt University in the Health Physics program that eventually brought me to Vanderbilt's Department of Physics and Astronomy. Even at this point, I was still inclined to pursue my doctorate at UTSI, having previously failed to gain admittance to the Vanderbilt Ph.D. program. I did not consider that I would

ever make it as far as I have. Again, a small effort on the part of professor Davis assured me that a masters degree from Vanderbilt University would not harm my pursuit of a doctorate.

Once again in graduate school there were more than a few hurdles to overcome. Professor Stabin made it possible for me to begin work on some of the physics doctorate core courses as part of my masters in health physics. He also enabled my transition into the physics Ph.D. program prior to completion of the health physics masters, which shortened my time in graduate school by a year.

However, before this transition could be enacted I needed an advisor. I found in Professors Joseph Hamilton and Akunuri Ramayya advisors that went well beyond making my transition to doctoral studies possible. Professors Hamilton and Ramayya treated me like a research colleague and helped me build the skills that I would need both as a professional physicist and to complete my Ph.D.

Now at last in the Ph.D. program at Vanderbilt university, with some of the core courses already completed as part of my time in the masters program, I had the chance once again to pursue my doctorate. What is more, I was at last in the program that was my first choice but I had previously failed to gain admittance some six years prior. Before me still remained the core courses and qualifying examination, prospects that caused more than one fit of panic and many nights of lost sleep, yet thanks to my studies at MTSU and the excellent lectures and class structure of Professors N. Tolk, J. Velkovska, S. Umar, and V. Oberacker I had finally succeeded in the study of advanced physics where before I had failed. Furthermore, with the guidance of Professors Hamilton and Ramayya I made it through my qualifying examination.

Since then Professors Hamilton and Ramayya and their post doctoral research colleague Enhong Wang provided countless consultations on the progression of my studies and my skills as a researcher. Their colleagues in the field at research institutes around the globe provided further support and I would like to thank some of them by name; Professor Gurgen Ter-Akopian for having me out to the JINR in Dubna Russia to work with him and his

research group; Krysztof Rykaczewski at ORNL for the opportunity to participate in the work with MTAS and his colleague Charlie Rasco who answered any questions I had no matter how trivial they may have seemed to me; Robert Grzywacz of UTK for the chance to work with the VANDLE array and Stanley Paulauskas for answering my many questions during the assembly of VANDLE; Michael Carpenter and Shaofei Zhu who welcomed me and the Vanderbilt group to Argonne National Laboratory to discuss future work at the facility there; and Brooks Musangu and Jonathan Eldridge who have shared these most recent years in the lab as fellow graduate students.

As I write this it is the end of my sixth year in graduate studies at Vanderbilt University. More than eight years have passed since I started work at K&S Associates accepting their offer of employment and their support of my ongoing education. I have been fortunate throughout this journey and been treated as a professional and an equal, and this has made all the difference. The people of MTSU and Vanderbilt treated me as though I belonged at their universities, those at UTSI provided me crucial council even though I never joined their student body, and the many research colleagues in the field always welcomed my questions. Having now twice attempted a doctorate I can tell you this, if you want your students to succeed, treat them as though they already have. The persons I have mentioned here have demonstrated clearly to me how I should behave should I want to see those around me succeed, and they have instilled in me the confidence to know that I will.

TABLE OF CONTENTS

LIST OF TABLES

LIST OF FIGURES

Chapter 1

Introduction

For the study of nuclear structure, the neutron-rich region near mass number A≈160 has been, and will continue to be, a region of great interest. As the number of nucleons increases beyond the closed shell values of 82 neutrons and 50 protons, the nuclear shape becomes steadily more deformed until a rapid onset of deformation occurs around N = 88-90 [1]. A similar region of rapid deformation centers around A≈100 with a sudden shift in deformation near N=60 [1]. This work now is the continuing effort to provide structural information for the ongoing study of the onset of deformation.

Detailed structural information for large cohorts of nuclei is central to the study of nuclear deformation, as accurate descriptions of the nuclear forces need multiple observations of similar states to confirm or deny their veracity. Appendix A contains material discussing a number of efforts to describe the source of the rapid onset of deformation in the A≈100 and A≈160 regions. These works are examples of how detailed nuclear structural analysis enables the growth of our understanding of nuclear physics.

Another example of applications of structural information in the A≈160 region comes from the field of nuclear astrophysics. As a part of the explanation for the mass distribution of elements in the universe, the r-process of nucleosynthesis endeavors to explain a number of peaks, in extremely neutron rich environments and accounts for about half of the heavy nuclei in the solar system [2, 3]. Several prominent features of the nuclear mass distribution are the peaks located near nuclear magic numbers corresponding to shell closures. Early models of the r-process have met with reasonable success by aiming their efforts at reproducing shell closure peaks. A feature that is drawing attention as a means of clarifying our understanding of the r-process is the smaller, rare earth element peak, illustrated in Figure 1.1, which corresponds to maximum nuclear deformation in the mass A≈160 re-

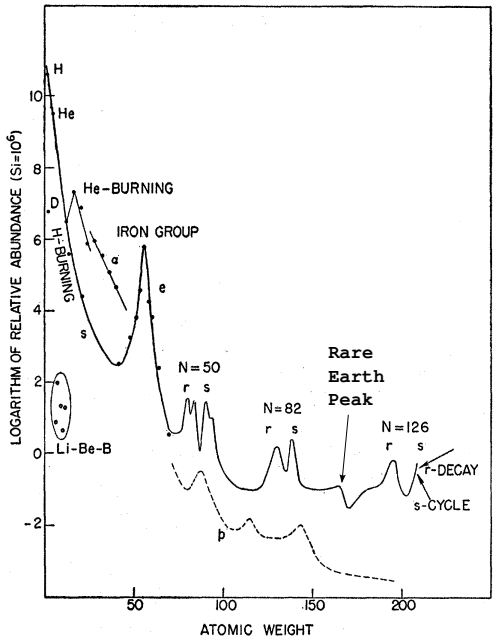

Figure 1.1: Plot of element abundance in the solar system, reproduced from Burbidge, *et al.* [2]. Peaks attributed to the r-process and s-process marked with an r or s, respectively. Arrow indicating the rare earth peak added for this work.

gion. Nuclear astrophysicists see this as an additional probe into r-process nucleosynthesis by incorporating nuclear input into their models intent upon reproducing this component of the mass distribution [4]. Thus, calling for further structure studies in the A$\approx$160 region as nuclear astrophysics models turn to studying the role of nuclear deformation in the formation of the rare earth element peak.

Crucial to progressing the application and confirmation of nuclear models, however, is clear identification of the model predicted states. It is this clear identification of states that is detailed in the next Chapters 3, 4, and 5 for the ground states and low-energy band structures of the isotopes ^{163}Gd, ^{163}Tb, and ^{157}Sm. This information provides the foundation of a more complete structure of these isotopes and provides further systematics for isotopes in this mass region. Chapter 2 will detail those principles of nuclear physics needed to facilitate discussion topics. Furthermore, systematic studies, such as incorporating nuclear input into r-process models, benefit from complete information across the mass region. The final

chapter will describe an upcoming project which will further the study of nuclear structure in the A$\approx$160 region.

Of special interest in this mass region is the isotope ^{163}Gd. Previous investigations in the doctoral thesis of Brewer [5] yielded structural anomalies, assigning several low-energy transitions to be competing with high-energy transitions at intensities greater than could be described theoretically. Brewer suggested a thorough evaluation of the relative intensities of these low-energy transitions prior to publication. In the course of performing the intensity analysis suggested by Brewer, the present findings identified a new structure for ^{163}Gd resolving the previously observed structural anomalies. The process by which the new structure was evaluated and the differences with previous findings are discussed in Chapter 3.5.

Chapter 2

Concepts in Nuclear Physics

While the majority of this work is dedicated to the experimental methods employed and the interpretation of nuclear structure based upon the experimental data, there are a few concepts of nuclear physics which are fundamental to this work and are addressed here. Discussion of the shell model and collective states, as well as reduced transition probabilities, follow the topics discussed in the nuclear structure appendix for Firestone's Table of Isotopes reference text [6].

2.1 Descriptions and Observables of the Nucleus

2.1.1 Shell Model

Early observations of nuclei by Elsasser and Mayer found increased nuclear stability for specific numbers of neutrons and protons [7, 8], nuclear magic numbers. Mayer and Jensen later detailed a nuclear shell model that described the arrangement of nucleons within the nucleus according to a spherical potential well. The typical potential, $V(r)$, used is that of a harmonic oscillator of the form [9]:

$$V(r) = -V_0[1-(r/R)^2] \tag{2.1}$$

where r is the distance from the center and R is the radius of the nucleus. The quantum states yielded by this potential can be characterized by, n, the principal quantum number such that each state has $n-1$ radial nodes, and by the orbital angular momentum l. In keeping with the metric from atomic spectroscopy the l terms $l = 0,1,2,3,...$ have been designated as $s,p,d,f,....$ Thus, states can be identified as $1s,1p,1d,2s,1f,...$ Solution of the Schrödinger equation for the potential $V(r)$ will then yield energy levels which are

degenerate in steps of $2(n-1)+l$ with states of a given energy with either all even l values or all odd l values. Later Mayer [10] and Haxel, *et al.* [11] demonstrated that spin orbit interactions would split orbitals into substates of $l \pm 1/2$ reducing the degeneracy and reproducing the nuclear magic numbers.

The development of the shell model made a significant step in describing nuclear structure, well describing the role of quantum mechanical principles in describing the origin of nuclear magic numbers. However, as the number of nucleons moves away from the magic numbers a spherical shell model ceases to accurately describe their level spacing.

2.1.2 Collective Model

In an effort to describe the nucleus away from the nuclear magic numbers, Rainwater [12] proposed the polarization of the even-even nuclear core by the motion of the odd nucleon in odd-A nuclei. This polarization would result in collective motion within the nucleus giving rise to static electric quadrupole moments, enhancing electric quadrupole (E2) transition rates.

Bohr and Mottelson developed the collective model [13] to describe the structure of spheroidal nuclei far from nuclear spherical shell effects. The description is that of nuclei with stable deformation because of collective interaction of nucleons beyond the last even-even closed shell with a deformed nuclear field. These spheroidal nuclei have equilibrium shape of either prolate or oblate. The nucleus in such a deformed state with moment of inertia $\mathscr{I}$ can undergo rotational motion about an axis perpendicular to the axis of symmetry with angular momenta of $0^+, 2^+, 4^+, 6^+...$ and energies of $E_R = \frac{\hbar^2}{2\mathscr{I}} I(I+1)$ to the first order. The collective excitations of the nucleons outside the even-even core give rise to two vibrational modes referred to as β and γ vibration modes, where β vibration is the oscillation of the nuclear shape along the axis of symmetry and γ vibration is the oscillation of the nuclear shape resulting in deviations from cylindrical symmetry. These band heads can undergo rotational motion leading to states with $0^+, 2^+, 4^+...$ for the β band and

$2^+, 3^+, 4^+, 5^+, 6^+$... for the γ band. A graphical representation of these vibration modes is demonstrated in figure 11.17 of Yang and Hamilton's text [14].

Of specific interest to this work is the γ vibrational mode proposed under the collective model. Two collective bands observed in ^{165}Dy, the nuclear analog to ^{163}Gd, have been proposed to be γ vibrational bands.

2.1.3 Deformed Shell Model

Nilsson and Mottelson continued the development of models for proton and neutron single particle states in deformed nuclei with the deformed shell model. This model breaks the degeneracy of states observed in the shell model by deformation of the potential, giving rise to the following additional quantum numbers as detailed in [6]. K, the projection for the total angular momentum J onto the nuclear symmetry axis, N, the total oscillator shell quantum number; n_z, the number of oscillator quanta in the z direction; M, the projection of J onto the laboratory axis; R, the angular momentum from the collective motion of the nucleus; Ω, the projection of total angular momentum j (orbital l plus spin s) of the odd nucleon on the symmetry axis; and Λ, the projection of angular momentum along the symmetry axis where $\Omega = \Lambda + \Sigma$ and Σ is the projection of intrinsic spin along the symmetry axis. Levels are labeled by the asymptotic quantum numbers $\Omega^{\pi}[Nn_z\Lambda]$. The deformed shell model can be used to produce Nilsson level diagrams, Bengtsson and Ragnarsson [15], over a range of nucleons and deformations. Figures of these Nilsson level diagrams from [6] have been reproduced within this work for the reader's convenience in Figures 2.1, 3.5, and 3.13.

Since the development of the deformed shell model it has been implemented by numerous studies to investigate deformation of the nucleus, see Appendix A for discussion of some examples. Some terminology important to the discussion both in Appendix A and Chapter 5 are the terms "intruder" and "extruder" states. Intruder states are those states which originate above the next shell gap from where the ground state of the nucleus in

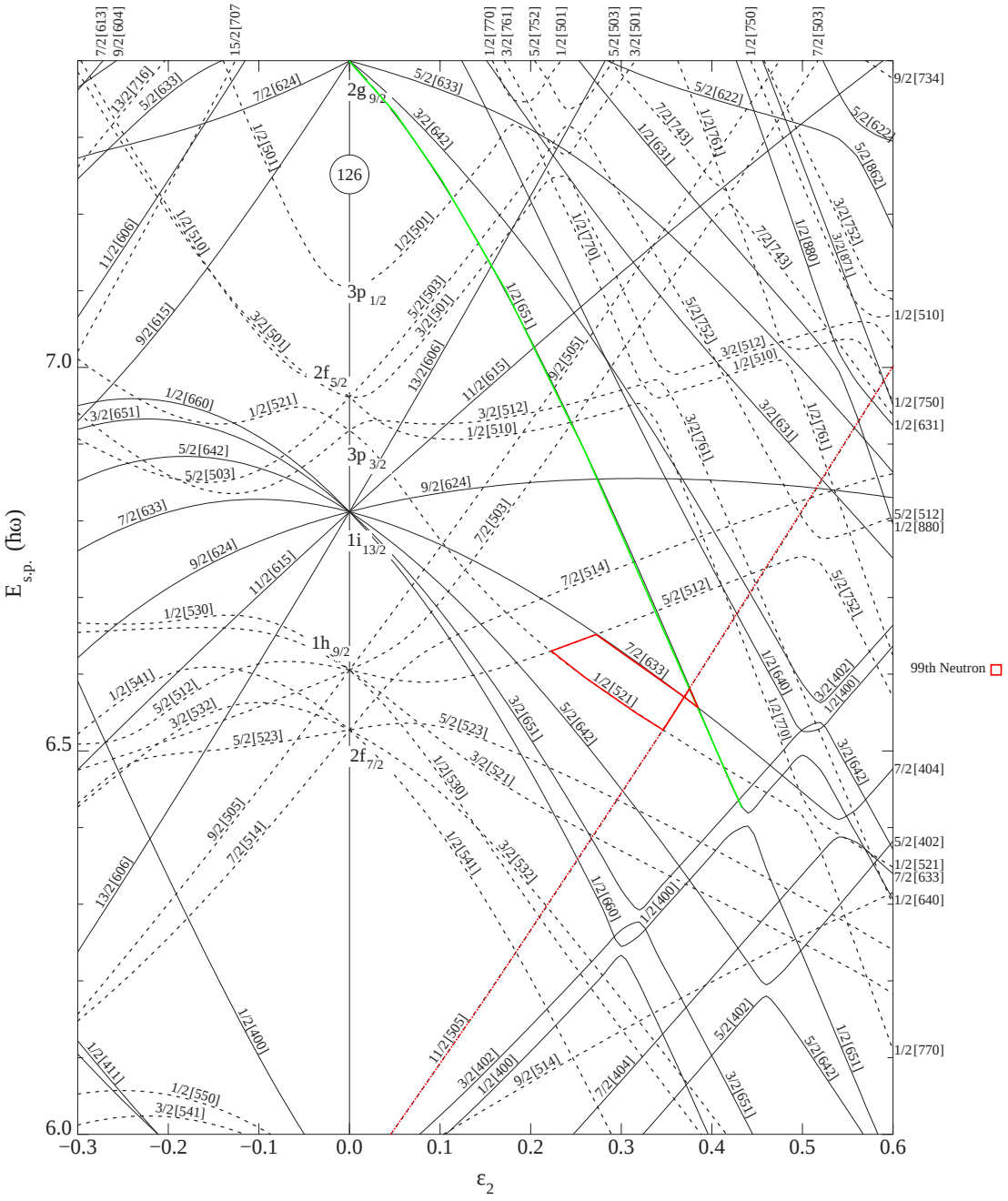

Figure 2.1: Nilsson Levels for Neutrons, $\varepsilon_4 = \varepsilon_2^2/6$, with an example of an intruder state marked in green, example of an extruder state marked in red, and a possible location for the 99th Neutron for a deformation near $\varepsilon_2 \approx 0.3$ labeled. Reproduced from [6].

question is located. Extruder states are those states which originate below the previous shell gap from where the ground state of the nucleus in question is located. Although, the extruder state term is less commonly used and typically both of these descriptions are often referred to as intruder states. In Figure 2.1, the $\nu g_{9/2^+}[651]$ is an example of an intruder state for an even-odd nucleus with 99 neutrons and deformation near $\varepsilon_2 \approx 0.3$, which may have a ground state near the $\nu p_{3/2^-}[521]$ level, and the $\nu h_{11/2^-}[505]$ level is an example of an extruder state for the same nucleus.

2.2 Nuclear Decay

Throughout this work, three forms of nuclear decay are implemented to study nuclear structure. The nature of these processes provide observables to enable study of the nuclear structure and the physical qualities unique to each of these decay modes provide context within which observations can be understood. Here a brief description of these three decay modes, β-decay, γ-decay, and spontaneous fission, is given.

2.2.1 Nuclear β Decay

The process of nuclear β decay is one of the three earliest known forms of radioactive decay. It is via the β-decay process that nuclear isotopes that lie above or below the line of stability convert either protons to neutrons, or neutrons to protons. The proton to neutron mode is known as β^+-decay and the neutron to proton mode is known as β^--decay. The energy released in β^--decay corresponds to the mass difference between the parent and daughter nucleus according to:

$$Q = [m_N({}^A_Z X) - m_N({}^A_{Z+1} X') - m_e - m_{\overline{\nu}_e}]c^2 \tag{2.2}$$

This quantity of available energy in β-decay is known as the Q value. So long as the Q value remains small the isotope in question is stable against β-decay. Following decay,

the energy is distributed between excitation of the daughter nucleus, kinetic energy of the electron, and kinetic energy of the electron anti-neutrino. All the nuclei studied in this work lie on the neutron rich side of the line of stability and are thus unstable to β^--decay. In this form of β-decay, the nucleus converts a neutron to a proton ejecting an electron and an electron anti-neutrino as described by:

$$ {}^{A}_{Z}X \rightarrow {}^{A}_{Z+1}X' + e^- + \overline{\nu}_e \tag{2.3} $$

For β-decay the portion of the Q value which goes to excitation of different states in the daughter nucleus is strongly determined by the change of angular momentum and parity during β-decay, which follows conservation of angular momentum. Thus, any angular momentum carried away by the electron and electron anti-neutrino must either cancel out or produce a change in the angular momentum state of the daughter nucleus. The majority of β-decay events follow either the Fermi or Gamow-Teller transition resulting in conservation of parity and with change in angular momentum, noted in this work by $\Delta I = X$, according to:

$$ \text{Fermi decay:} \qquad \Delta I = 0, \qquad \text{including: } 0^+ \rightarrow 0^+ \tag{2.4} $$

$$ \text{Gamow-Teller decay:} \qquad \Delta I = 0, \pm 1, \qquad \text{excluding: } 0^+ \rightarrow 0^+ \tag{2.5} $$

There are significantly less likely cases in which more than one unit of angular moment is carried away, and/or there is a change in the parity between nuclear states. These transitions are referred to as forbidden transitions, with an order corresponding to how unlikely the transition is. For the purpose of this work it is not anticipated that any transitions of forbiddeness greater than first-forbidden is observed. First-forbidden transitions correspond to those with $\Delta I = 0, 1,$ or 2 and a change of parity.

2.2.2 Nuclear γ Decay

Another mode of decay is that of gamma decay, a process by which the nucleus transitions from a state of a given energy excitation above the ground state of the nucleus to another state of lesser excitation. As part of this transition, the energy difference between the two states is carried off in the form of an electromagnetic wave or photon. As this is an electromagnetic process, these gamma rays, photons which originate from a nucleus, can carry away different amounts of spin and parity that define the multipolarity of the transition. Observation of these γ-rays provides explicit information regarding the relationship between different states within the nucleus.

Important to the study of nuclear structure via γ-ray spectroscopy is the reduced transition probability, which is the comparison of observed γ-ray lifetimes to the theoretically calculated lifetimes assuming single particle transitions. By making the comparison, detailed in Appendix K of Firestone's Table of Isotopes [6], a measure of the collectivity of the transitions may be obtained. Furthermore, because of the relationship between lifetime and transition probability, it is possible to make use of the calculated single particle transitions, included in Figures 2.2 and 2.3, for the readers convenience, without observation of lifetime by comparison of observed relative γ-intensities from the same level. The plots in Figures 2.2 and 2.3 are calculated lifetimes of transitions of a given energy for each possible multipolarity up to ΔI=4, for both magnetic and electric multipole single particle transitions.

In the scope of this work, an ideal illustration can be found in evaluation of the relative intensities of the two transitions identified as originating from the 324.8 keV $7/2^-$ level in ^{163}Gd, a ΔI=1 115.4 keV transition and a ΔI=2 137.8 keV transition. Review of these transitions internal conversion corrected (ICC) relative intensities, according to $I_\gamma ICC = I_\gamma(1+\alpha_t)$ for total internal conversion correction, shown in Table 3.1, shows that the two transitions, 115.4 keV with I_γ ICC of 58(3) and 137.8 keV with I_γ ICC of 63(3), have experimentally observed intensities consistent with transitions of nearly equivalent lifetime.

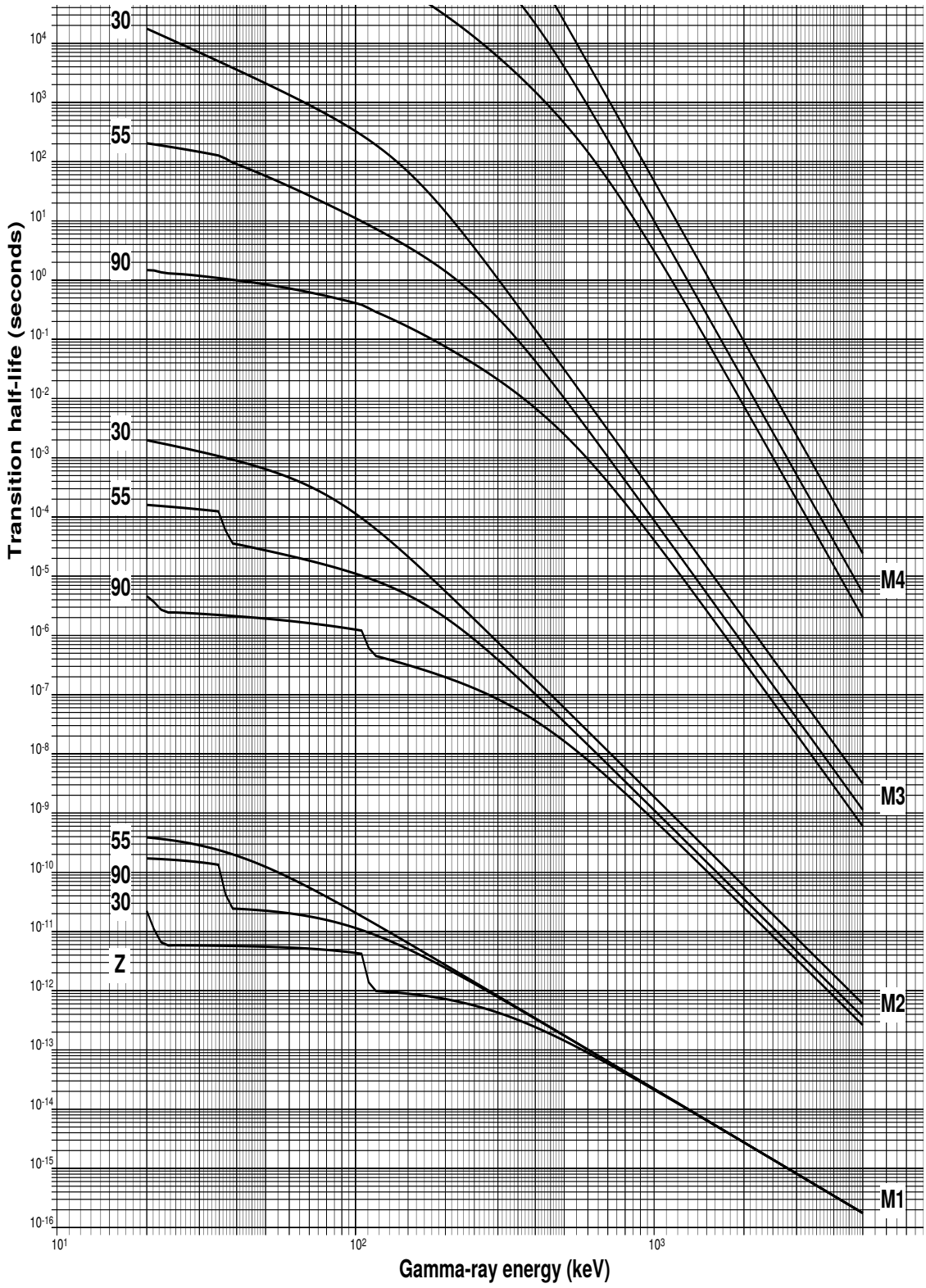

Figure 2.2: Single particle transition half-lives for magnetic transitions corrected for internal conversion. Reproduced from [6].

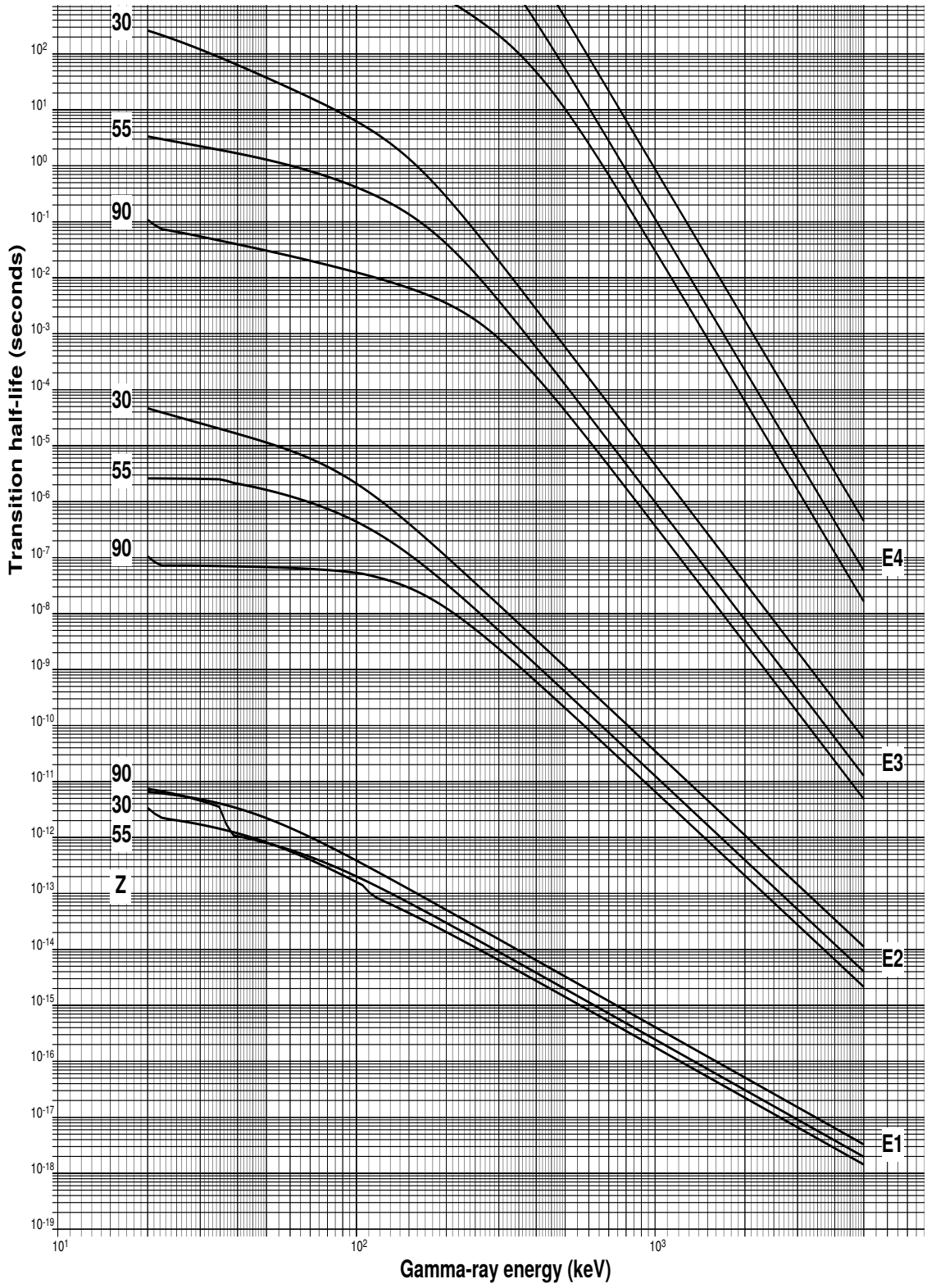

Figure 2.3: Single particle transition half-lives for electric transitions corrected for internal conversion. Reproduced from [6].

However, comparison of either possible ΔI=1 single particle transition half-life, electric or magnetic, would yield a result with significantly shorter half-life than that of either possible ΔI=2 single particle half-life. This discrepancy between the observed relative intensities and the calculated single particle relative intensities is consistent with these transitions being part of a collective rotational band as opposed to being single particle transitions.

2.2.3 Spontaneous Fission

Another form of nuclear decay observed in this study is that of spontaneous fission(SF), a decay process available only to the heaviest portion of the table of nuclides. SF results in a large release of energy and produces a wide array of nuclei in a wide range of spin excitation states. The fission process, both spontaneous and induced, is a rich dynamic process that is the subject of ongoing study, therefore the description which follows is by no means a complete description. For nuclei of sufficient mass, the SF process begins to compete with the more common α-decay mode. In the process of SF the Coulomb repulsion in the nucleus results in a split of the nucleus into two or more fragments. Immediately following the scission point, that point in the fission process where the fissioning nucleus splits into two or more separate nuclei, the primary fragments are accelerated away from each other by the Coulomb repulsion between the protons in each fragment. Simultaneously the primary fragments begin to de-excite from the highly excited state in which they are created. The first mode of de-excitation undergone is that of the more energetic neutron emission, or commonly referred to as neutron evaporation. As the excitation of the nucleus decreases, γ-ray emission becomes more competitive with that of neutron emission and eventually the nucleus is no longer excited enough to emit neutrons. At this point the fragments are referred to as secondary fragments, having now transmuted to lighter, less neutron rich nuclei. Unlike β-decay, SF populates up to very high spin states in the fragment nuclei. This makes the observation of coincident γ-ray emission following SF very effective for studying high spin states in a nucleus if high enough orders of coincidence can be observed.

Chapter 3

^{163}Gd

3.1 Experimental Methods

For the study of ^{163}Gd and ^{163}Tb, a 10 - 18 μA beam of 50 MeV protons was used to induce fission in a UCx target on a High Voltage (HV) platform to produce $^{162-165}$Eu via fission at the Holifield Radioactive Ion Beam Facility at Oak Ridge National Lab. After fission, ions were accelerated off the HV platform and were magnetically separated isobarically to provide isotopes of the desired charge over mass ratio, Q/A, to the low-energy radioactive ion beam spectroscopy station (LeRIBSS), as shown in Fig 3.1. It should be noted that some molecular ion contaminants are possible with Q/A beam selection as well as isotopes with very similar Q/A. Their effects on the analysis will be discussed in more detail in Chapter 4.3. The europium beam was implanted onto a movable tape. After a designated measurement time, the moving tape controller (MTC) would transport the accumulated source behind a shield to prevent additional background from daughter products. Then, a new source would be collected. This process of source accumulation, observation of decay, and decay product removal is referred to as the tape cycle. The MTC settings for source collection time and measurement time were varied to best allow for observation of wanted products as selected from previously measured half-lives of europium and gadolinium isotopes. These settings were for a 30s collection time and a 25s decay time. It is noticed that there is a typographical error in the tape cycle listings in reference [5]. For ^{163}Eu the half-life was measured by Osa, *et al.* [16] to be 7.7(4)s and by Sato, *et al.* [17] to be 7.8(5)s. The half-life of ^{163}Gd was measured as 68(3)s by Gehrke *et al.* [18]. In addition to the data collected with the tape cycling, a saturation measurement was made for assessment of the lifetimes of the beam constituents. This measurement was run for 46 min with the beam on and the tape stationary. Following the saturation measurement, a

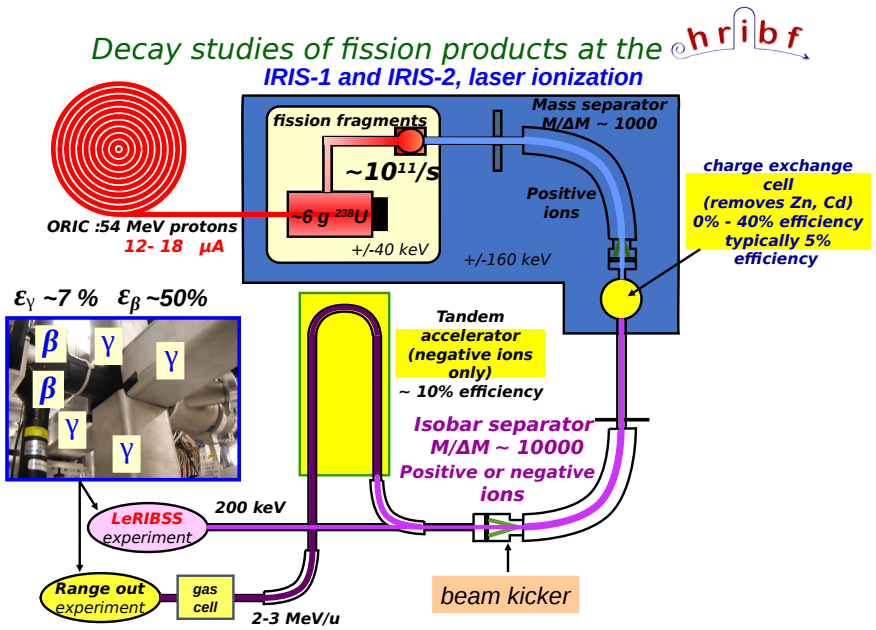

Figure 3.1: Sketch of Holifield Radioactive Ion Beam Facility Beamline and photo of the CARDS used to collect the data for this study at the LeRIBS Station. In the CARDS photo the beamline is incoming from the right. While the 4 Clover detectors are central and the β detectors are left. The CARDS setup is mobile between the Range Out Station and the LeRIBS Station. γ-ray efficiency reported is for energies near 1 MeV. Reproduced with permision of the ORNL Physics Division.

separate data file logged observations of decays from the accumulated source for 7 min.

The detector array included a Clover array for radioactive decay spectroscopy (CARDS) that consisted of four HPGe Clover detectors, without Compton suppression, for the detection of γ-rays. The Clover detectors were oriented around the beamline adjacent to two plastic scintillators for β-ray detection, shown in Figure 3.1. The four Clover detectors were located on a single plane normal to the beamline at 90° angles between each adjacent Clover. The scintillators allowed for gating of coincident γ signals with β triggers but were of insufficient volume for β spectroscopy. Data acquisition was via digital pulse processing with Pixie16 modules according to methods detailed by Grzywacz [19]. This setup allowed for coincident analysis with γ-γ, γ-γ-β, γ-tape cycle, γ-β-tape cycle and associated projections.

Each single event was logged with detector ID, time, and energy. Data analysis was

performed with both the DAMM software [20] and tools from the RADWARE software toolkit [21] following assembly of individual data entries into coincidence data volumes with the SCAN code from the UPAK software distribution from Oak Ridge National Lab. Before a transition was incorporated into the level scheme, background subtracted, and not subtracted, coincidence spectra for that transition, and any coincident transitions, were evaluated. Background subtraction was performed at the time of creating the coincidence gate using channels both higher and lower than the gate. Coincidence spectra were assembled with the SCAN code with a 300 ns coincidence window. The window of 300 ns was selected to yield x-ray intensities of the ^{163}Tb transitions correlated to the 287.8 keV transition in ^{163}Tb. A rolling coincidence window method was employed ending a set of coincidence measurements only once a full coincidence window elapsed without further events.

In addition to background subtraction, each transition was evaluated to confirm that the coincidence spectra were not the result of Compton scatter between two of the HPGe Clover detectors. While a technique for subtracting Compton scatter from intensity measurements has been detailed by Allmond [22], the great majority of the transitions incorporated in the level schemes were not strongly contaminated by Compton scatter. Further considerations will be discussed in Chapter 3.5, page 42. Additionally, as all transitions were evaluated with background subtracted gates with background taken from both higher and lower channels, Compton scatter peaks were easily identifiable by a visual artifact in the form of a valley or recess on either shoulder of the peak.

Figure 3.2 illustrates contributions from Compton scatter and the gates used in the Compton scatter background correction method detailed by Allmond. A set of coincidence gates are used to construct a Compton scatter corrected background for a coincidence peak on a Compton scatter contour. This is in contrast to a typical background correction which is either a function fit for the entire data set and subtracted out during data compilation, or simply an equal number of channels selected from a nearby region with no coherent

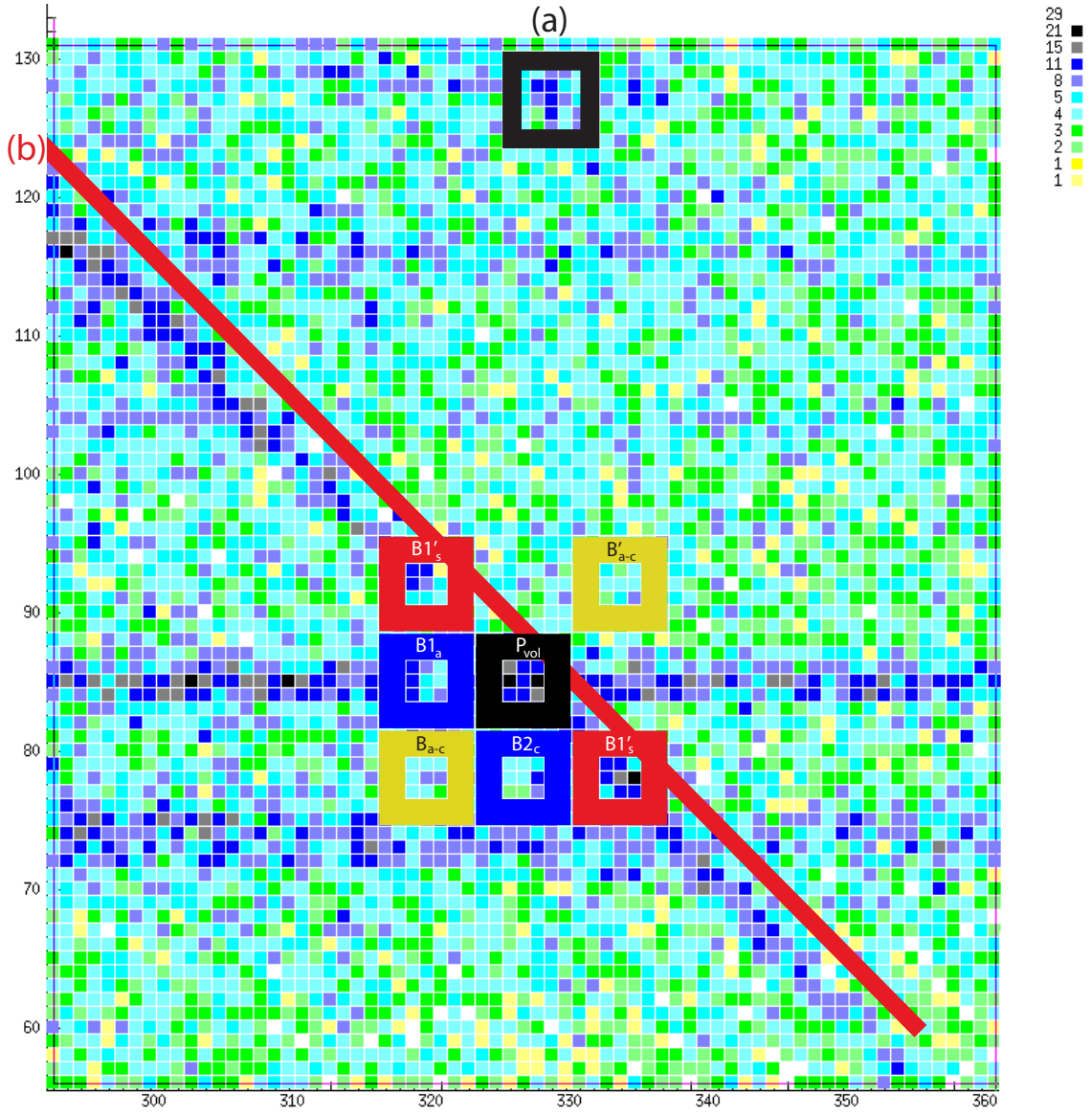

Figure 3.2: Example 2D color plot of coincidence data from the A=163 data. The black frame (a) encloses an example of a coincidence peak. The red line (b) runs adjacent to observation of Compton scatter crosstalk. The remaining frames indicate the selection areas for performing a Compton scatter background correction per Equation 3.1.

signals and subtracted as part of drawing a gated spectrum. Here a coincidence peak is the volume of the data that corresponds to both coincident signal observations. Additionally, a coincidence contour is a surface defined within the data volume of γ energy vs γ energy vs counts. In detail:

$$P_{vol} - B1_c - B2_c + B_{a-c} + \frac{(-B1'_s - B2'_s + 2 * B'_{a-c})}{2} \tag{3.1}$$

where, P_{vol} is the volume under the coincidence peak, Bn_c are backgrounds for each of the separate coincident γ-rays, Bn'_s are backgrounds taken from the Compton scatter band both higher and lower than the coincident peak. B_{a-c} & B'_{a-c} are anti-coincident backgrounds selected from nearby regions not coincident with either γ-ray of interest.

This method removes both the coincident background and the Compton background and replaces anti-coincident, non-Compton scatter background. Figure 3.2 illustrates the areas selected as part of this correction method. For general analysis, this background correction method was not needed on most of the peaks in these data, only for those peaks who lay in a region of the coincidence surface which was underpinned by a strong Compton scatter contour and only for confirmation that the peak was not an artifact of the experimental setup. At the end of the re-evaluation it was found that few of the transitions investigated had significant contamination related to Compton scatter.

Shown in Figure 3.3 is an example of spectra used for discovery and confirmation of new transitions. In frame (a) three valleys in the data are indicated by the marker (1). These are brought about by the fact that peaks caused by Compton scatter ”walk” and thus result in over subtraction before and after a peak due to Compton scatter. In frame (b) the marker (2) highlights several common background peaks. Lastly, in frame (b) the marker 3 highlights a peak with ideal background, lacking in Compton scatter or any other coincident peak.

Furthermore, evaluation of the decay rate of a given transition within the tape cycle window was used to clarify the genesis of the transition. Shown in Figure 3.4 we see the

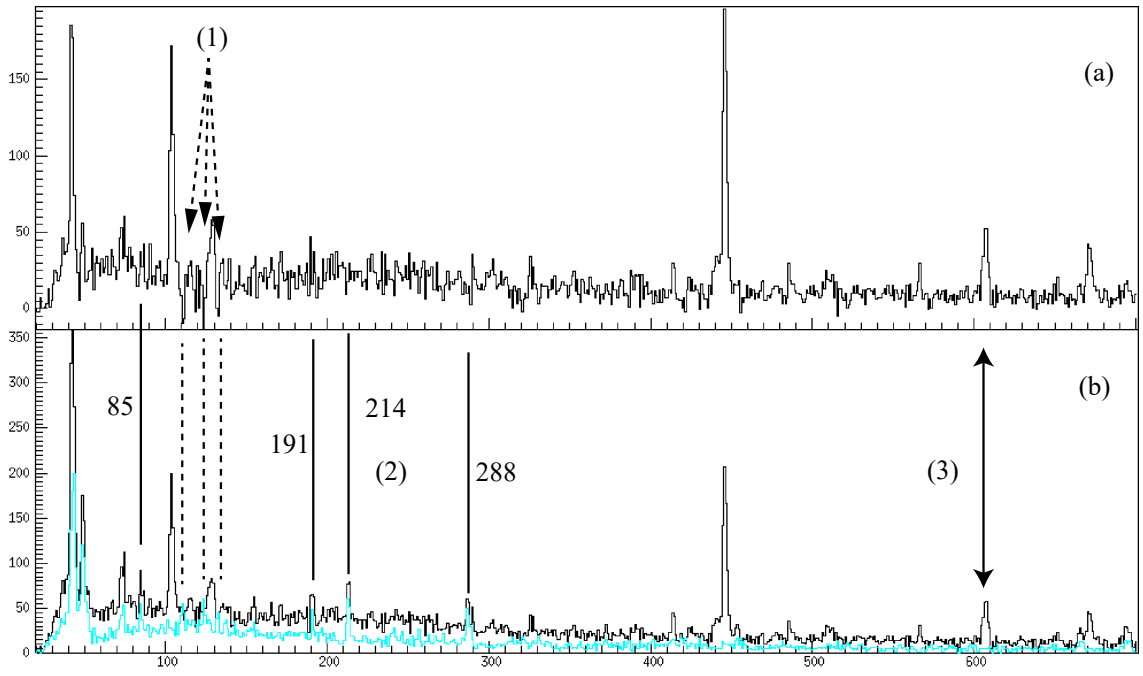

Figure 3.3: Example of background correction using a gate on the 85 keV ^{163}Gd transition. Frame (a) is a gate on channels 84 and 85 less the content of channels 80 and 89. Frame (b) shows the gate on channels 84 and 85 along side the sum of channels 80 and 89.

decay curves for transitions from ^{163}Tb, ^{163}Gd, and background. This method of decay analysis was used visually to resolve transitions from isotopes with significant differences in half-lives.

Over the course of the data analysis, the gating methods and relative intensity methods were written into command files to allow easy repetition of previous analysis. A command file detailing the specific channels for gate and background was written for each individual gate which was relevant to the analysis of the structure for both ^{163}Gd and ^{163}Tb. Additionally, relative intensity measurements were performed via command files allowing the exact fit that was made initially to be repeated at a later date in the event that more transitions were found that needed to have intensity measurements made. While these command files are simple, they proved to be a formidable tool for data analysis preserving the exact spectra that were used for each step along the analysis process. Example command files are included in Appendix B.

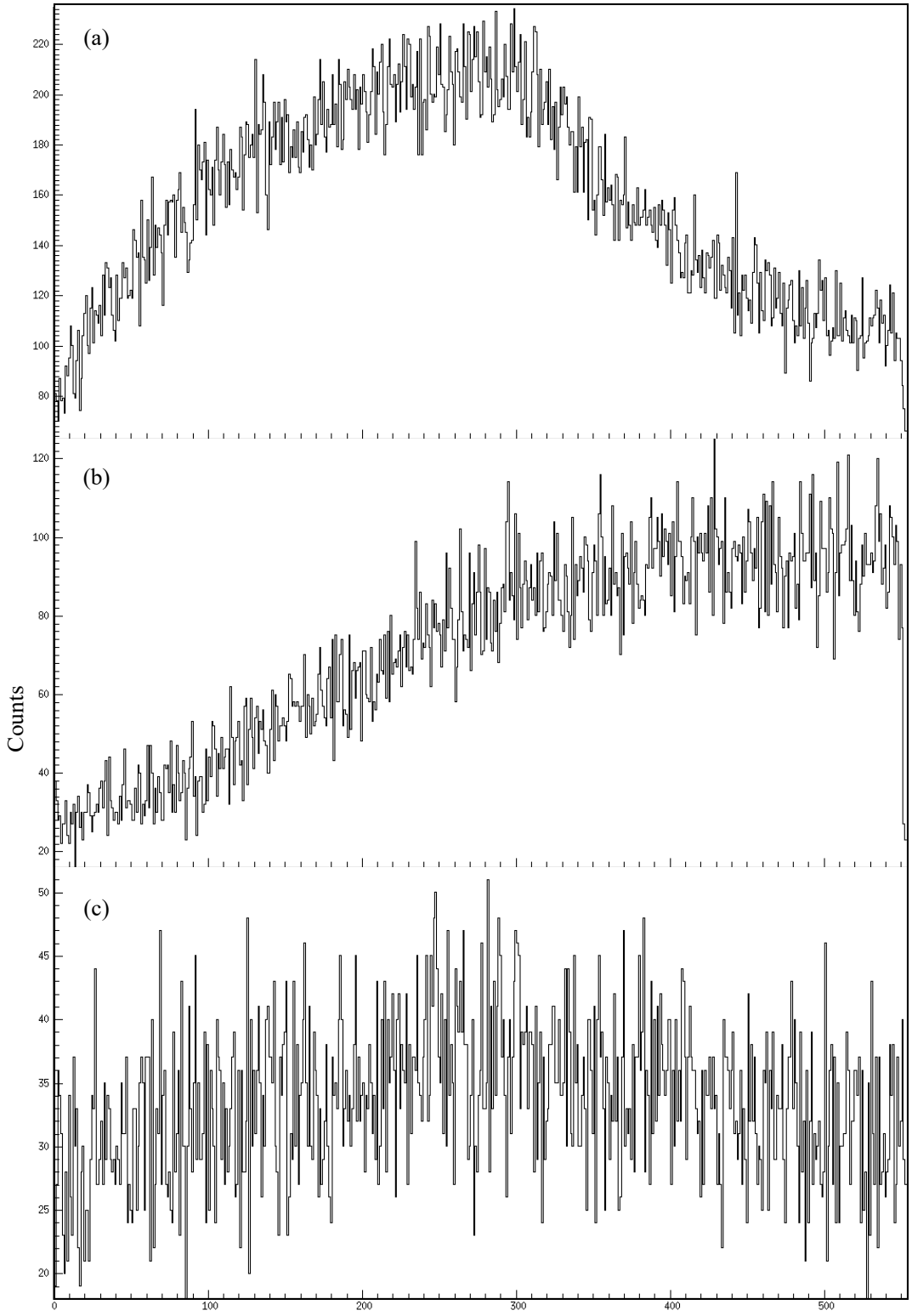

Figure 3.4: Examples of ^{163}Gd growth and decay, ^{163}Tb growth and decay, and background in frames (a), (b), and (c) respectively. With units of thenths of Seconds on the X-axis.

Pivotal to confirmation of the level schemes presented here were the relative intensity measurements performed. Peaks were fit according to the DAMM software package FIT command. For those peaks of especially low intensities, simple sums were used with backgrounds selected from nearby representative channels. The reference peaks used were 454.2 keV and 287.7 keV for ^{163}Gd and ^{163}Tb, respectively. Peak intensities were corrected for detector efficiency via a multiple term exponential fit based upon efficiency measurements made at the time of the experiment.

3.2 Previous Findings in ^{163}Gd

The previous total absorption studies, including ^{163}Gd by Hayashi, *et al*. [23] identified the Q_β for ^{163}Gd as 3170(70) keV, and its parent isotope's, ^{163}Eu, Q_β as 4690(70) keV. A study with the JAEA-ISOL by Sato, *et al.* [17], identified 5 transitions with energies 85.8, 116, 138, 191.2, and 401 keV in ^{163}Gd without level assignment. All of the 5 previously observed transitions have been confirmed and 93(22) new transitions identified, 22 of which are tentative between 52 new levels, 9 of which are tentative.

3.3 Band Structure of ^{165}Dy

The low-energy band structure of ^{165}Dy is important in the evaluation of ^{163}Gd. Included here is a brief description of those similarly observed between the two nuclei. The Z=66 ^{165}Dy has N=99 neutrons, as does ^{163}Gd with Z=64, a closed spherical subshell. Thus, both nuclei have one unpaired neutron in the same orbit with all protons paired and so should have similar neutron single particle states. In Figure 3.5 is seen the Nilsson single particle states for neutrons. The level occupied by the spare neutron in ^{165}Dy and ^{163}Gd in their ground state is indicated, Sheline *et al.* [24] proposed the ground state of ^{165}Dy to occupy the $7/2^+[633]$ level. The study of ^{165}Dy has been carried out via β and Isomeric Transition decay studies, as well as neutron capture and tritium or deuteron transfer reactions. Shown in Figure 3.6 is a partial level scheme of ^{165}Dy based upon the level scheme from Nudat2 [25]. This partial scheme focuses on the low-energy rotational band structure of ^{165}Dy built on low-energy neutron single particle states omitting the observed high-energy single particle states.

Of particular interest in the structure of ^{165}Dy is the excitation of the $1/2^-$ band head and the lifetime of the E3 transition from that level to the $7/2^+$ ground state. At an excitation of 108.2 keV, the state has a lifetime of 1.257 min. It is expected that a similar such band head and lifetime will be observed in ^{163}Gd and is detailed at the start of the following

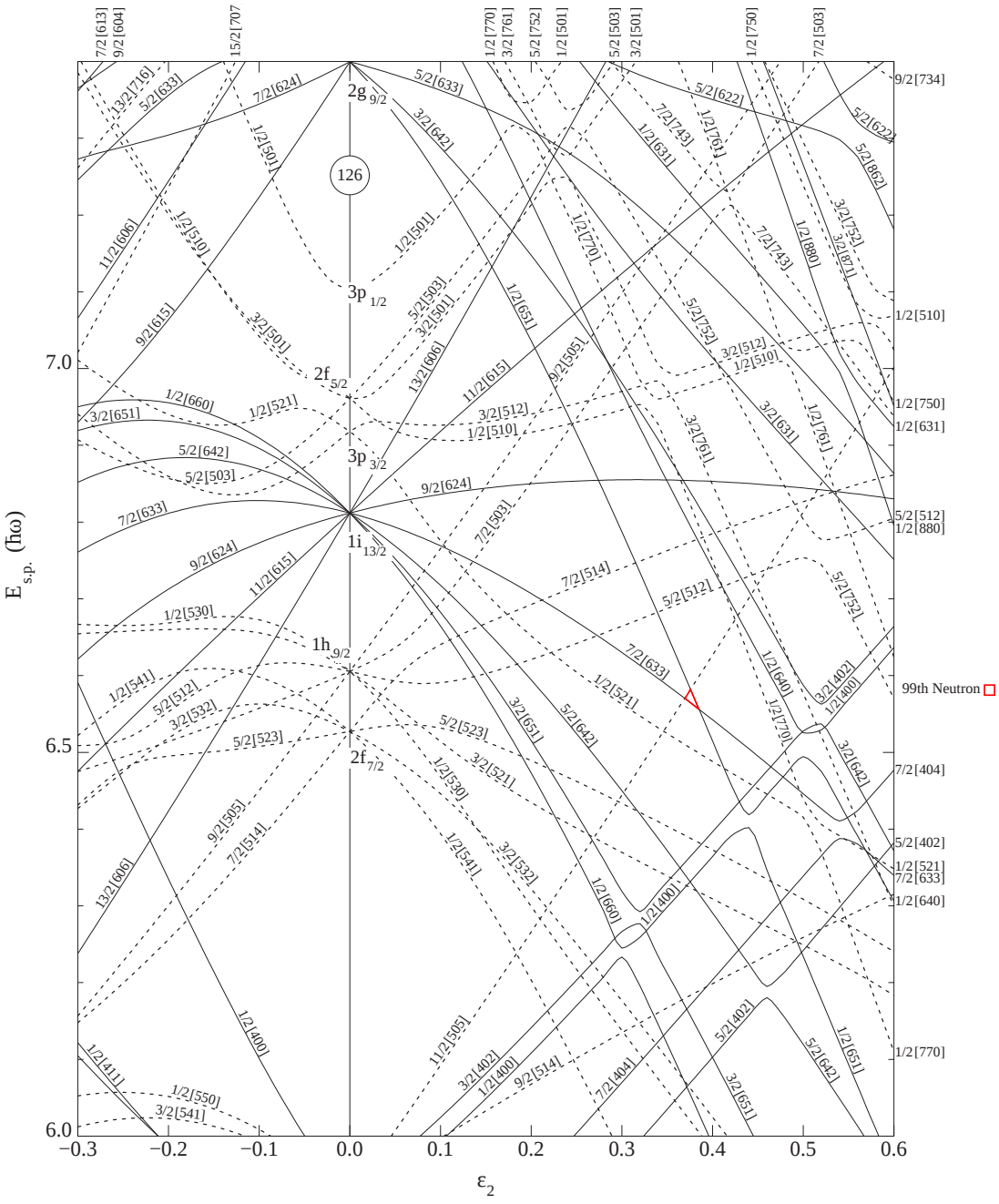

Figure 3.5: Nilsson Levels for Neutrons. Reproduced from [6].

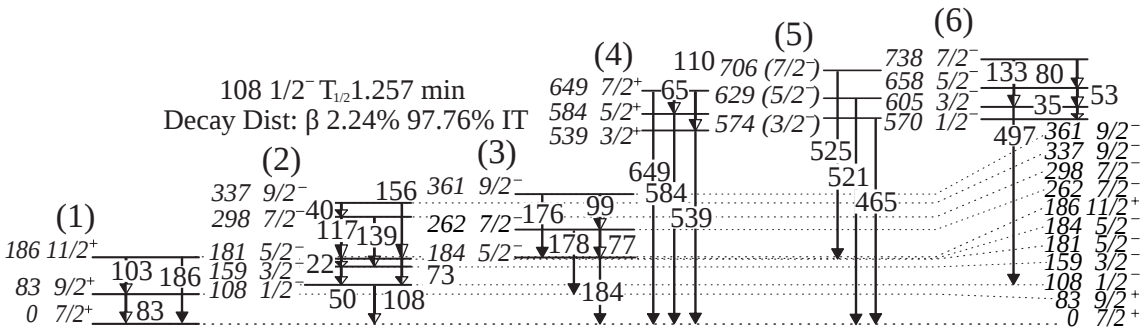

Figure 3.6: Level scheme for the low-energy band structure of ^{165}Dy.

section. Furthermore, the $3/2^+$ and $3/2^-$ band heads at 538.6 and 573.6 keV, respectively, are each postulated to be γ vibrational band heads built on the $7/2^+$ ground state and the $1/2^-$ state respectively, as described by Sheline, *et al.* [24]. The γ vibrational band in ^{164}Dy is at 761.8 keV per Shelton and Sheline's findings [26]. A final feature to note in the ^{165}Dy structure is the distinct spacing, energy difference of the first $1/2^-$ band. Here first refers to the band of a given spin with the lowest excitation for the band head. Commonality between this band and a similar band in ^{163}Gd was very useful in the analysis and will be discussed in the following section.

3.4 ^{163}Gd Results

Five transitions related to the de-excitation of ^{163}Gd were identified previously with energies of 85.8, 116, 138, 191.2, and 401 keV [23], and are observed in this work to be 85.0, 115.4, 137.8, 191.3, and 400.7 keV. These transitions were not assigned any level association at that time. These previously identified transitions and the characteristic x-rays for ^{163}Gd were used to confirm transitions associated with the de-excitation of ^{163}Gd via coincidence. The full decay scheme obtained in this work is shown in Figures 3.7 and 3.8.

The previously observed 85.0, (137.2) and (400.7) keV transitions and the newly observed 454.2, 1036.6, (2376), 2396 keV transitions have been placed as populating the

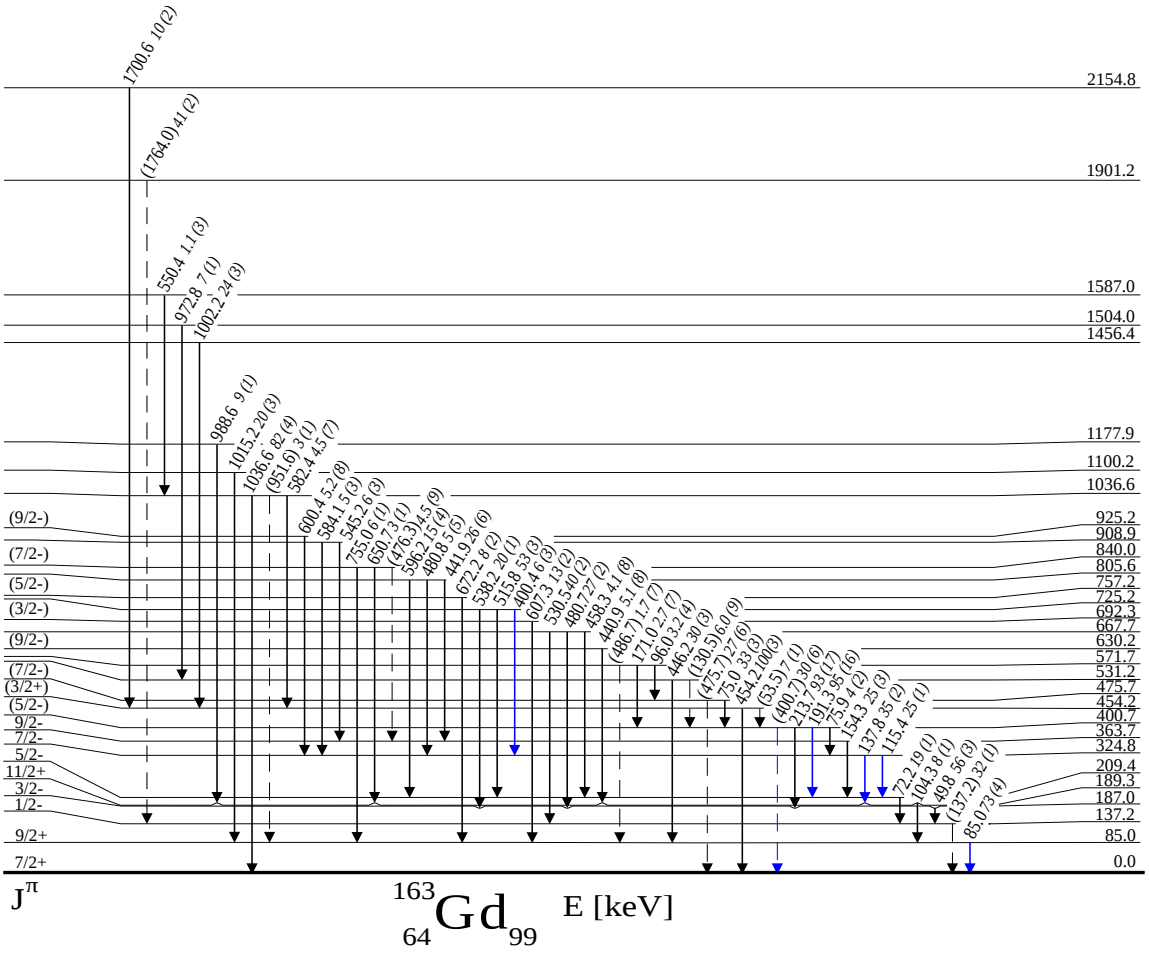

Figure 3.7: Level scheme of ^{163}Gd. New transitions and levels in black, previously identified transitions in blue.

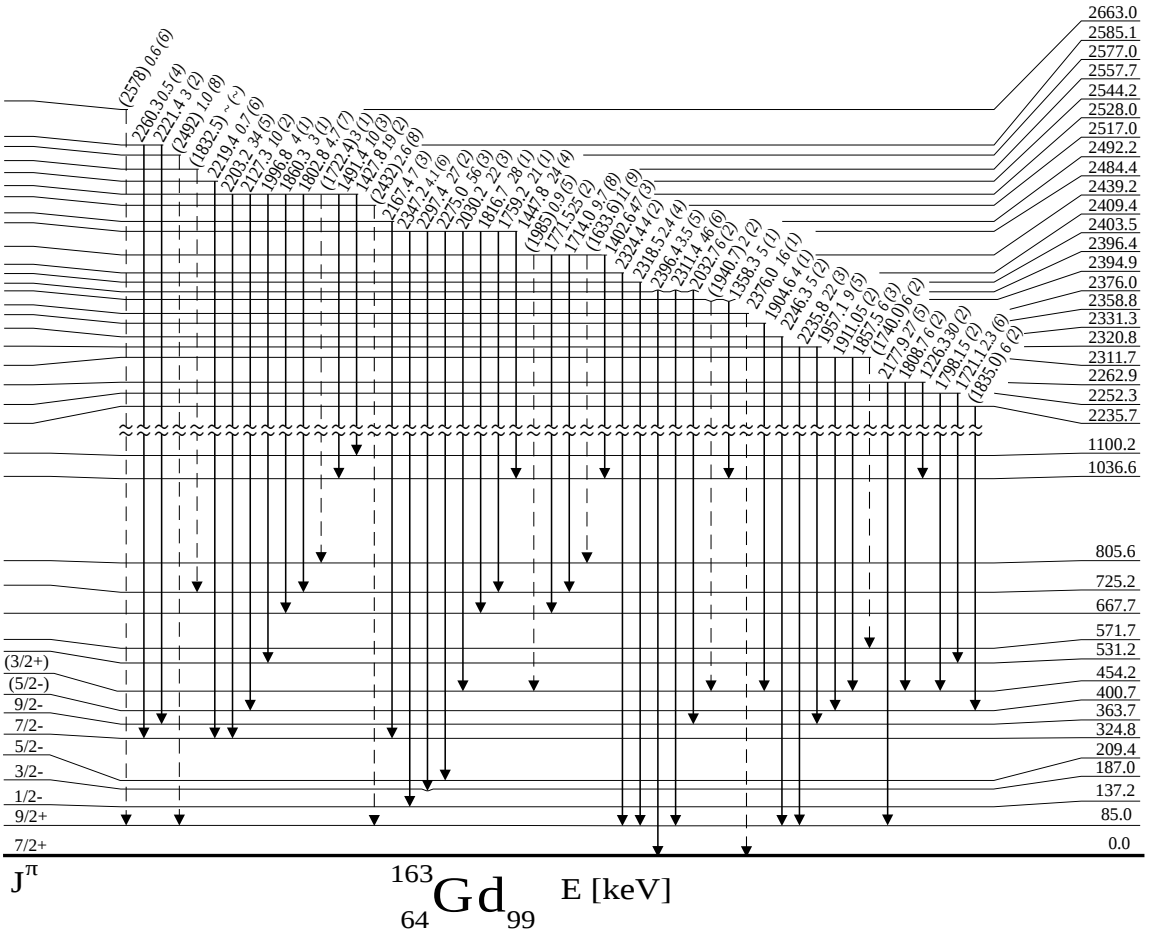

Figure 3.8: Level scheme of ^{163}Gd continued. New transitions and levels in black, previously identified transitions in blue.

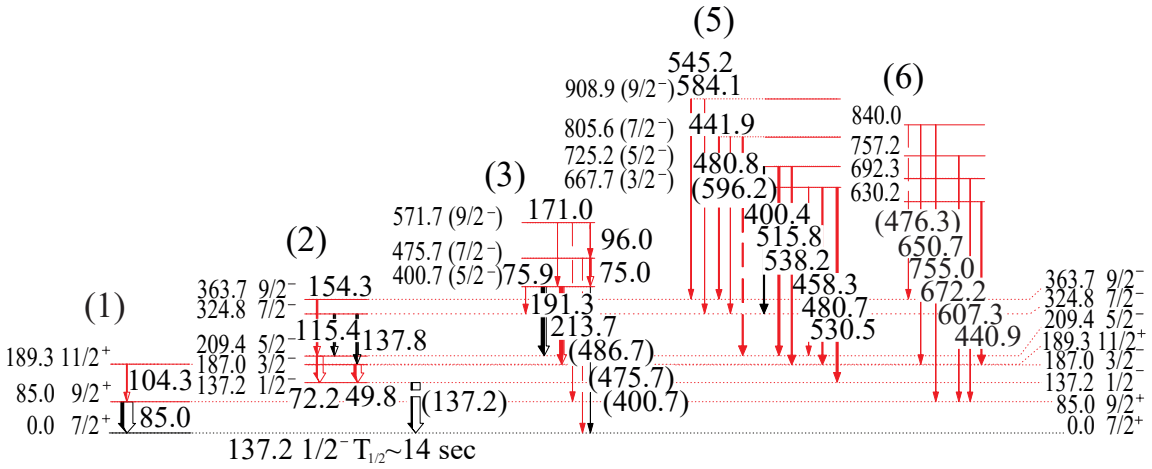

Figure 3.9: Band assignments based on odd neutron levels in N=99 ^{163}Gd and ^{165}Dy. New transitions and levels in red, previously identified transitions in black.

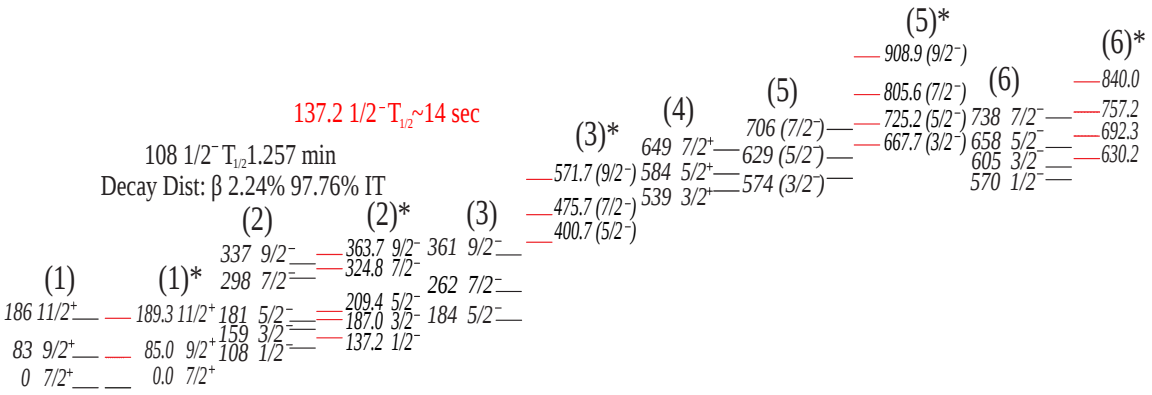

Figure 3.10: Comparison of the low-energy band structure of ^{165}Dy with the porposed low-energy level scheme of ^{163}Gd. Bands proposed for ^{163}Gd marked with *.

ground state which has been assigned a spin value of $7/2^+$. This assignment of $7/2^+$ as the ground state of ^{163}Gd is based upon systematics with ^{165}Dy because both have N=99 and the similarities in level spacings observed [24, 27, 28]. Assignment of the $1/2^-$ band in ^{163}Gd was based upon systematics of the $1/2^-$ band structure observed in ^{165}Dy. In ^{165}Dy, the $1/2^-$ band contains γ transitions up to $9/2^-$ and level spacing consistent with large signature splitting. A very similar structure is observed in ^{163}Gd. In ^{165}Dy the following transitions are observed within the first $1/2^-$ band: 50.4, 72.8, 116.8, 139.1, and 156.2 for which the analogs in the proposed $1/2^-$ band in ^{163}Gd are 49.8, 72.2, 115.4, 137.8, and 154.3 keV. These transitions have been listed according to the levels between which they are observed in ^{165}Dy and the matching spin levels where they are proposed to be transitions in ^{163}Gd. Additional lower energy transitions within the first $1/2^-$ band of ^{165}Dy were observed at the energies of 22.4 and 39.5 keV, and according to the proposed scheme, would be expected within ^{163}Gd to be 22.4 and 38.9 keV. However, these transitions are in an energy region for which the internal conversion is very strong. Thus, their not being clearly observed within the scope of this study is not disconcerting.

The excitation of the $1/2^-$ band head was initially assigned based upon the level spacing of the coincident 1771.5, 1816.7, and 2203.2 keV transitions originating from single particle levels at energies of X+2302.0, X+2347.2, and X+2390.8. The energy spacing of these single particle states matched within uncertainties the spacing of the 2439.2, 2484.4, and 2528.0 keV single particle states which depopulate through transitions coincident with the 1036.6 keV transition to ground. This assignment that these are the same three levels yields the excitation energies of 137.2 and 400.7 keV for the $1/2^-$ and $(5/2^-)$ band heads. These energies are very similar to two other identified transitions in the level scheme, 137.8 and 400.4 keV, which complicates their clear identification from the $1/2^-$ band head with only γ-γ coincidence. Following this analysis, the $1/2^-$ band and other low-energy levels in ^{163}Gd, shown in figure 3.9, are found to compare well with the low-energy levels in ^{165}Dy, shown in Figure 3.10.

Transitions from the $1/2^-$ and $(5/2^-)$ band heads to ground are expected at (137.2) and (400.7) keV. However, with the transitions of 137.8 and 400.4 keV being more clearly evident in the coincidence spectra, depopulating other levels, clear observations of these 137.2 and 400.7 keV ground state transitions were not possible with this setup. Although, each of these transitions do exhibit enhancement in the singles spectra which suggests they are doublets. With the observed peak intensity enhancement and the matching spacing of the associated single particle states, the $1/2^-$ band head is tentatively assigned to have an excitation of 137.2 keV. If it is taken that both the 108.2 keV transition in ^{165}Dy and the 137.2 keV transition in ^{163}Gd are pure E3 transitions, the half-life of the 137.2 keV transition can be roughly estimated according to the reduced transition probabilities for E3 transitions by assuming the same reduced transition probability for both transitions. As the half-life of the 108.2 keV transition was observed to be 1.257 minutes [29], the half-life of the 137.2 keV transition would be estimated as 14.3s per:

$$t_{1/2b} = t_{1/2a} * (E_{\gamma a}^7 / E_{\gamma b}^7) \tag{3.2}$$

This is according to the energy relationship for reduced transition probabilities as discussed in [30].

Observations of transitions in the $7/2^+$ band were limited to only the newly identified 104.3 keV transition and the previously observed, but not placed 85.0 keV transition. This is in agreement with a ground state spin on the parent isotope, ^{163}Eu, being $5/2^+$ allowing for population of excited states in the $7/2^+$ band predominantly via γ-transitions from high-energy single particle states. The β-feeding of the $7/2^+$ band is expected to be limited as decays to the $9/2^+$ and $11/2^+$ are second-forbidden β-decay transitions. Furthermore, population of the $3/2^-$, $5/2^-$, and $7/2^-$ levels can be populated by first-forbidden β transitions and the $9/2^-$ by first-forbidden unique β transitions. An alternative parent ground state of $5/2^-$ would increase the likelihood of direct β population of the $9/2^+$ state and is discussed

in 3.5.

From further investigations following the placement of the $1/2^-$ band head at 137.2 keV and the ground state as $7/2^+$, the following tentative transitions were observed: from the 475.7 keV ($7/2^-$) level to the ground state a (475.7) keV transition; and from the 840 keV level in the unassigned band A to the 363.7 keV $9/2^-$ level in the $1/2^-$ band a (476.3) keV transition; and between the 571.7 keV (9/2-) level and the 85.0 keV $9/2^+$ level a 486.7 keV transition. These tentative observations provide some additional support for the selection of the $7/2^+$ as the ground state and the excitation of the $1/2^-$ band although a more clear association would be preferred.

Figure 3.11 (a) and (b) show spectra of those γ-transitions coincident with the 85.0 keV transition. Therein are clearly observed the 104.3, 440.9, 446.2, 988.6, 1015.2, and 1427.8 keV transitions. Gates on each of these transitions are consistent with their assignments. Gating on the 104.3 keV γ-ray allows observation of the 650.7 keV transition, which is of low intensity and is not distinguishable from the background in the coincidence spectra of the strong 85.0 keV transition. Also seen in the 85.0 keV coincidence spectra are evidences for a number of transitions that are not observed in gates for any other transitions but whose coincidence spectra are consistent with their assignment: 607.3, 672.2, 2177.9, 2235.8, 2246.3, 2311.4, 2318.5, 2324.4, 2432, 2492, and 2578 keV transitions. The 191.3 keV peak is due to incomplete background subtraction.

Seen in Figure 3.11 (c) and (d) are transitions coincident with the 191.3 keV transition; (53.5), 72.2, (75.0), 96.0, 130.5, (171.0), (1740.0), (1835), 1857.5, 1911.0, 2030.2, (2046), 2083.7 and 2127.3 keV. The observation of the (53.5) keV transition in this gate, a weak aberration on the shoulder of the 49.8 keV x-ray, corroborates the $1/2^-$ band head assignment. However, this transition is in a region of very strong internal conversion and gates upon the 53.5 keV transition do not confirm this assignment, therefore, it is only tentatively placed. The 130.5 keV transition matches the energy to originate from the 531.2 keV level to the 400.7 keV level, but a gate on 130.5 keV does not show the expected coincident

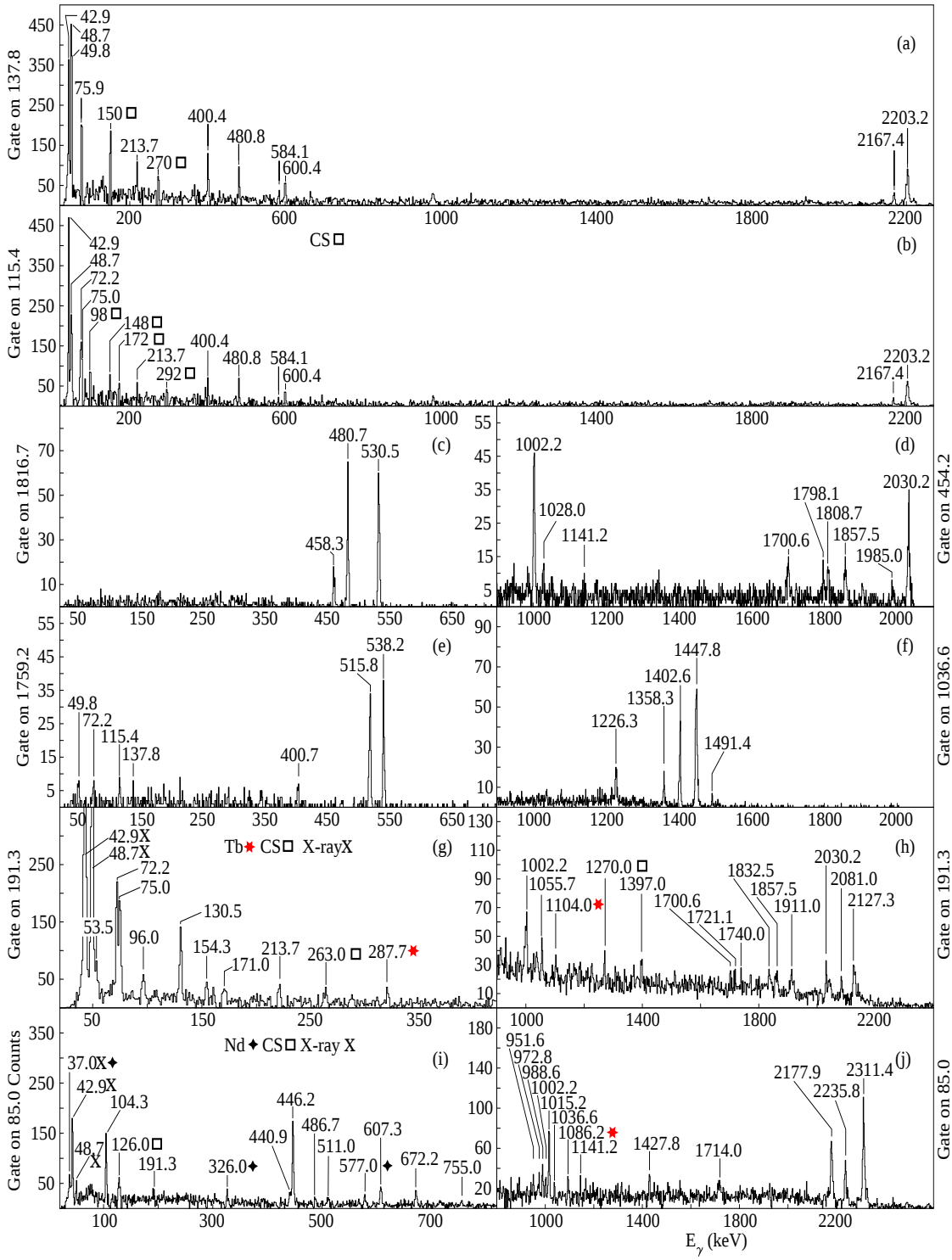

Figure 3.11: Coincidence spectra for gates on ^{163}Gd transitions; (a)&(b) 85 keV, (c)&(d) 191.5 keV, (e) 1759 keV, (f) 446.5 keV, (g) 454.5 keV, (h) 1815 keV, (i) 115.5 keV, (j) 137.5 keV. Where CS indicates a Compton Scatter peak.

transitions. This transition is thus tentative. While the 171.0 keV transition appears clearly in the gate on the 191.3 keV transition, a further gate on the 171.0 keV transition does not clearly indicate any further coincidence. Similarly, a gate on the 75.0 keV transition does not provide clear evidence for this placement as it feeds from the 454.2 keV level to the 400.7 keV level. However, the 171.0 and 75.0 keV transitions would be consistent with the structure of the $5/2^-$ band observed in ^{165}Dy and a 486.7 keV transition has been observed that would be consistent with the placement of a 571.7 keV $9/2^-$ level as previously mentioned. The competition between the 486.7 keV transition, expected to have a multipolarity of E1, and the 171.0 keV transition, anticipated to be a rotational band E2 transition, would explain the reduced intensity observed for the 171.0 keV transition. The (1740) keV transition would agree with a transition from 2311.7 to 517.1 but is not strongly observed and is thus tentative. The (1835) and (2046) transitions are not observed to be contaminants but otherwise appear only in this coincidence gate and gates upon each of these transitions do not yield clear coincidence with any other γ-ray or x-ray from ^{163}Gd, thus these transitions are included tentatively.

In frame (e) of Figure 3.11 is seen the coincidence spectra for a gate on the 1759.2 keV transition. Apparent peaks in spectra (e) from 140 to 400 are aberrations due to low counts when using background subtraction. The peaks of 400.4, 515.8, and 538.2 keV correspond to the three transitions from the 725.2 keV ($5/2^-$) level to the 324.8 keV $7/2^-$, 209.4 keV $5/2^-$, and 187.0 keV $3/2^-$ levels, respectively. Similarly, frame (h) shows coincident spectra for the gate on the 1816.7 keV transition. The peaks of 458.3, 480.7, and 530.5 keV correspond to the three transitions from the 667.7 keV level to the 209.4 keV $5/2^-$, 187.0 keV $3/2^-$, and 137.2 keV $1/2^-$ levels, respectively. The sequential transitions for 1816.7 would be 72.2 and 49.8, but are not visible after background subtraction for the spectra in frame (h). For both of these coincidence spectra, it is clearly seen that only three transitions are well observed exiting the $3/2^-$ band at each of these levels. Although allowed from a $5/2^-$ level, no transition has been observed to the $7/2^+$ ground state band from these lev-

els. Similar transitions between the $3/2^-$ proposed gamma vibrational band and the $1/2^-$ band in ^{165}Dy are observed. Thus, the 667.7, 725.2, 805.6, and 908.9 keV levels have been tentatively assigned to the $(3/2^-)$ band. Additionally, sequential transitions of 137, 115, 49.8 and 72 are visible in frame (e). Further apparent peaks are the result of low count background subtraction.

In frame (f) of Figure 3.11 is seen the coincidence spectra for a gate on the 1036.6 keV transition, demonstrating coincidence with the 1226.3, 1358.3, 1402.6, 1447.8, and 1491.4 keV transitions. In frame (g) of Figure 3.11 is seen the coincidence spectra for a gate on the 454.2 keV transition, demonstrating coincidence with the 1002.2, 1700.6, 1798.1, 1808.7, 1857.5, 1904.6, and 2030.2 keV transitions. The 2030.2 keV transition coincident with the 454.2 keV transition and the 1491.4, 1447.8, and 1402.6 keV transitions observed in coincidence with 1036.6 keV transition provide the strongest observation of the 2528, 2484.4 and 2439.2 keV levels by which the two separately observed structural elements of ^{163}Gd were associated. The 1036.6 keV level from which the 1036.6 keV transition to ground originates is taken to be a n+1 particle state within ^{163}Gd. The 454.2 keV level is low enough in energy for anticipated single particle states though no band structure is observed on top of this state. It is possible that the 454.2 keV is associated with the $7/2^-[514]$ neutron level, this would be consistent with the strong apparent β-feeding received by the 454.2 keV level. However, with no observed band structure, it is not clear with what neutron state this strongly populated level is associated. As the most intense transition in ^{163}Gd, the 454.2 keV transition has been used as the reference peak for the relative intensity measurements of transitions in ^{163}Gd.

Frames (i) and (j) are gates upon the two previously observed transitions of 115.4 and 137.8 keV. Evidence is seen in these gates for the 49.8 keV transition and the 72.2 keV transition. Note that while the 49.8 keV peak appears in both spectra, it is strongly enhanced in the 137.8 keV gate because this transition overlaps in energy the K_b1 x-rays for ^{163}Gd. The enhancement observed only in the 137.8 keV gate is because the 49.8 keV co-

incident γ-ray transition adds intensity to the x-ray peak while the peak observed in 115.4 keV gate is expected to be only from the K x-rays from ^{163}Gd. Strong 191.3 keV and 75.0 keV peaks are observed in the gate on 137.8 keV due to Compton scatter from 213 keV transitions. Seen in these gates are the high-energy 2203.2 and 2167.4 keV transitions. Of particular note is the relative intensity between the 2203.2 keV tansition and the 400.4 keV transition. While the 400.4 keV transition in the singles spectra is of similar intensity to that of the 2203.2 keV transition, after efficiency corrections, it is clearly seen here that the 2203.2 keV transition is much stronger in this gate relative to the 400.4. Note that for the HPGe's used in this study, the efficiency continually drops with energy beyond $\approx$100 keV, thus the similar sized 2203.2 keV transition observed in the figure would correspond to a much stronger transition by comparison with the 400.4 keV transition. This means that the 400.4 is not the only $\approx$400 keV transition, and while a clear observation of the 400.7 keV transition to ground is complicated by this energy degenerate transition, the intensity discrepancy provides support for its existence.

The 85.0, 454.2, 1036.9, (2376), and 2396.4 keV transitions are the only transitions to ground observed clearly in this work. Given the strong γ feeding of the $1/2^-$ 137.2 keV level which could feed the ground state via a 137.2 keV transition, the lack of clear observation of a 137.2 keV γ-ray is either indicative of the state having a lifetime on the order of seconds, or the assignment of the $1/2^-$ band is incorrect. The former is the most likely based upon the lifetime of the $1/2^-$ state in ^{165}Dy.

As for the remaining transitions identified in ^{163}Gd at 2318.5, 2324.4, 2347.8, 2365.2, 2376, 2396.4, and 2492 keV, they are not clearly present in the total projection but are coincident with appropriate K x-ray peaks, and are present in the singles spectra, not shown.

Shown in Figure 3.9 are those levels and associated transitions found in ^{163}Gd that are best candidates for band members. Here we see analogs for the $7/2^+$ band, first $1/2^-$ band, the $5/2^-$ band, the $3/2^-$ band and a potential candidate for the second $1/2^-$ band in ^{163}Gd. No observation is made of an analog to the $3/2^+$ band in ^{165}Dy which inclines the author to

Table 3.1: Transitions in ^{163}Gd. Transition energy, intensity, internal conversion corrected intensity, assumed multipolarity, energy and J^π of initial and final levels. J^π assignments from systematics with ^{165}Dy, [24, 27, 28].

E_γ (keV)	$I_\gamma(\%)$	$I_\gamma(\%)ICC$	*ICC Multipolarity*	E_i	E_f	J_i^π	J_f^π
49.8	55(3)	188(10)	M1	187.0	137.2	$3/2^-$	$1/2^-$
53.5	7(1)	94(16)	M1	454.2	400.7	$(3/2^+)$	$(5/2^-)$
72.2	19(2)	114(7)	M1	209.4	137.2	$5/2^-$	$1/2^-$
75.0	33(3)	182(14)	M1	475.7	400.7	$(7/2^-)$	$(5/2^-)$
75.9	4(2)	21(13)	M1	400.7	324.8	$(5/2^-)$	$7/2^-$
85.0	73(4)	30 6(16)	M1	85.0	0.0	$9/2^+$	$7/2^+$
96.0	3.2(4)	11(1)	M1	571.7	475.7	$(9/2^-)$	$(7/2^-)$
104.3	8(1)	22(3)	M1	189.3	85.0	$11/2^+$	$9/2^+$
115.4	25(1)	58(3)	M1	324.8	209.4	$7/2^-$	$5/2^-$
130.5	6.0(9)	12(2)	M1	531.2	400.7		$(5/2^-)$
137.2	32(1)	284(13)	E3	137.2	0.0	$1/2^-$	$7/2^+$
137.8	35(2)	63(3)	E2	324.8	187.0	$7/2^-$	$3/2^-$
154.3	25(3)	40(5)	E2	363.7	209.4	$9/2^-$	$5/2^-$
171.0	2.7(7)	4(1)	M1	571.7	400.7	$(9/2^-)$	$(5/2^-)$
191.3	94(16)	125(21)	M1	400.7	209.4	$(5/2^-)$	$5/2^-$
213.7	93(17)	115(21)	M1	400.7	187	$(5/2^-)$	$3/2^-$
400.4	6(3)	6(3)	M1	725.2	324.8	$(5/2^-)$	$7/2^-$
400.7	30(6)	30(6)	E1	400.7	0.0	$(5/2^-)$	$7/2^+$

accept a $5/2^-$ ground state of the parent isotope as discussed in Chapter 3.5. The layout of these bands has been modified to reflect that of the previously shown ^{165}Dy level scheme in Figure 3.6.

Tables 3.1, 3.2, and 3.3 list every transition observed in ^{163}Gd, the relative intensity referenced to the 454.2 keV transition with uncertainty of the last digit indicated in parenthesis, the internal conversion corrected intensities and the multipolarity assumed for this correction, the energy of the initial and final levels as well as the spin of the initial and final levels for those levels with spin assignments.

Table 3.2: Transitions in ^{163}Gd continued.

E_γ (keV)	$I_\gamma(\%)$	E_i	E_f	J_i^π	J_f^π
440.9	5.1(8)	630.2	189.3		$11/2^+$
441.9	26(6)	805.6	363.7	$(7/2^-)$	$9/2^-$
446.2	30(3)	531.2	85.0		$9/2^+$
454.2	100(3)	454.2	0.0	$(3/2^+)$	$7/2^+$
458.3	4.0(8)	667.7	209.4	$(3/2^-)$	$5/2^-$
475.7	27(6)	475.7	0.0	$(7/2^+)$	
476.3	5(1)	840.0	363.7		$9/2^-$
480.7	27(2)	667.7	187.0	$(3/2^-)$	$3/2^-$
480.8	5(4)	805.6	324.8	$(7/2^-)$	$7/2^-$
486.7	1.7(7)	571.7	85.0	$(9/2^-)$	$9/2^+$
515.8	53(3)	725.2	209.4	$(5/2^-)$	$5/2^-$
530.5	40(2)	667.7	137.2	$(3/2^-)$	$1/2^-$
538.2	20(1)	725.2	187.0	$(5/2^-)$	$3/2^-$
545.2	6(3)	908.9	363.7	$(9/2^-)$	$9/2^-$
550.4	1.0(3)	1587.0	1036.6		
582.4	4.5(7)	1036.6	454.2		$(3/2^+)$
584.1	5(3)	908.9	324.8	$(9/2^-)$	$7/2^-$
596.2	15(4)	805.6	209.4	$(7/2^-)$	$5/2^-$
600.4	5.2(8)	925.2	324.8		$7/2^-$
607.3	13(2)	692.3	85.0		$9/2^+$
650.7	3(1)	840.0	189.3		$11/2^+$
672.2	8(2)	757.2	85.0		$9/2^+$
755.0	6(1)	840.0	85.0		$9/2^+$
951.6	3(1)	1036.6	85.0		$9/2^+$
972.8	7(1)	1504.0	531.2		
988.6	9(1)	1177.9	189.3		$11/2^+$
1002.2	24(3)	1456.4	454.2		$(3/2^+)$
1015.2	20(3)	1100.2	85.0		$9/2^+$
1036.6	81(4)	1036.6	0.0		$7/2^+$
1226.3	30(2)	2262.9	1036.6		
1358.3	5(1)	2394.9	1036.6		
1402.6	47(3)	2439.2	1036.6		
1427.8	18(2)	2528.0	1100.2		
1447.8	24(4)	2484.4	1036.6		
1491.4	10(3)	2528.0	1036.6		
1633.6	11(9)	2439.2	805.6		$(7/2^-)$
1700.6	10(2)	2154.8	454.2		$(3/2^+)$
1714.0	9.7(8)	2439.2	725.2		$(5/2^-)$
1721.1	2.3(6)	2252.3	531.2		
1722.4	3(1)	2528.0	805.6		$(7/2^-)$

Table 3.3: Transitions in ^{163}Gd continued.

E_γ (keV)	I_γ(%)	E_i	E_f	J_i^π	J_f^π
1740.0	6(2)	2311.7	571.7		$(9/2^-)$
1759.2	21(1)	2484.4	725.2		$(5/2^-)$
1764.0	41(2)	1901.2	137.2		$1/2^-$
1771.5	25(2)	2439.2	667.7		$(3/2^-)$
1798.1	5(2)	2252.3	454.2		$(3/2^+)$
1802.8	4.7(7)	2528.0	725.2		$(5/2^-)$
1808.7	6(2)	2262.9	454.2		$(3/2^+)$
1816.7	28(1)	2484.4	667.7		$(3/2^-)$
1832.5		2557.7	725.2		$(5/2^-)$
1835.0	6(2)	2235.7	400.7		$(5/2^-)$
1857.5	6(3)	2311.7	454.2		$(3/2^+)$
1860.3	3(1)	2528.0	667.7		$(3/2^-)$
1904.6	4(1)	2358.8	454.2		$(3/2^+)$
1911.0	5(2)	2311.7	400.7		$(5/2^-)$
1940.7	2(2)	2394.9	454.2		$(3/2^+)$
1957.1	9(5)	2320.8	363.7		$9/2^-$
1985.0	0.9(5)	2439.2	454.2		$(3/2^+)$
1996.8	4(1)	2528.0	531.2		
2030.2	22(3)	2484.4	454.2		$(3/2^+)$
2032.7	6(2)	2396.4	363.7		$9/2^-$
2127.3	10(2)	2528.0	400.7		$(5/2^-)$
2167.4	7(3)	2492.2	324.8		$7/2^-$
2177.9	27(5)	2262.9	85.0		$9/2^+$
2203.2	34(5)	2528.0	324.8		$7/2^-$
2219.4	0.7(6)	2544.2	324.8		$7/2^-$
2221.4	3(2)	2585.1	363.7		$9/2^-$
2235.8	21(3)	2320.8	85.0		$9/2^+$
2246.3	5(2)	2331.3	85.0		$9/2^+$
2260.3	0.5(4)	2585.1	324.8		$7/2^-$
2275.0	56(3)	2484.4	209.4		$5/2^-$
2297.4	27(2)	2484.4	187.0		$3/2^-$
2311.4	46(5)	2396.4	85.0		$9/2^+$
2318.5	2.4(4)	2403.5	85.0		$9/2^+$
2324.4	4(2)	2409.4	85.0		$9/2^+$
2347.2	4.1(6)	2484.4	137.2		$1/2^-$
2376.0	16(1)	2376	0.0		$7/2^+$
2396.4	3.5(5)	2396.4	0.0		$7/2^+$
2432.0	2.6(8)	2517	85.0		$9/2^+$
2492.0	1.0(8)	2577	85.0		$9/2^+$
2578.0	0.6(6)	2663	85.0		$9/2^+$

3.5 ^{163}Gd Discussion

The analysis of the ^{163}Eu β-decay data presented several challenges. The first and most significant being that of identifying which γ-transitions were feeding the ground state. The present ground state assignment of $7/2^+$ was only recently put forward following the systematic assignments cited previously in 3.4. Previous to this, the ground state had been assigned following initial analysis presented by Brewer as part of his doctoral thesis [5]. Both the author and Brewer had originally selected the ground state as being fed by the 191.3 keV transition while treating the 213.7 keV transition as a contaminant from sequential ^{163}Tb decay. Earlier, the 72.2 keV and 49.8 keV transitions had been assigned as higher in the level scheme for a combination of reasons; Contamination from ^{163}Tb decay for the 72.2 keV transition and x-ray contamination for 49.8 keV were problems. Both transitions have strong internal conversion. Furthermore, a transition from the $1/2^-$ band to ground is still not clearly observed and, at that time was not anticipated, as the 191.3 keV was taken as going to ground. At that time the 85.0 keV transition was treated as feeding an isomer and this was taken as explanation for the absence of transitions following the 85.0 keV transition to the previously proposed level of 151.1 keV.

With 49.8 and 72.2 keV transitions being out of place, efforts by both parties resulted in a structure that placed low and high-energy transitions in competition. This conflicted with theoretical understandings. From the perspective of coincidence spectra only, the structure appeared correct though theoretically improbable. It was not until a rigorous intensity analysis, as called for in Brewer's work, showed irreconcilable discrepancies that the previous scheme was abandoned. From there the analysis was begun anew, starting from the log book. The new analysis has resulted in the level scheme shown in Figures 3.7 and 3.8.

Of significance to the unfolding of the level structure of ^{163}Gd is that the systematics described in the second paragraph of Chapter 3.4 are not apparent without the 49.8 and 72.2 keV transitions being placed below the 191.3 keV transition in the level scheme, a transition

that is now proposed to be from the $(5/2^-)$ band head to the $5/2^-$ level in the first $1/2^-$ band. The new arrangement of these low-energy transitions resolved both the complications between the proposed level scheme [5] and theory, and made the similarity between the structure of ^{165}Dy and ^{163}Gd readily apparent, following the advice of J. Hamilton [31]. Analysis from this point now had a new resource in the similarity in structure between N=99 ^{165}Dy and ^{163}Gd with one odd neutron. However, agreement within a band does not mean that all the observed bands can be expected in both nor that the bands will occur with the same excitation energies. Thus, the question of what the excitation of the ground state still persisted at this late stage of the analysis.

Following the re-organization of the level scheme, there emerged two distinct structures with no immediately apparent transitions to the ground state, the same complication as had previously been encountered. The Figure 3.12 shows the two groups of states and their associated transitions, none of which had well observed transitions connecting either structure to the other. Such a structural divide presents a significant problem in coincidence analysis as without some outside observation there is no simple strong method for selection of the ground state. This is because coincidence analysis is fundamentally a logic relationship analysis method, and without any observed logical relationship, there is no explanation coincidence analysis can provide. Yet as advised by Wang, though coincidence analysis is done exclusively by observations of γ transitions, these are not the only information there is to work with in coincidence analysis [32].

Following the recommendation of Wang in the absence of observed linking transitions, the evaluation turned to other structural information which could be obtained from the coincidence data, specifically level spacing. As the uncertainty of a level energy is a function of how many transitions the level is from the ground state structural analysis is best done with direct observation of the γ-rays emitted during a nuclear transition. Additionally, there is little preventing a nucleus from having a state of energy degenerate within the uncertainty of measurement, especially for well deformed nuclei such as those found in the A$\approx$160

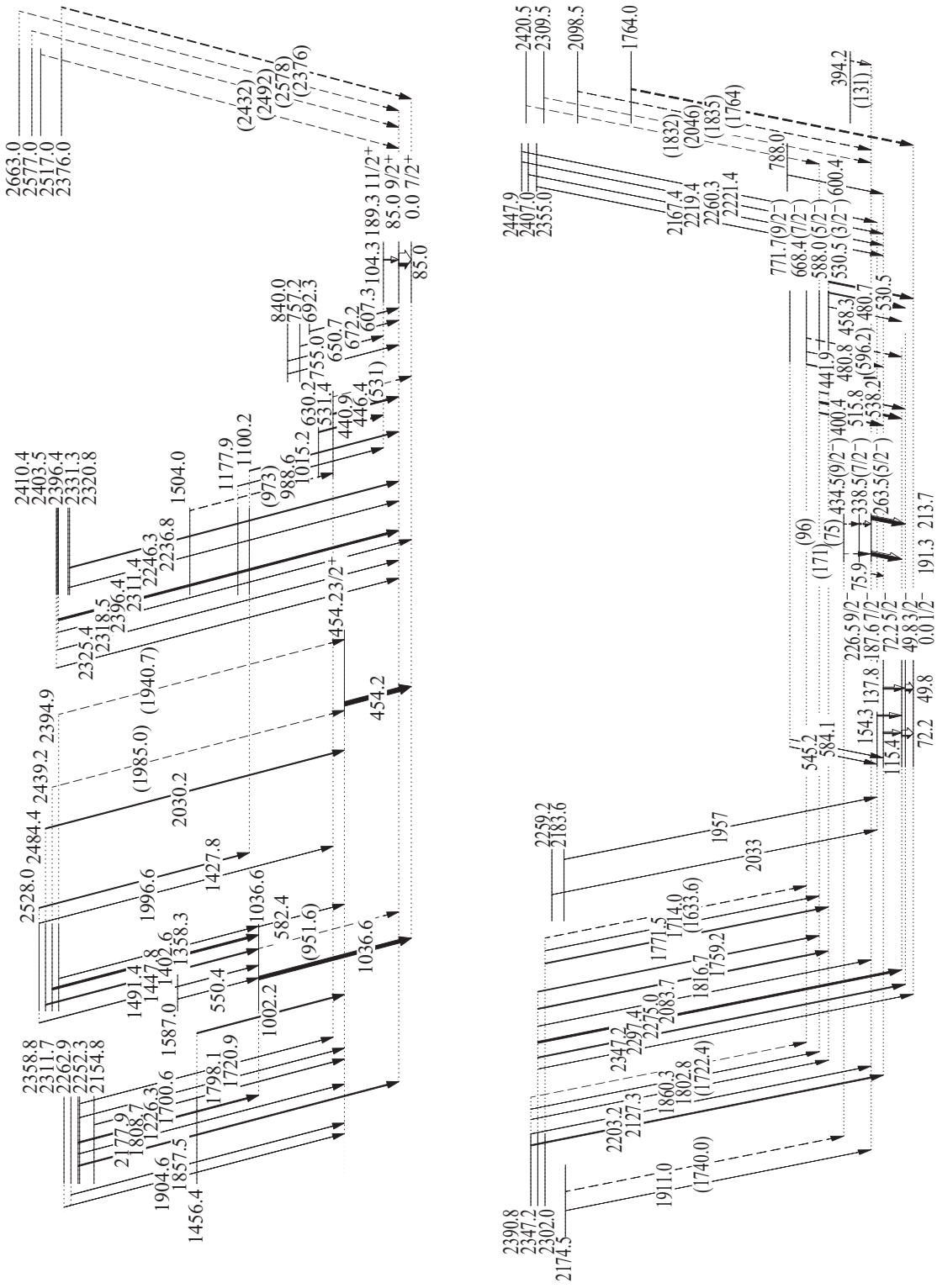

Figure 3.12: Partial level schemes of ^{163}Gd for all transitions presently confirmed with relation to the ground state.

region. Thus, the approach used had the goal of finding a set of levels in both structures which were as close to identically spaced as possible. Once such a set was found, one would then be able to look for weaker transitions corresponding to the spacing between the two structures that had previously been overlooked because of low intensity.

A brief search found a set of levels associated with single particle states that were observed with spacing that matched within uncertainties, as detailed in Chapter 3.4. As levels associated with single particle states are frequently degenerate within uncertainties this assignment could not be based upon this common structure alone. Thus, the combined structure of ^{163}Gd as seen in Figures 3.7 and 3.8 was put together and the search for direct observation of linking transitions was resumed.

What this combined structure, based on secondary conclusions, makes possible is identification of further levels which provide a guide for what energy transitions can be anticipated. It is possible that very weak transitions were overlooked because the intensity is very close to the background, from Compton scatter signals, or is nearly degenerate in energy with another previously identified transition. As mentioned briefly in Chapter 3.1, molecular contaminants as well as isotopes of similar mass and charge are still possible with Q/A beam selection. This means that a molecule or other isotopic contaminant of the appropriate Q/A can be passed through the filter and onto the MTC. This results in there being a limited amount of beam contaminants that have a few previously observed transitions associated with them that can obscure possible weak transitions belonging to the isotopes of interest. The effects of these contaminants are further discussed in Chapter 4.3. Armed with the expected energies of the transition between the two separate structures observed in ^{163}Gd, it was found that two such tentative transitions had been overlooked because they were close in energy to transitions in contaminant ^{163}Dy.

Review of the ^{165}Dy level scheme in Figure 3.6 revealed that no analogs of the 191.3 & 213.7 keV transitions in ^{165}Dy are observed. However, these transitions would be M1 transitions of 3.4 and 25.7 keV, respectively, and thus are not expected in ^{165}Dy where they

would be competing with higher energy E1 transitions.

Prior to assignment of the ground state band via spacing similarities of single particle states, either band could have been selected as the ground state band, leaving the other a likely candidate for an isomeric state because of the large spin difference in the band heads. Another approach was pursued for identifying possible isomeric transitions by evaluation of the relative intensities in ^{163}Tb. The objective had been to identify the spin of the apparent beta preferred state. However, this approach was unsuccessful and is discussed further in Chapter 4.3.

Earlier in the analysis of the ^{163}Eu decay data, the primary concern had been the presence of strong Compton scatter signals in the data. Initial concerns had been that these signals were obscuring further transitions within the structure of ^{163}Gd that would have offered either some further support of, or explanation for, the anomalous transition pairings previously discussed. In the course of the investigation it was found that while Compton scatter is a common complication for γ-ray spectroscopy experiments there was not a common method for resolving the issue in post processing. The primary means of addressing Compton scatter is either by implementing an active Compton suppression system at the time data is collected, or by placing heavy shielding between γ-ray detectors to act as passive Compton suppression. The state of the art γ spectrometers operate off of γ-ray tracking thereby obviating the need for Compton suppression by reconstructing the path of the γ-ray back through all Compton scatter events.

To address the issue of Compton scatter in the data already collected, several modifications to the data analysis process were considered including, rejection of signals from adjacent detectors, hard coded identification of cross talk, stochastic crosstalk rejection, and analysis of the Compton peak cross section. However, each method either reduced signal intensities too much to be effective, introduced bias into the analysis, or would take too long to implement. Ultimately, it was found that a rigorous relative intensity analysis and careful application of crosstalk background subtraction techniques provided by

Allmond [22] in conjunction with consideration of the physics of Compton scatter would make analysis of the data complete without modification to the SCAN code.

In Chapter 3.1 the capability of this data set to plot transition intensities as a function of tape cycle time was described. However, what is plotted in Figure 3.4 is the overall intensities of transitions coincident to a given energy that are within the coincidence window. There is, however, a limitation on the ability to correlate signals over long time frames as there is no means of confirming the origin of a γ-ray observation other than time. After a window on the order of a few micro seconds has passed, the likelihood that observed transitions are originating from a different nuclear decay approaches unity. Thus, this method is not capable of obtaining a lifetime for the proposed isomeric state at 137.2 keV.

Table 3.4 lists the internal conversion corrected feeding and outflow observed from γ relative intensity measurements for ^{163}Gd. As mentioned in the results section, the states populated in the 7/2+ band are only observed up to 11/2+. These are expected only to be populated from gamma feeding from single particle states. A review of Table 3.4 shows a feeding and outflow relationship consistent with very limited β-feeding for the 189.3 keV level the apparent beta feeding, gamma outflow in excess of gamma feeding, is very low. However, the apparent beta feeding of the 85 keV 9/2+ state, a second-forbidden transition for a parent ground state of $5/2^+$, is comparable to that of the 725.2 keV ($5/2^-$), a first-forbidden transition. While it is possible that there is an artificial enhancement of the 85.0 keV transitions intensity, this also presents some evidence against the 9/2+ spin assignment for this level.

There remains a few transitions which would be expected given the band assignments made in ^{163}Gd that are not observed. In ^{165}Dy there is observed a $3/2^+$ band with transitions to both the first $1/2^-$ band and the $7/2^+$ ground state band. There is no analog to this band recognized within the observations of this work. This is unexpected as the ground state of the parent nucleus is tentatively expected to have a spin of $5/2^+$ according to both the Nilsson levels for protons shown in Figure 3.13, and based upon the tentative ground state

Table 3.4: Internal Conversion Corrected γ Feeding and γ Outflow in ^{163}Gd. J^{π} assignments in the current work from systematics with ^{165}Dy, [24, 27, 28].

E_{Level} (keV)	γ Feeding	γ Outflow	J^{π}	E_{Level} (keV)	γ Feeding	γ Outflow	J^{π}
0	848(22)	0(0)	7/2+	1456.4	0(0)	24(3)	
85	213(11)	306(15)	9/2+	1504.0	0(0)	7(1)	
137.2	387(13)	284(13)	1/2-	1587.0	0(0)	1.0(3)	
187.0	251(21)	188(10)	3/2-	1901.2	0(0)	41(2)	
189.3	18(2)	23(3)	11/2+	2154.8	0(0)	10(2)	
209.4	351(23)	114(7)	5/2-	2235.7	0(0)	6(2)	
324.8	108(17)	121(4)	7/2-	2252.3	0(0)	7(2)	
363.7	53(10)	40(5)	9/2-	2262.9	0(0)	63(5)	
400.7	313(22)	267(33)	(5/2-)	2311.7	0(0)	17(4)	
454.2	85(6)	195(16)	(3/2+)	2320.8	0(0)	30(6)	
475.7	11(1)	209(15)	(7/2-)	2331.3	0(0)	5(2)	
531.2	10(2)	41(3)		2358.8	0(0)	4(1)	
571.7	7(2)	16(2)		2376.0	0(0)	16(1)	
630.2	0(0)	5.1(8)	(9/2-)	2394.9	0(0)	8(2)	
667.7	56(3)	71(3)		2396.4	0(0)	53(7)	
692.3	0(0)	13(2)	(3/2-)	2403.5	0(0)	2.4(4)	
725.2	35(2)	104(7)		2409.4	0(0)	4(2)	
757.2	0(0)	8(2)	(5/2-)	2439.2	0(0)	90(10)	
805.6	11(9)	46(9)		2484.4	0(0)	182(7)	
840.0	0(0)	14(2)	(7/2-)	2492.2	0(0)	7(3)	
908.9	0(0)	11(4)		2517.0	0(0)	2.6(8)	
925.2	0(0)	5.2(8)	(9/2-)	2528.0	0(0)	83(7)	
1036.6	117(6)	89(4)		2544.2	0(0)	0.7(6)	
1100.2	19(2)	20(3)		2557.7	0(0)	0(0)	
1177.9	0(0)	9(2)		2577.0	0(0)	1.0(8)	
1456.4	0(0)	24(3)		2585.1	0(0)	4(2)	
1504.0	0(0)	7(1)		2663.0	0(0)	0.6(6)	
1587.0	0(0)	1.0(3)					

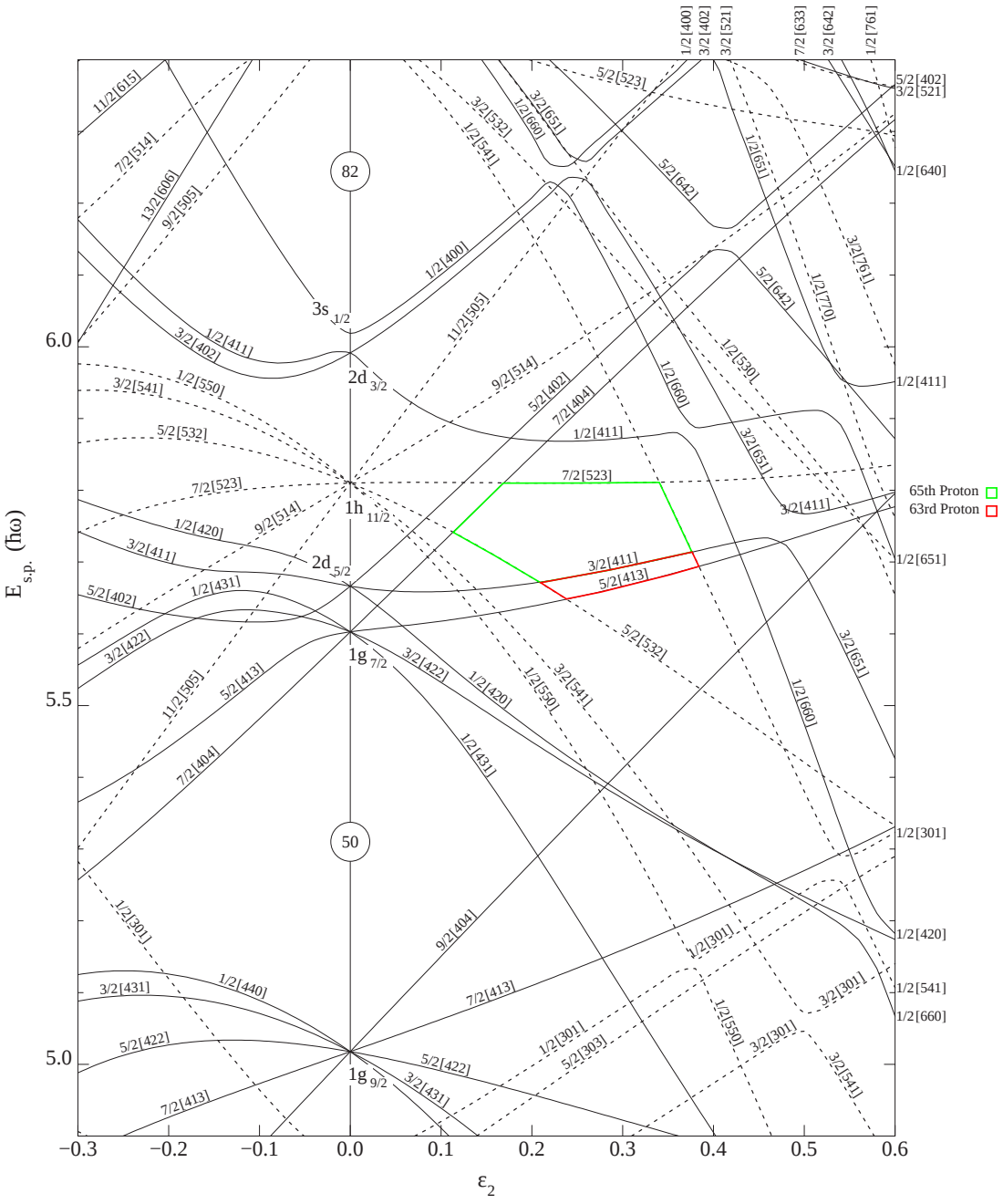

Figure 3.13: Nilsson Levels for Protons. Reproduced from [6].

deformation of the two proton analog of ^{163}Eu, ^{165}Tb. If the parent isotope does indeed have a ground state spin of $5/2^+$, population of the $3/2^+$ should be preferred to all of the observed bands, their linking transitions as shown in Figure 3.9. A lack of a well populated $3/2^+$ band but strongly populated $1/2^-$, $3/2^-$, and $5/2^-$ bands, offers support of the parent ground state being not $5/2^+$ with deformation similar to the 2 proton analog but a less deformed $5/2^-$ as seen in Figure 3.13. With a parent ground state of $5/2^-$, the apparent β-feeding of the $9/2^+$ state is partially reconciled as this would no longer be a second-forbidden β transition but a first-forbidden unique β transition. However, this feeding may still be excessive for even that assignment.

Chapter 4

^{163}Tb

As ^{163}Tb was studied using the same data set as ^{163}Gd see Chapter 3.1 for description of the experimental methods.

4.1 Previous Findings in ^{163}Tb

The structure of ^{163}Tb has been studied via the ^{164}Dy(**t**,α) reaction [33], the ^{164}Dy(**d,**^{3}**He**) reaction [34], and gamma spectroscopy following ^{163}Gd β^- decay [18]. These studies yielded a number of bands and levels within the structure of ^{163}Tb as well as 11 γ transitions, only three of which were tentatively placed in the level scheme. All 11 of the previously observed transitions have been confirmed in this work. In addition to the previous 11 transitions, 40 new transitions have been observed for ^{163}Tb, seven of which are tentative. All transitions have been observed between 12 new levels and 16 previously identified levels, including from reaction studies, with four of the new levels tentative. The list of levels previously identified in both the ^{164}Dy(d,^{3}He) and the ^{164}Dy(t,α) reaction experiments are given in Table 4.1[33, 34].

4.2 ^{163}Tb Results

Gehrke *et al.* performed γ-ray spectroscopy of ^{163}Tb following ^{163}Gd β^- decay observing 11 transitions at the following energies; 214.0, 287.79, 373.37, 396.4, 575.1, 632.9, 1167.7, 1234.4, 1311.6, 1562.1, and 1684.5 keV. These previously known transitions provided an excellent starting point for the present work where they are observed as; 213.9, 287.7, 373.7, 397.3, 575.2, 632.8, 1167.8, 1234.3, 1311.9, 1562.5, and 1685.6 keV. Of the previously identified transitions, only three were tentatively placed in the level scheme,

Table 4.1: Levels previously identified in ^{163}Tb via reaction studies [33, 34].

E_{level} (keV)	J^{π}	E_{level} (keV)	J^{π}
0.0	$3/2^+$	890(2)	$(11/2)^-$
54(2)	$5/2^+$	960(5)	$(1/2^+)$
128(5)	$7/2^+$	987(2)	$(3/2)^+$
223(2)	$9/2^+$	1065(2)	$(5/2)^+$
344(5)	$7/2^-$	112(5)	$(7/2)^+$
373(5)	$5/2^+$	1186(5)	
422(5)	$9/2^-$	1219(2)	$(1/2^+)$
452(2)	$7/2^+$	1281(2)	$3/2^+$ and $5/2^+$
522(2)	$11/2^-$	1351(5)	$(9/2^+)$
552(5)	$9/2^+$	1428(2)	$7/2^+$ and $9/2^+$
552?	$(5/2^-)$	1498(5)	
640?(10)	$(3/2^+)$	1549(5)	
662(5)	$7/2^-$	1815(2)	$(7/2)^-$
678?(10)	$(5/2^+)$	1902(5)	
771(5)	$9/2^-$	1982 (2)	$(11/2)^-$

373.37 keV from the 5/2+ level of the same energy and the 287.79 and 214.0 keV transitions from the $7/2^-$ level at 344.5 keV.

The majority of transitions in ^{163}Tb can be observed in the total projection shown in Figure 4.1 including nine of the 11 previously identified transitions. To provide clear evidence for the remaining transitions, a number of separate gates have been used, some of which will be shown in this work.

Beginning from a gate on the 287.7 keV transition, shown in Figure 4.2(e) and observed with high intensity in the singles spectrum, four of the previously observed transitions, 575.2, 632.8, 1167.8, and 1562.5 keV, are found to be coincident with the 287.7 and 11 additional coincident transitions are observed, 54.0, 81.6, 242.3, 394.7, 675.9, 687.4, 760.9, 768.7, 801.0, 947.5, 1086.2, and 1480.9 keV. The 801.0 keV transition is tentatively placed because of the low intensity and poor agreement between the gate on 287.7 keV transition and the gate on 801.0 keV transition, likely because of the few counts above background in the 801.0 keV gate. This gate and others are consistent with the previous tentative

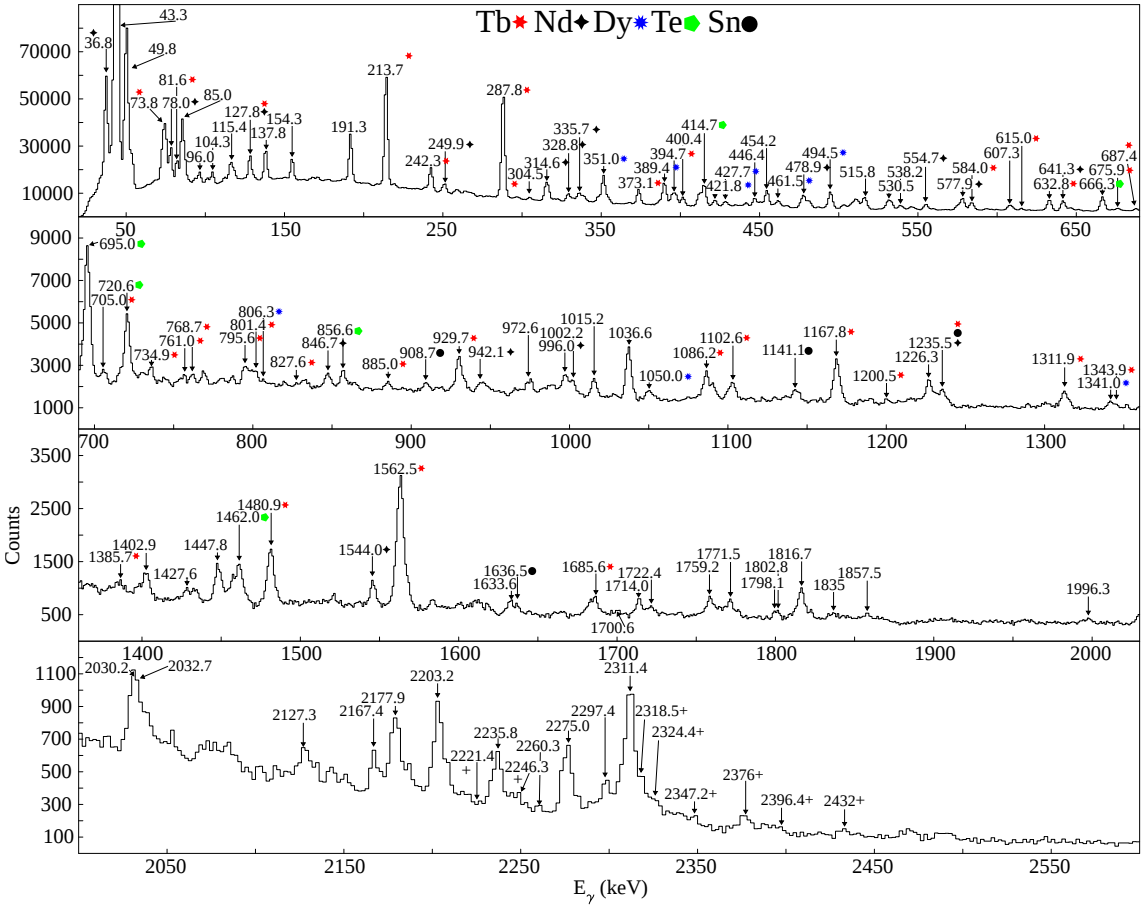

Figure 4.1: Total projection of γ-rays coincident with mass 163 data for all data collected and a coincidence window of 10 μs. The 43.3 and 49.6 keV peaks are produced predominantly by a mix of ^{163}Gd and ^{163}Tb K x-rays. The 36.9 keV peak is from ^{147}Nd K x-rays(NdO). Peaks caused by contaminants have been marked accordingly, transition labels without a symbol correspond to transitions from ^{163}Gd. The (+) indicates a transition which is primarily observed in the singles spectra associated with ^{163}Gd.

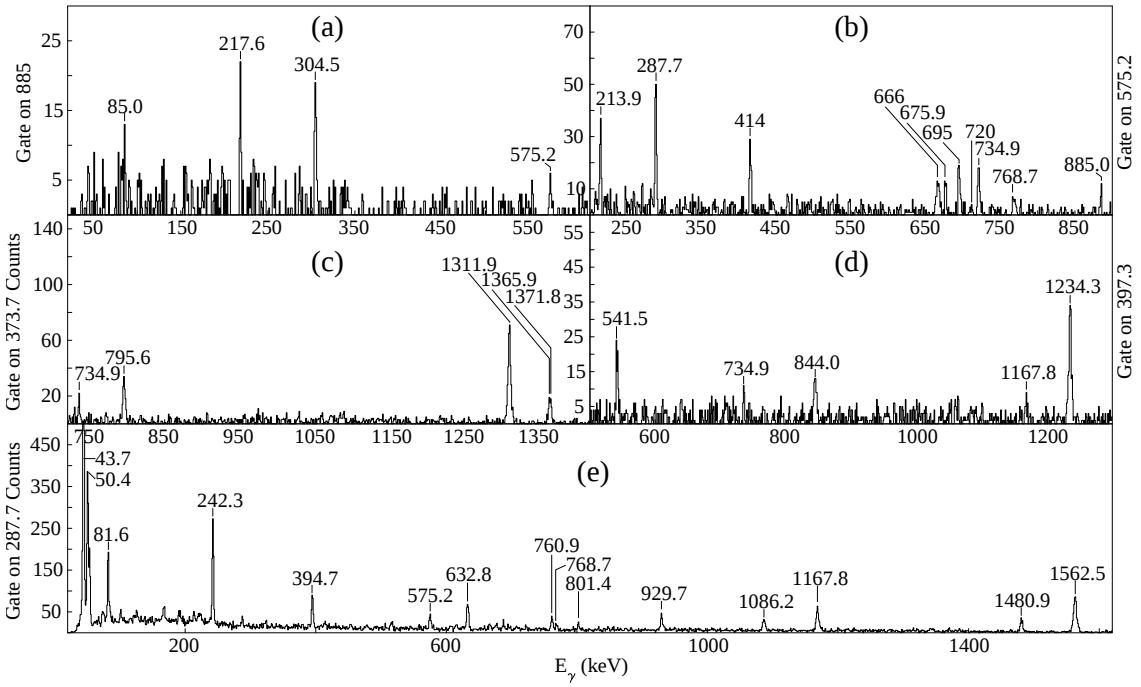

Figure 4.2: Coincidence spectra for gates on ^{163}Tb transitions (a) 287.5 keV, (b) 373.5 keV, (c) 397.5 keV, (d) 575 keV, and (e) 885 keV.

placement of the 213.9 & 287.7 keV transitions and they are thus listed here as confirmed transitions from the 341.7 keV $7/2^-$ level.

Also shown in Figure 4.2 (c) is the gate on the 373.7 keV transition which reveals the coincidence relationship between the previously observed 373.7 keV transition and the previously observed 1311.9 keV transition as well as the new 734.9, 795.6, and 1365.9 keV transitions. The 734.9 and 795.6 keV transitions are sequentially coincident with each other. This pair of transitions forms a connection to the previously observed 1904 keV level while the 1311.9 keV previously observed transition appears to be originating from a new level at 1686 keV.

In Figure 4.2(d) is seen the gate on the 397.3 keV transition which yields observation of the previously identified 1234.3 keV transition and four new transitions of 541.5, 718.0, 844.0, and 1058.2 keV. The coincidence between the 397.3 keV transition and the 1234.3 keV transition is confirmed by the gate on 1234.3 keV transition shown in Figure 4.3(a)

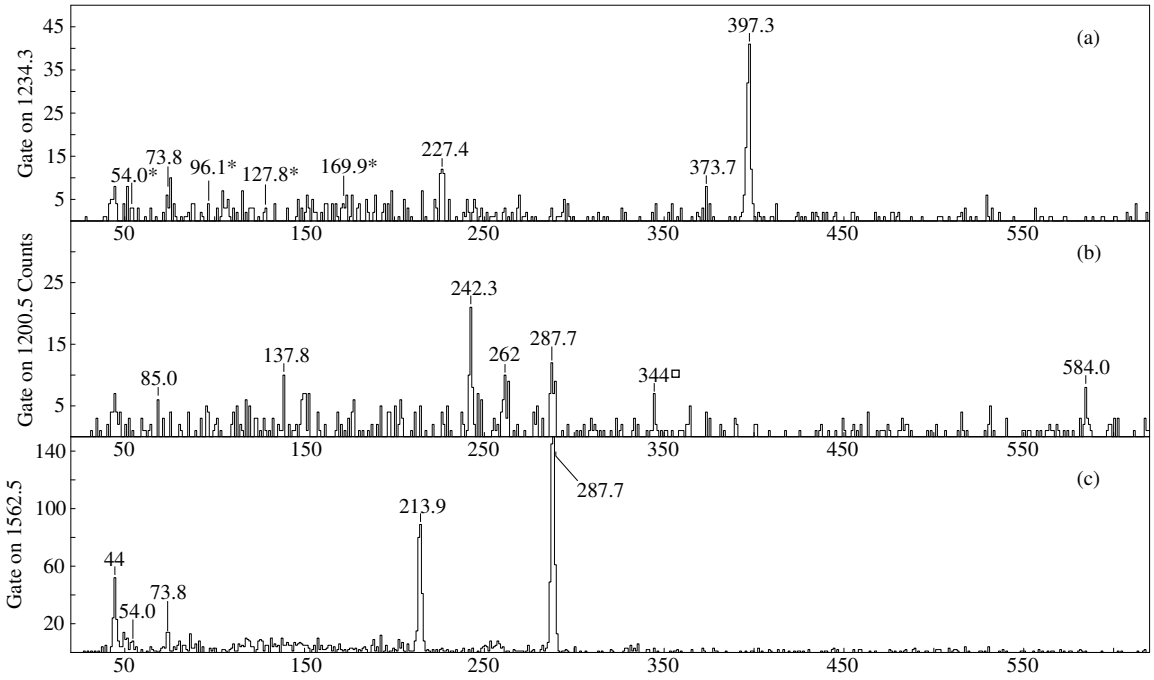

Figure 4.3: Coincidence spectra for gates on ^{163}Tb transitions (a) 1234 keV, (b) 1200 keV, and (c) 1562 keV. *these peaks are below background and belong to transitions better observed in other gates.

which lacks significant transitions besides those of 227.4 and 397.3 keV and further confirms the placement of the 54.0, 397.3, and 1234.3 keV transitions.

The gate on the 575.2 keV transition shown in Figure 4.2(b) confirms the placement of the 575.2 keV transition feeding the $7/2^-$ level at 341.7 keV and reveals two feeding transitions of 675.9 and 768.7 keV, the later of which confirms the placement of the 1685.6 keV transition as feeding the ground state. Gates on both the 675.9 and 768.7 keV transitions, not shown, confirm these placements. Also seen in this gate are the 414, 666, 695, and 720 keV transitions of ^{126}Te, the presences of which are covered in Chapter 4.3.

Shown in Figure 4.2(a) is the gate on 885.0 keV which shows coincidences with two transitions, 217.6 and 304.5 keV, both taken to be tentative. These are presently placed

in the level scheme associated with a set of tentative levels which include the placement of the strong but tentatively associated 1102.6 keV transition. Evidence in the 885.0 and 575.2 keV gates present an alternate placement without relation to the 1102.6 keV level and transition but instead with the 885 keV transition feeding the 916.9 keV level from which the 575.2 keV transition originates. However, the gates on the 217.6 and 304.5 keV transitions do not show a 575.2 keV transition but do show an 885.0 keV transition. It is possible that there is a second $\approx$ 885.0 keV transition or a transition of similar energy either within the structure of ^{163}Tb or an unidentified contaminant, but the coincidence spectra do not offer enough information to confirm either of these possibilities. Thus, these transitions have tentatively been placed without association to the 575.2 keV transition.

From the gate on the 1200.5 keV transition shown in Figure 4.3(b), evidence is observed for the 584.0 keV transition feeding the ground state and the 242.3 keV transition feeding the 341.7 keV level from which the 213.9 keV and 287.7 keV transitions originate. The 213.9 keV transition feeds the 73.8 keV transition which feeds the 54.0 keV level seen in the gate as a shoulder on the 50 keV X-ray peak. Note that these spectra have not been corrected for detector efficiency. Thus, transitions of apparently similar peak heights after correction can be found to be of disparate intensity values as the intensities of higher energy transitions are under represented in the spectra. Also observed are the 85.0, and 137.8 keV transitions from ^{163}Gd which are in coincidence with transitions in ^{163}Gd near or above 1200 keV. Lack of Compton suppression on the Clover detectors greatly extends the energy range over which high-energy transitions from separate isotopes will contaminate gates in the coincidence spectra. Not only gates near the actual energy of the transition but also gates in the Compton continuum will yield contaminant coincidences, see Chapter 1 or Knoll's text on radiation detection [35] for more details on Compton scatter. This is exacerbated when there are a number of high-energy transitions or very intense transitions in the contaminant isotope. Here contaminant meaning any isotope not the one presently being investigated.

Lastly, a gate on the 1562.5 keV transition, shown in Figure 4.3(c), further confirms the location of the 1562.5 keV transition. The key features of this spectrum are first, the clarity, there are few transitions observed which are not presently understood to be coincident with the gating transition, and second, the relative intensity of the 213.7 keV peak and the 287.7 keV peak. Following efficiency correction, these intensities match with the overall observed relative intensity between these two transitions. Such an observation is only possible when the gating transition shares a level with the coincident transitions in question. Therefore, as we know from other gates that the 213.7 and 287.7 keV transitions originate from the same level, the 1562.5 keV transition must feed the level from which the 213.7 and 287.7 keV transitions originate. This gate also provides observation of the 54.0 keV transition on the shoulder of the 50 keV $K_{\beta 1}$ X-ray which only appears poorly in other gates shown. The 1562.5 keV transition provides further evidence for the spin assignments of the ground State, 54.0, and 127.8 keV levels as the higher multipolarity 127.8 keV transition is not observed in strong competition with the heavily converted 73.8 keV transition. This is consistent with the difference in transition probability expected between a 73.8 keV, ΔI=1 transition and a 127.8 keV ΔI=2 transition, although the ΔI=2 transition can be enhanced in rotational bands.

Figure 4.4 shows the level scheme for ^{163}Tb produced as part of this work. Each transition was placed based upon a variety of background subtracted gates in addition to those gates shown here. Where separate gates did not agree, or where a gate on the transition in question yielded too few counts to confirm coincident transitions and the anticipated x-ray spectra, transitions have been placed tentatively according to level spacing or atop the strongest transition whose gate indicates the presence of the transition in question.

Tables 4.2 and 4.3 list every transition observed in ^{163}Tb. The relative intensity referenced to the 287.7 keV transition with uncertainty of the last digit indicated in parenthesis, the internal conversion corrected intensities are also shown along with the multipolarity assumed for calculating the internal conversion correction for those transitions with sufficient

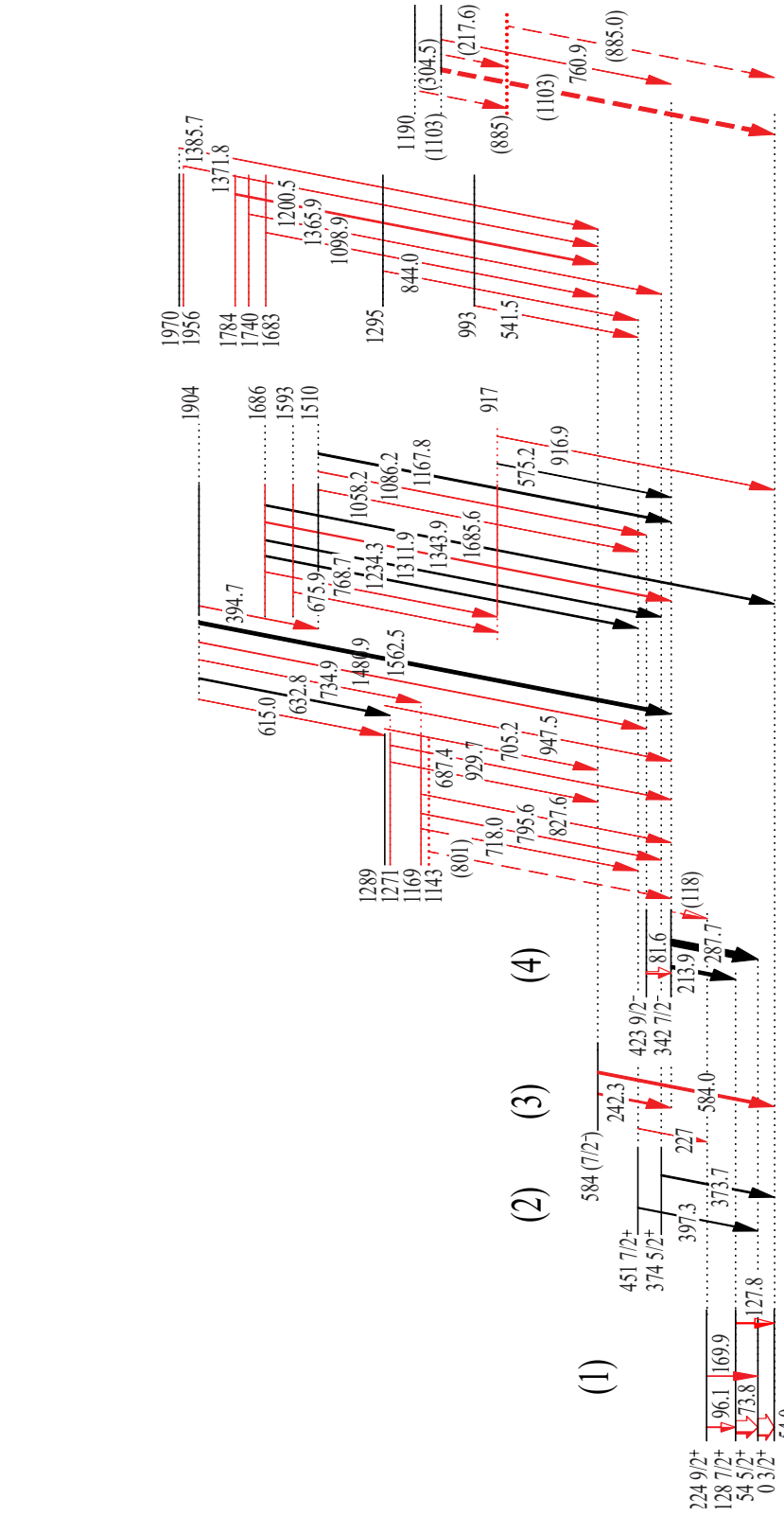

Figure 4.4: Level scheme of ^{163}Tb. New transitions and levels are shown in red, previously identified transitions and levels in black, and tentative transitions and levels are dashed.

Table 4.2: Transitions in ^{163}Tb. Transition energy, intensity, internal conversion corrected intensity, assumed multipolarity, energy and J^π of initial and final levels. J^π assignments adopted from [18, 33, 34].

E_γ (keV)	$I_\gamma(\%)$	$I_\gamma(\%)ICC$	*ICC Multipolarity*	E_i	E_f	J_i^π	J_f^π
54.0	19(4)	268(56)	M1	54.0	0.0	$5/2^+$	$3/2^+$
73.8	5(2)	31(13)	M1	127.8	54.0	$7/2^+$	$5/2^+$
81.6	4.6(5)	23(3)	M1	423.3	341.7	$9/2^-$	$7/2^-$
96.1	19(3)	65(10)	M1	223.9	127.8	$9/2^+$	$7/2^+$
117.8	4.4(7)	10(2)	M1	341.7	223.9	$7/2^-$	$9/2^+$
127.8	7.7(8)	16(2)	E2	127.8	0.0	$7/2^+$	$3/2^+$
169.9	10(2)	14(3)	E2	223.9	54.0	$9/2^+$	$5/2^+$
213.9	46(4)	47(4)	E1	341.7	127.8	$7/2^-$	$7/2^+$
217.6	2.5(9)	3(1)	M1	1102.6	885.0		
227.4	4(1)	4(1)	E1	451.3	223.9	$7/2^+$	$9/2^+$
242.3	12.7(9)	15(1)	M1	584	341.7	$(7/2^-)$	$7/2^-$
287.7	100(3)	102(3)	E1	341.7	54.0	$7/2^-$	$5/2^+$
304.5	4.0(6)	4.1(6)	E1	1189.5	885.0		

internal conversion. The energy of the initial and final levels and the spin of the initial and final levels for those levels with spin assignments is shown in the final two columns.

Table 4.3: Transitions in ^{163}Tb continued.

E_γ (keV)	I_γ(%)	E_i	E_f	J_i^π	J_f^π
373.7	21(1)	373.7	0.0	$5/2^+$	$3/2^+$
394.7	8(1)	1904.2	1509.5		
397.3	14(1)	451.3	54.0	$7/2^+$	$5/2^+$
541.5	3.3(7)	992.8	451.3		$7/2^+$
575.2	5.0(7)	916.9	341.7		$7/2^-$
584.0	36(2)	584.0	0.0	$(7/2^-)$	$3/2^+$
615.0	3(1)	1904.2	1289.2		
632.8	18(1)	1904.2	1271.4		
675.9	6(1)	1592.8	916.9		
687.4	1.0(3)	1271.4	584.0		$(7/2^-)$
705.2	2(1)	1289.2	584.0		$(7/2^-)$
718.0	3.6(8)	1169.3	451.3		$7/2^+$
734.9	3(1)	1904.2	1169.3		
760.9	7(1)	1102.6	341.7		
768.7	7(1)	1685.6	916.9		
795.6	6.8(8)	1169.3	373.7		$5/2^+$
801.4	3.0(7)	1143.1	341.7		$7/2^-$
827.6	0.7(4)	1169.3	341.7		$7/2^-$
844.0	3.5(8)	1295.3	451.3		$7/2^+$
885.0	2.9(7)	885.0	0.0		$3/2^+$
916.9	4.8(9)	916.9	0.0		$3/2^+$
929.7	8(1)	1271.4	341.7		$7/2^-$
947.5	2.6(5)	1289.2	341.7		$7/2^-$
1058.2	0.7(3)	1509.5	451.3		$7/2^+$
1086.2	8(2)	1509.5	423.3		$9/2^-$
1098.9	6(2)	1682.9	584.0		$(7/2^-)$
1102.6	55(3)	1444.3	341.7		$7/2^-$
1167.8	23(2)	1509.5	341.7		$7/2^-$
1200.5	21(6)	1784.5	584.0		$(7/2^-)$
1234.3	20(2)	1685.6	451.3		$7/2^+$
1311.9	20(3)	1685.6	373.7		$5/2^+$
1343.9	1.6(8)	1685.6	341.7		$7/2^-$
1365.9	3.7(8)	1739.6	373.7		$5/2^+$
1371.8	5(3)	1955.8	584.0		$(7/2^-)$
1385.7	6(3)	1969.7	584.0		$(7/2^-)$
1480.9	9.2(8)	1904.2	423.3		$9/2^-$
1562.5	51(3)	1904.2	341.7		$7/2^-$
1685.6	21(1)	1685.6	0.0		$3/2^+$

4.3 ^{163}Tb Discussion

The low-energy level scheme of ^{163}Tb has now been rigorously examined across three previous studies and this present one. However, at higher energies the identification of levels seen in this work that were previously observed is complicated by the uncertainty ranges obtained in the reaction studies [34, 33], shown in Table 4.1. As seen in Figure 4.4, some of the high levels have been indicated as previously observed for cases where the presently observed energy was within the previously published uncertainties, though these assignments may not be accurate because of increasing level density with excitation. These may be states different from those observed in reaction studies. Additionally, a number of the states previously indicated as doublets were not observed as such in this work. This again is more likely because β decay is populating single particle states of similar energy not because of inaccuracy of previous work. Within the scope of only γ coincidence, it may be best to list these as newly observed states until some spin measurement can be made of the levels to confirm they are the same states.

As previously mentioned in Chapter 3.1, data were collected both for a saturation measurement and with a tape cycle during the experiment. During the early stages of this study, these data were analyzed as a single set using a ten microsecond event window for coincidence. Incorporation of the saturation measurement with the tape cycle data and the large event window allowed for clear identification of contaminant beam constituents. Because the saturation measurements duration was an order of magnitude longer than the half life of ^{163}Gd, the saturation measurement duration was 46 minutes and the half-life of ^{163}Gd is 68(3)seconds [18]. The intensity of the ^{163}Tb γ transitions were thus greatly enhanced relative to all other beam constituents. The discovery work on ^{163}Tb was primarily based on this combined data set. Intensities and energy fittings were then performed with only tape cycle data, to reduce the effect of contaminant transitions on these measurements. Shown in Figures 4.6 and 4.5 are the coincidence projections for the tape cycle only data and the combined data sets, respectively.

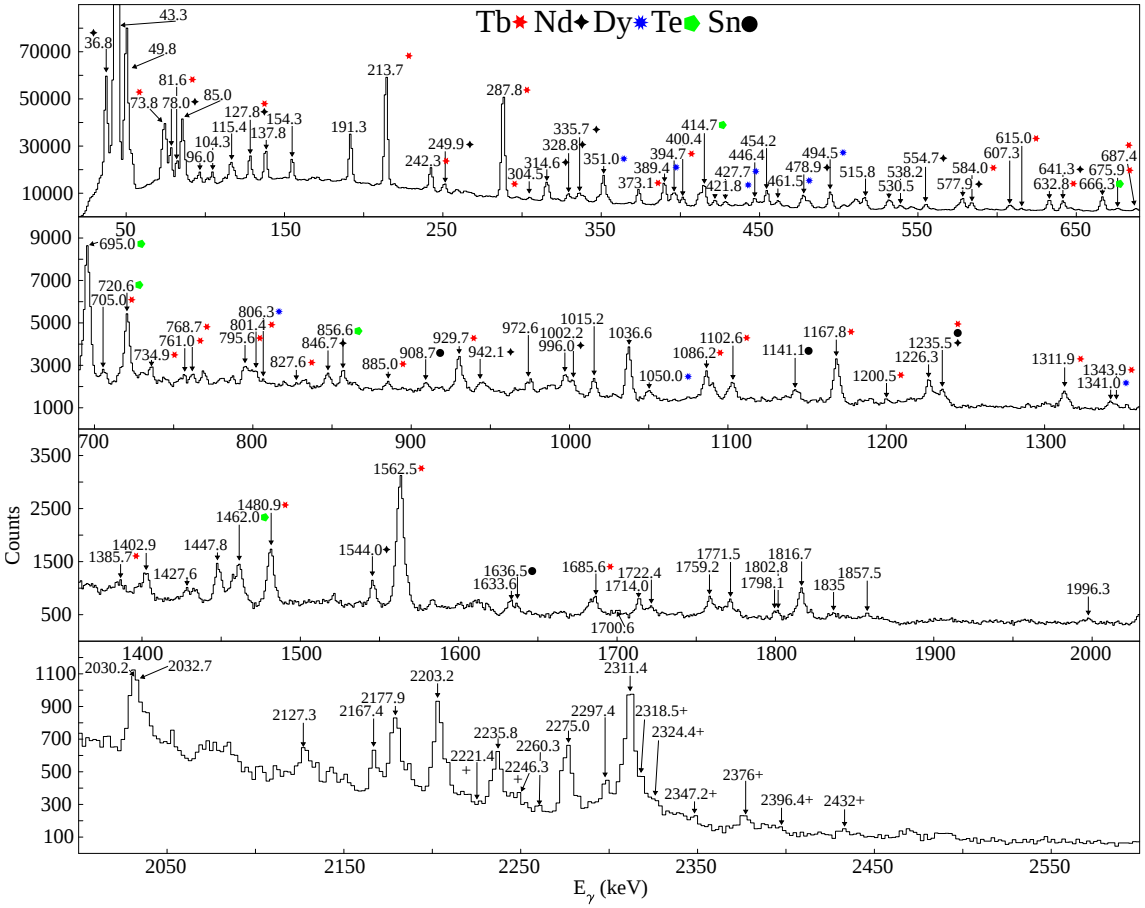

Figure 4.5: Total projection of γ-rays coincident with mass 163 data for all data collected and a coincidence window of 10 μs. The 43.3 and 49.6 keV peaks are produced predominantly by a mix of ^{163}Gd and ^{163}Tb K x-rays. The 36.9 keV peak is from ^{147}Nd K x-rays(NdO). Peaks caused by contaminants have been marked accordingly, transition labels without a symbol correspond to transitions from ^{163}Gd. The (+) indicates a transition which is primarily observed in the singles spectra associated with ^{163}Gd.

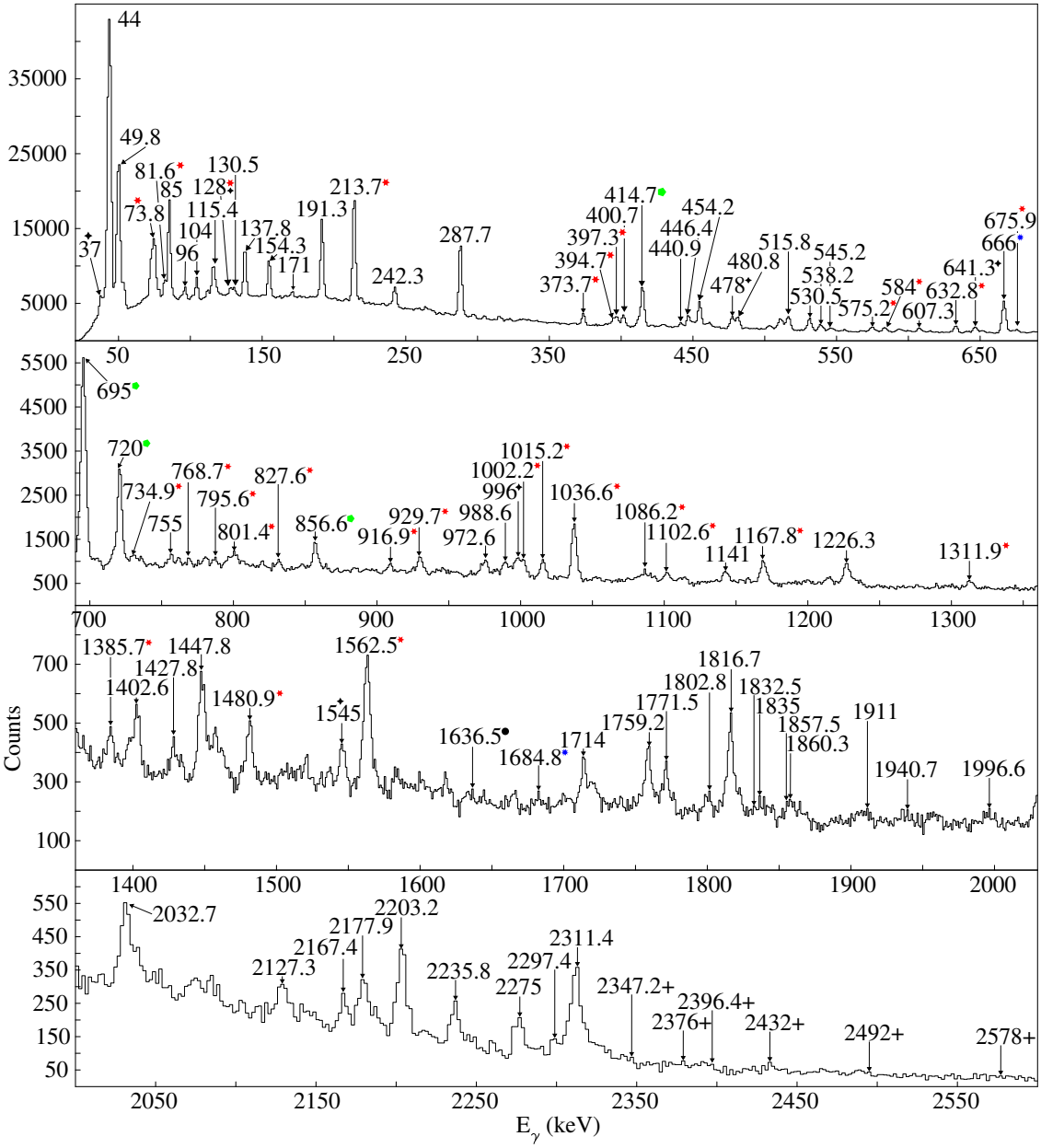

Figure 4.6: Total projection of γ-rays coincident with mass 163 data for only tape cycle data and a coincidence of 300 nanoseconds. The 43.3 and 49.6 keV peaks are produced predominantly by a mix of ^{163}Gd and ^{163}Tb K x-rays. The 36.9 keV peak is from ^{147}Nd K x-rays (NdO). Peaks caused by contaminants have been marked accordingly, transition labels without a symbol correspond to transitions from ^{163}Gd. The + indicates a transition which is primarily observed in the singles spectra.

Note, ^{147}Nd(NdO), and ^{163}Dy have been identified clearly as beam contaminants. Additionally, ^{126}Te and ^{126}Sn activities was accumulated near the CARDS as part of a previous experiment, and contaminant transitions from these isotopes are also observed. Some observations were made of weaker transitions from ^{147}Pr but these were negligible contributions to the 300 nanosecond coincidence window data. Contributions from the ^{147}Nd had the benefit of the clearly identifiable K x-ray transition at 36.8 keV. As the neodymium characteristic x-rays are of clear energy difference from those of gadolinium and terbium, 42.8 keV and 43.4 keV, it was a simple matter to confirm when contributions from ^{147}Nd were present. However, the earlier practice of disregarding peaks that were known to be present in ^{147}Nd ultimately came back to hamper progress as was found in the observation of the 475.7 keV and 476.3 keV transitions, which lay in close proximity to the 478 keV transition in ^{147}Nd, as discussed in Chapter 3.5.

Fortunately, it has not been observed that similar problems arose from the presence of ^{126}Te and ^{126}Sn. This is largely because the near spherical structure of these nuclei results in their first excited states being higher in energy and resulting in fewer transitions. With fewer transitions per decay, not only was there less opportunity to interfere with the investigation of ^{163}Gd and ^{163}Tb, but there was also less likelihood of them even being observed in coincidence. Furthermore, all of the contaminant isotopes listed here lie closer to the line of stability and have been well studied. Thus, with the exception of cases where transitions lie very close in energy, as the example in the previous paragraph, interference from these contaminant isotopes were clearly identified.

Shown in Table 4.4 are the γ-feeding and outflow values observed for ^{163}Tb. These feeding and outflow values can be used to estimate β-feeding which would manifest as an excess of γ-outflow compaired to γ-feeding. For known odd parity states, there is limited observed β-feeding, this is consistent with the current proposed ground state for ^{163}Gd of $7/2^+$. As further evidence for the proposed ground state spin assignment of ^{163}Gd the states with the highest apparent β-feeding are the allowed spin 0 transition from a parent ground

Table 4.4: Internal Conversion Corrected γ Feeding and γ Outflow in ^{163}Tb. J^{π} assignments adopted from, [18, 33, 34].

E_{Level} (keV)	γ Feeding	γ Outflow	J^{π}	E_{Level} (keV)	γ Feeding	γ Outflow	J^{π}
0.0	424(67)	0(0)	3/2+	1169.3	3(1)	11(2)	
54.0	161(20)	268(56)	5/2+	1189.5	0(0)	4.1(6)	
127.8	112(14)	47(14)	7/2+	1271.4	18(1)	9(1)	
223.9	15(3)	79(13)	9/2+	1289.2	3(1)	5(2)	
341.7	138(13)	160(9)	7/2-	1295.3	0(0)	3.5(8)	
373.7	30(5)	21(1)	5/2+	1509.5	8(1)	31(4)	
423.3	17(3)	23(3)	9/2-	1592.8	0(0)	6(1)	
451.3	32(4)	18(2)	7/2+	1682.9	0(0)	6(2)	
584.0	42(15)	51(3)	(7/2-)	1685.6	0(0)	70(8)	
885.0	7(2)	2.9(7)		1739.6	0(0)	3.7(8)	
916.9	13(2)	9(2)		1784.5	0(0)	21(6)	
992.8	0(0)	3.3(7)		1904.2	0(0)	92(8)	
1102.6	0(0)	65(6)		1955.8	0(0)	5(3)	
1143.1	0(0)	3.0(7)		1969.7	0(0)	6(3)	

state of $7/2^+$ to a daughter state of $7/2^+$ and the ΔI=1 allowed β transitions to the $5/2^+$ and $9/2^+$.

An isomeric transition may be implied by the discrepancy in feeding and outflow observed for the 54 keV $5/2^+$ state. However, the error is sufficiently large because of the large uncertainty involved in obtaining the total relative intensity for the 54 keV transition which is the only observed, and only anticipated transition out of this state, that this apparent lifetime is likely due either to over estimation of the outflow or under observation of the feeding. A similar explanation is available for the 451.3 keV $7/2^+$ state as an in band transition would be possible for this state though one is not observed. While no transition is observed at 77.6 keV, this transition intensity would be weak and strongly internally converted. Thus, the difference in feeding compared to observed outflow from the 451.3 keV $7/2^+$ level is expected to be related to unobserved internally converted transitions out of that state. Similarly, the discrepancy between observed feeding and outflow for the 373.7 keV $5/2^+$ level are more likely related to unobserved weak transitions than to an isomeric

state. An excess of feeding is also observed for the 1271.4 keV level. It is anticipated that this level like the 373.7 keV $5/2^+$ and 451.3 keV $7/2^+$ also has unobserved transitions depopulating this level.

Further evidence for the $1/2^-$ band head at 137.2 keV in ^{163}Gd being an isomer would have been observation of enhanced β-feeding of $1/2^+$ and $3/2^-$ levels in ^{163}Tb. However, both lack of spin information for the higher lying states in ^{163}Tb and lack of a lifetime measurement for the $(137.2)(1/2^+)$ state in ^{163}Gd interfere with observation of preferential feeding. The lack of spin information prevents confirmation that a higher energy state that is receiving β-feeding is in fact $1/2^-$ or $3/2^-$ as would be expected. With the lifetime of the (137.2) keV $(1/2^-)$ isomeric state estimated at 14 seconds, as discussed in 3.4 and the expected β-decay from the state being $\approx 0.4\%$, β-feeding enhancement may be less than is measurable, as the predominant depopulation of the isomer is likely γ-decay to the ^{163}Gd ground state.

Chapter 5

^{157}Sm

5.1 Introduction

Kleinheinz, *et al.* [36] proposed that intruder and extruder states explain the onset of deformation near A≈150. Urban, *et al.* [37] investigated the 11/2$^-$[505] neutron extruder state in ^{159}Sm in comparison with systematics of several nearby A≈150 nuclei with the 11/2$^-$[505] neutron extruder state to extend the description of deformation onset as related to extruder states. Similarly ^{157}Sm was studied by Hwang, *et al.* [38] to observe the theoretically expected 3/2$^-$[521], 5/2$^+$[642],5/2$^-$[523], and 11/2$^-$[505] bands. However, from the eight γ-rays Hwang *et al.* proposed, only one extended band in ^{157}Sm was reported based on the ground state assignment from β-decay studies [6]. The isomeric state associated with the 11/2$^-$[505] neutron extruder state was not observed. Since Hwang's analysis, new software tools have been implemented by Wang [39], described in Chapter 5.2, which allowed further investigation of ^{157}Sm. This study of ^{157}Sm builds upon the work by Hwang, *et al.* and finds an additional 35 transitions, re-locating a number of Hwang's observed transitions and extending the high spin band structure of both the (3/2$^-$) and (5/2$^+$) bands.

5.2 Methods

In August and November of 2000, a 62μCi ^{252}Cf source, which undergoes α-decay for 97% of decay events and spontaneous fission (SF) for 3% of decay events with a half-life of 2.65 years, was studied with the Gammasphere for observations of SF over the course of a total of 4 weeks. The ^{252}Cf source was deposited on a 10 mg/cm^2 iron foil then covered with an additional 10 mg/cm^2 iron foil, and further encased in a polyethylene sphere 7.72 cm in diameter, to absorb β-rays and conversion electrons. During these observations, 101

of Gammasphere's possible 110 high purity germanium (HPGe) detectors were used with the bismuth germanate (BGO) Compton suppression system. The source was placed at the center of the Gammasphere with heavy metal filters in place on the face of the BGO crystals but without foil absorbers covering the HPGe detectors. Further details on the experimental setup can be found in the work by Luo, *et al.* [40].

Data analysis of the $5.7x10^{11}\gamma-\gamma-\gamma$ and higher fold events observed with the Gammasphere was performed with tools from the RADWARE software package [21]. These data were assembled into a symmetric data volume allowing for up to two projection gates to be made simultaneously. Not only does the ability to make two projection gates from the Gammasphere data greatly reduce the influence of many similar energy transitions observed coming from a SF source, the ability to make two projections greatly expedites analysis within the structure of a single nucleus. Additionally, the data were analyzed with hypercube software as described in the doctoral thesis of Enhong Wang [39]. This data cube of $1.9x10^{11}\gamma-\gamma-\gamma-\gamma$ and higher fold coincident events allows a further projection gate to be made beyond the two already possible with the earlier data cube. Such a triple gate allows for significant reduction in background signals to make observation of comparatively weakly populated states possible.

As the data for this study were obtained from γ-ray observations following fission, there were two main approaches for selection of coincidence gates. The first, and more easily applied method, is to simply begin with gates on previously identified γ-ray transitions within the nucleus of interest. Alternatively, for those cases where no transitions are known within the isotope of interest, there are also coincident γ-rays from the partner fission fragments. For any given isotope produced in fission there are as many different partner isotopes as there are variations in neutron multiplicity, one for each different number of prompt neutrons emitted. It is possible to use known transitions for the 3 to 5 neutron channel partner fragments to assemble a spectrum which consists predominantly of transitions in the isotope of interest. This is possible due to the mean number of neutrons emitted in ^{252}Cf SF

and the range of neutron numbers for a best fit would change according to the dynamics of the specific fission process being used. Gating on known transitions to ground in $^{90-92}$Kr for the 5, 4, and 3 neutron channels produces a set of spectra which contain observations of the coincident transitions for each of the krypton isotopes as well as transitions from the samarium fission partners. Thus, each of these spectra individually contain a large amount of information. While this breadth of information does make it impossible to use fission data for analysis of isotopes which have no known transitions in either the isotope of interest or its predominant fission partner, it does offer a great wealth of information useful to extending the structures for those isotopes for which some starting point is known. As there were previous findings for ^{157}Sm, the first approach was to gate upon known γ-rays in this study.

In addition to providing a means of creating spectra for extending nuclear structure of their partners, the relationship between the fission fragments are also used to confirm from which nucleus the transitions are originating. Thus, all transitions proposed have been confirmed in multiple coincidence spectra and the intensities of the relevant fission partners have been observed in gates on the transitions in question. Transitions where all of these confirmations were not observed have been listed tentatively. In this work tentative transitions in a level scheme are illustrated with dashed arrows and tentative energies, spins, and parities are listed in parenthesis.

5.3 ^{157}Sm Results

Starting from the high spin structure established by Hwang *et al.* [38], shown in Figure 5.1, γ-γ-γ-γ coincidence analysis was implemented to extend the known structure of ^{157}Sm and make observation of the $11/2^-[505]$ isomeric state. Study of the high spin structure benefited greatly from the γ-γ-γ-γ coincidence data, allowing for simultaneously gating on x-rays from ^{157}Sm, transitions from krypton fission partners, and a known transition from within ^{157}Sm. Such a set of simultaneous gates provides much greater clarity for states

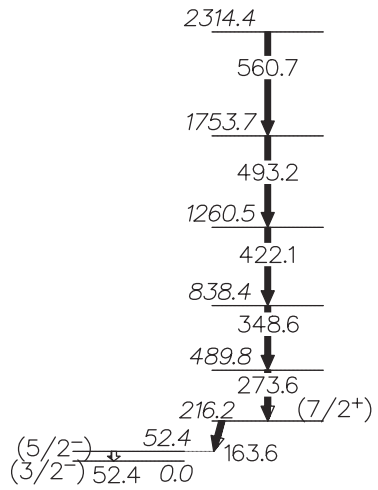

Figure 5.1: Level scheme for ^{157}Sm as previously observed by Hwang *et al.* [38].

rarely populated or for isotopes with low yields as the additional coincidence gate brings transitions which would otherwise be obscured by the background into clear view.

The structure of ^{157}Sm proposed in this work is shown in Figure 5.2. Note that the convention in the ^{157}Sm scheme separates bands graphically into ΔI=2 components. Here the (1) and (2) bands belong to the (3/2$^-$) ground state band and the (3) and (4) bands belong to the (5/2$^+$) band. The proposed structure breaks up those transitions previously identified by Hwang *et al.* shifting the ΔI=2 transitions above the (7/2$^+$) state observed by Hwang, *et al.* up by three units of spin, and assigning these transitions to the (5/2$^+$) band proposed by β-decay studies [6].

For the ground state band, Figure 5.3 frame (b) illustrates observations made in coincidence with the 208.2 keV transition from the (11/2$^-$) state in band (1) in frame (b) and frame (a) shows transitions coincident with the 247.7 keV transition from the (13/2$^-$) level in band (2). Each of these coincidence spectra have further gates set on the 40.3 keV samarium Kα_1 x-rays and the 707.1 keV ground state transition in ^{90}Kr, the 5 neutron fission partner. Seen in the Figure 5.3 frame (a) is evidence for the 166.9, 326.3, 364.5, 401.7, 437.9, and 474.1 keV $\Delta I = 2$ transitions, the 73.3, 93.6, 155.1, 171.2, and 193.3 keV M1

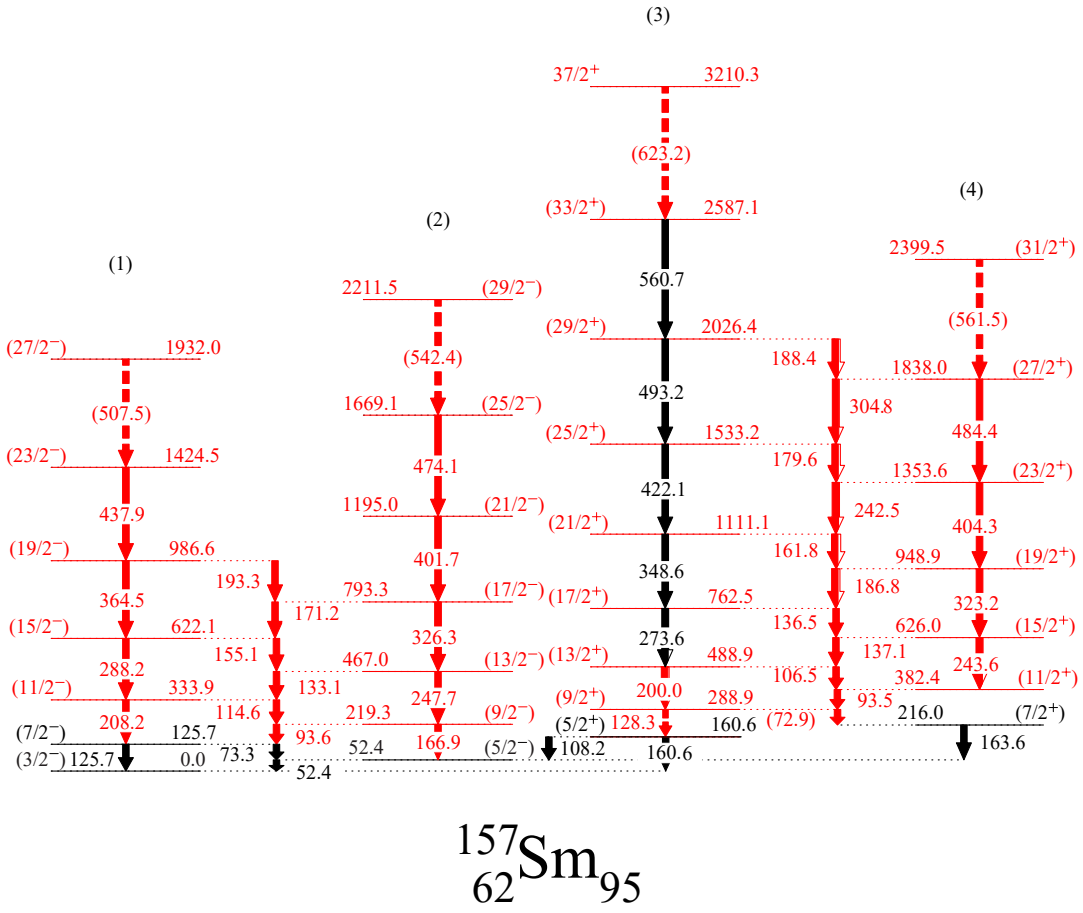

$^{157}_{62}Sm_{95}$

Figure 5.2: Level scheme for ^{157}Sm. Previously observed transitions and levels shown in black, new transitions shown in red.

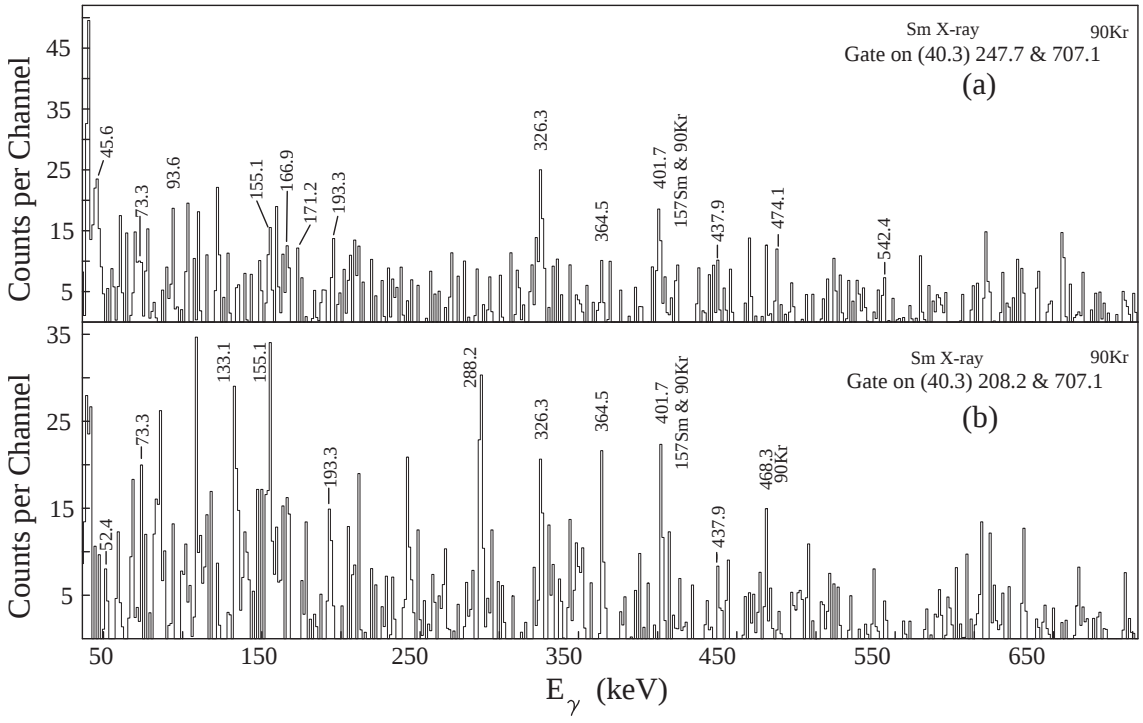

Figure 5.3: Coincidence spectra for transitions in band (1) and (2) in ^{157}Sm. γ-γ-γ-γ coincidence employed with gate energies listed in the top right corner of plot.

transitions and the 45.4 Kb_1 x-ray and the tentative (542.4) keV tentative $\Delta I = 2$ transition. Seen in the bottom frame is evidence for the 288.2, 364.5, and 437.9 keV $\Delta I = 2$ transitions as well as the 52.4, 73.3, 133.1, 155.1, and 193.3 keV $\Delta I = 1$ transitions. Each of these transitions are further confirmed in several other gates involving transitions in the same bands, with the exclusion of the (507.5) and (542.4) keV tentative transitions which lacked sufficient confirmation in multiple gates. Additionally, transitions have been investigated to confirm that they conform to expected intensity trends according to their location in the structure. It may be noted that no evidence for the 114.6 keV transition is seen in these gates; however, the 114.6 keV transition is not in coincidence with either gates illustrated.

Similarly, the observations in the $(5/2^+)$ band can be detailed in a single pair of gates shown in Figure 5.4. The top frame of Figure 5.4 is a plot of transitions coincident with

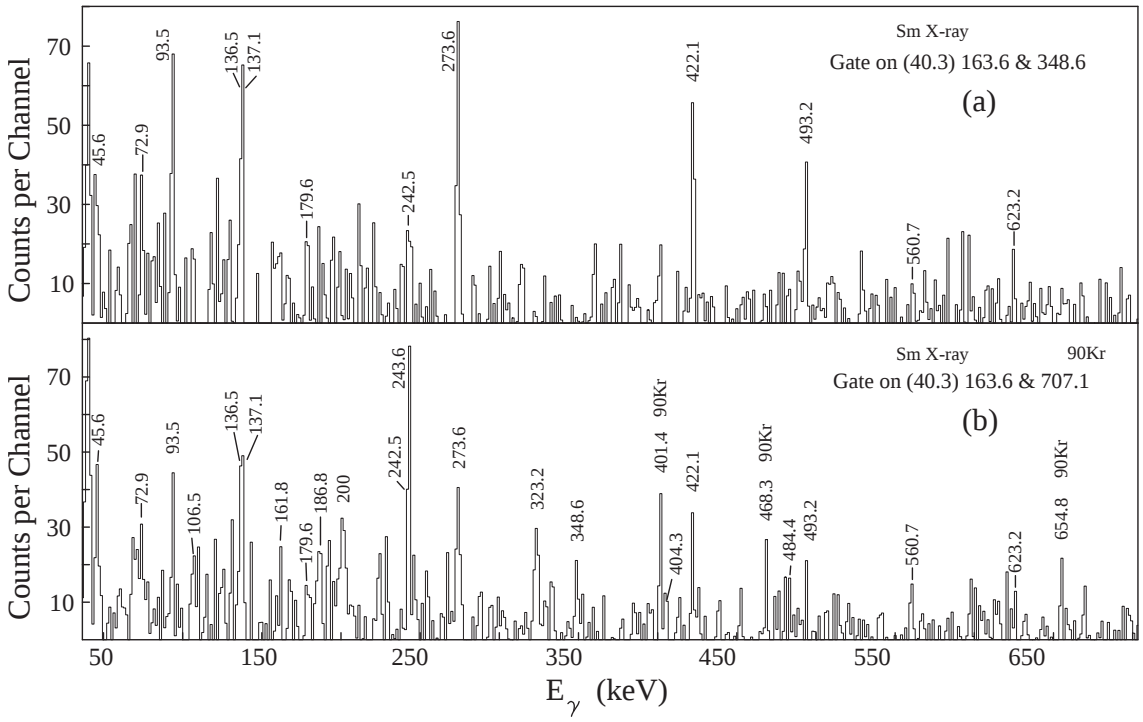

Figure 5.4: Coincidence spectra for transitions in band (3) and (4) in ^{157}Sm. γ-γ-γ-γ coincidence employed with gate energies listed in the top right corner of plot.

40.3 keV samarium Ka_1 x-rays the 163.6 keV $\Delta I = 1$ transition from the $(7/2^+)$ level and the 348.6 keV $\Delta I = 2$ transition from the $(21/2^+)$ level in band (3). The bottom frame of Figure 5.4 is a plot of transitions coincident with 40.3 keV samarium $K\alpha_1$ x-rays the 163.6 keV $\Delta I = 1$ transition from the $(7/2^+)$ level in band (4) and the 707.1 keV transition to ground in ^{90}Kr. Seen in frame (a) is evidence for the 273.6, 422.1, 493.2, and 560.7 keV $\Delta I = 2$ transitions as well as the 72.9, 93.5, 136.5, 137.1, 179.6, and 242.5 keV $\Delta I = 1$ transitions, the 45.4 $K\beta_1$ x-ray and the tentative (623.2) keV $\Delta I = 2$ transition. Seen in frame (b) is evidence for the 200.0, 243.6, 273.6, 323.2, 348.6, 404.3, 422.1, 484.4, 493.2, and 560.7 keV $\Delta I = 2$ transitions, as well as the 72.9, 93.5, 106.5, 136.5, 137.1, 161.8, 179.6, 186.8, and 242.5 keV $\Delta I = 1$ transitions and the 45.4 $K\beta_1$ x-ray and the tentative (623.2) keV $\Delta I = 2$ transition.

In summary, new observations in ^{157}Sm have extend two high spin bands with band heads of the $(3/2^-)$ ground state and the first excited $(5/2^+)$ state. These assignments are based upon level observations from β-decay studies [6], systematics with ^{155}Sm [41] and ^{159}Sm [42] shown in Figure 5.5, and available Nilsson orbitals.

5.4 ^{157}Sm Discussion

With the recent extension of ^{159}Sm's high spin structure [42], and the yet undiscovered $11/2^-[505]$ isomer in ^{157}Sm, there were three primary goals for this investigation of ^{157}Sm. Extension of the ground state band to high spin, identification of the signature partner band for the $7/2^-$ band identified by Hwang *et al.*, and discovery of the lifetime and energy of the $11/2^-[505]$ isomeric state in ^{157}Sm. These first two objectives were met though no observation was made of the isomeric $11/2^-$ state.

With the extension of the ground state band the systematics for the neutron rich samarium isotopes has now been extended. Systematics of ^{157}Sm with ^{155}Sm and ^{159}Sm are shown in Figure 5.5. For comparison, the $5/2^-$ ground state and levels in ^{159}Sm have been normalized to the $5/2^-$ energy in ^{157}Sm. Note, for N=93 in^{155}Sm, the next available Nilsson orbital is the $3/2^-$, and the systematics shown indicate the same is true for ^{157}Sm while for N=97 ^{159}Sm, the next available Nilsson orbital is $5/2^-$. Good agreement is observed for the energy levels in the ground state bands in ^{155,157,159}Sm (less than 10 keV difference up through $13/2^-$). There is a small decreasing excitation with increasing neutron number, consistent with increasing deformation.

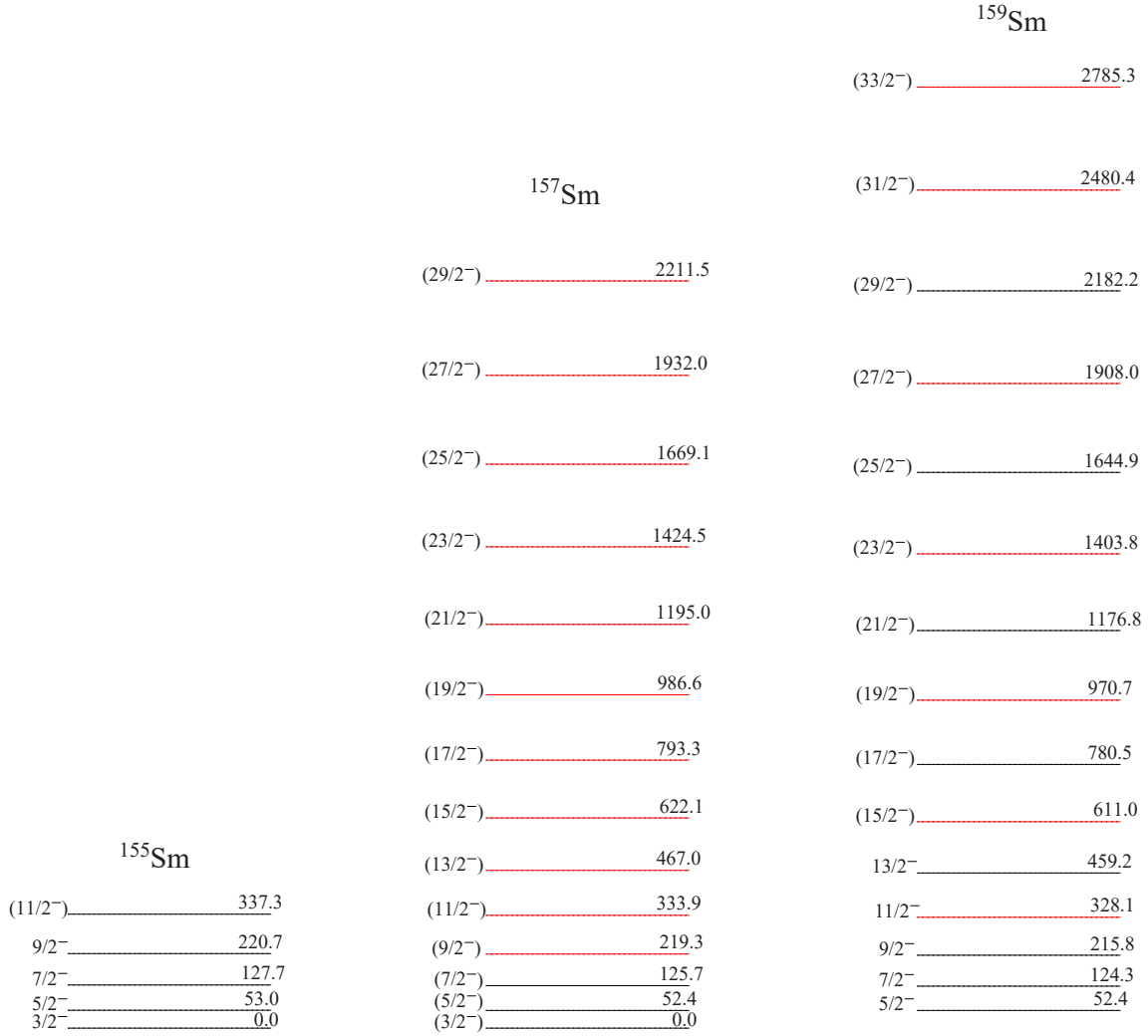

Figure 5.5: Systematics of $^{155,157\&159}$Sm. Levels in ^{159}Sm have been normalized to a ground state energy of 52.4 keV found in ^{157}Sm. New levels shown in red, previously identified levels shown in black. New levels in ^{159}Sm from publication in process [42].

Chapter 6

Fission Dynamics Via SF

6.1 Background

Significant progress in the study of low-energy fission process can be achieved by combining prompt γ-ray spectroscopy with the measurements of the masses and energy distributions of fission fragments. Such an experiment enables one to obtain direct information on the excitation energy of the fission fragment pairs and the distribution between collective and internal degrees of freedom as well as the nuclear structure influence, and actual deformation at the instant of scission.

In contemporary nuclear physics research, many observable properties of fissile nuclei carry fundamental information on the pathways in multidimensional collective space corresponding to the different final mass splits obtained in experiments. Theoretical approaches [43, 44, 45] are at a level where a number of important aspects of the fission process, such as fission barriers, collective inertia, nuclear viscosity, and generation of fragment angular momentum can be calculated on the basis of a fully microscopic description of the nuclear fission process.

Spontaneous fission studies offer preferable conditions to test the theoretical results because of the well defined 0^+ initial state of the even-even fissile nucleus, e.g. ^{252}Cf. A significant argument in favor of spontaneous fission is the absence of an additional term added to the excitation of internal degrees of freedom at the descent to scission as alternate induced fission modes require exciting the nucleus. As modeling efforts for the fission process become more advanced [46, 47, 48, 49, 50], access to the precision measurements of fission observables becomes critical to continued improvement of model accuracies. According to the universally recognized concept of fission dynamics, when the nucleus executing the sub-barrier tunneling comes to the exit point from under the fission barrier, it

evolves towards the appearance of the two nascent fragments moving down to the rupture of the neck connecting them. As the Coulomb energy V_{Coul} decreases, the deformation energy V_{Def} increases, and the sum (V_{Coul}+V_{Def}) is the energy which is bound as potential energy at scission. The total available energy is the Q-value of the fission reaction. Therefore, the energy still free for the excitation of collective or intrinsic degrees of freedom is the difference $E_{Free} = Q - (V_{Coul} + V_{Def})$. In the framework of the Scission Point Model [51], the energy values V_{Coul}, and V_{Def} are calculated assuming that immediately after the neck scission there are two spheroid-shape fragments with a tip distance between them kept constant.

For the most probable region of the mass split observed in the ^{252}Cf spontaneous fission near the heavy fragment mass $A_H \approx$ 135 - 155, the E_{Free} value takes about 30 MeV. The known multiplicity of prompt neutrons emitted by the fission fragments, M_γ = 3.75, is used to make the conclusion that the major part of this energy applies to the thermal excitation of fission fragments. For a typical SF event, 5-6 MeV is left for the excitation of collective degrees of freedom. The known sizable values of fragment angular moments point at a picture with the spin bearing modes (the bending and wriggling oscillations) excited on the way to the scission point. Another collective degree of freedom taking a part of the E_{Free} value could be the kinetic energy of E_K^{sci} acquired by the nascent fragments just by coming to the scission point. It is reasonable to assume the relation TKE=(V_{Coul}+V_{Def}) is valid for the total kinetic energy (TKE) measured for the pairs of fragments detected at fission. In the region of prevalent yields obtained in the ^{252}Cf spontaneous fission, confined between TKE = (170-200) MeV and $A_H \approx$ 135 -155, the part of E_K^{sci} in the TKE value appears to be small.

Assuming that viscosity appears at the descent, one should admit that the two fragments emerging at the scission may have thermal excitation in addition to the excitation energy stored in their deformation. In the case of the ^{252}Cf spontaneous fission, rough estimations taking into consideration the differences in the yields of fission fragments with even-odd

proton or neutron numbers give a few MeV value for the thermal excitation appearing due to the energy dissipation produced by friction.

In fact, the even-odd effects are well observed in the low-energy fission. Its numerical value is presented as $\delta_{Z/N} = (Y_e - Y_o)/(Y_e + Y_o)$ with Y_e and Y_o the yields of fragments with even and odd proton or neutron numbers, respectively. However, it remains open to question whether these measured alternating yields of fragment pairs testify to the friction manifestation or the descent to the scission point as adiabatic with nucleon pairs remaining intact. Moreover, there are important facts calling into question the assumption that the adiabatic model is appropriate to the low-energy fission of even-even nuclei [52]. According to this model, the descent from the saddle to scission is super-fluid, and the pair breaking happens at the moment of the non-adiabatic neck rupture.

TKE values measured for the ^{252}Cf spontaneous fission in the vicinity of the mass splits with $A_H \approx$ 135-155 cover a range extending from TKE $\approx$ 130 MeV to the maximum values coming close to the fission reaction Q value (see e.g. in [53]). Events with TKE approaching within a few MeV of the total energy release are called true cold fission. The specializing "true" tells that these are the fission events where the most compact scission configuration is realized and the number of prompt fission neutrons is zero. The first direct observation of these cold neutronless binary fragmentations in spontaneous fission of ^{252}Cf was made with the multiple germanium detector Compact Ball facility at Oak Ridge National Laboratory [54, 55]. A puzzle occurring with the true cold fission of ^{252}Cf is that the yields of fission fragment pairs with Z_L+Z_H=98 clearly show negative values of the even-odd effect δ_N: the yields of fragments with odd neutron numbers are remarkably prominent [54, 56]. The measurement of fragment charges in true cold fission provides evidence that the above puzzle is a general phenomenon with novel implications for our understanding of fission (see [52] and references therein).

When TKE approaches the lowest obtainable limit going below 140 MeV (see Figure 12 in [53]), a maximum energy becomes stored in the deformation of nascent fragments. This

fission mode was revealed in earlier work [55, 56] where high neutron-multiplicity yields of Ba-Mo fragment pairs were obtained in the spontaneous fission of ^{252}Cf. Recently, the neutron multiplicity yields of Ba-Mo, Ce-Zr, and Nd-Sr have been studied again [57] with improved precision by using the $\gamma-\gamma-\gamma-\gamma$ coincidence cube [39], as well as the $\gamma-\gamma-\gamma$ data and the latest level structures of these nuclei. The results clearly confirm that the Ba-Mo yield data have a hot fission mode where 8, 9, and 10 neutron evaporation channels are observed which are not in the other channels. This mode can indicate that ^{144}Ba is likely hyper-deformed at scission giving rise to such high neutron multiplicities. An extreme case appearing to be attainable in spontaneous fission, corresponds to cold deformed fission, which has been the subject of discussions for a long time [52]. However, whether the most deformed scission configuration is actually attained both with the kinetic energy E_K^{sci} and thermal excitation E_{th}^{sci} occurring to be zero at scission has to be answered by experimental observations.

Additionally, fission is an important source of neutron-rich nuclei where the fragments cover a wide range of isotopes with A $\approx$ 70-180 and Z $\approx$ 28-66. This range covers a wide variety of structural properties of nuclei from spherical double magic to strongly deformed double magic. This experiment will provide further opportunities for the study of these nuclei.

6.2 Goals

The primary goals of the proposed fission dynamics experiment are as follows:

Determination of values for the independent yields of more than 150 individual secondary, appearing after neutron evaporation, fragment pairs of the seven most probable charge splits (Z_L/Z_H = 46/52, 44/54, 43/55, 42/56, 41/57, 40/58, and 38/60) occurring in the spontaneous fission of ^{252}Cf. For the first time, the yields obtained for the individual charge splits will be attributed to specific narrow ranges of the the fission-fragment total kinetic energy distribution starting with $(\mathrm{TKE})_{min} \approx 100$ MeV and extending to TKE coming

close to the total energy release obtained at these charge splits.

Estimation of the viscosity effect appearing at the descent to the scission point. This is done by finding the primary fragment pairs which contribute to the yields of the secondary fragment pairs. By examining correlations between these primary pairs and obtained TKE bands, the determination of the thermal-excitation energy (E_{th}) spectra of these primary fragments is possible. By locating the primary fragment pairs, the whole studied energy range is covered with a band width of Δ(TKE) $\approx$ 15-20 MeV. This combination yields data that has not been available before. It is anticipated that separation of the part E_K^{sci}, kinetic energy acquired just by coming to the scission point, from the fragment TKE is possible with these data.

Obtaining a set of basic data on the process of true cold fission represented by events revealed in bands taken with 1.5 MeV steps in the plots giving the TKE values measured for the specific fragment masses. The results, the fragment charge and mass splits revealed as the true cold fission, the proton/neutron even-odd effects, and energy spectra populated in pairs of fragments, will shed light on the shell structures making cold fission competitive.

Measurements of angular correlations of prompt γ-ray emission with the fission axis. The resolution of the fission axis for the chamber will be 3° and angular correlations of the γ-ray observations by the Gammasphere will be processed by software previously developed for angular correlations [58]. These measurements will be used for important band and level spin assignments and confirmations. Furthermore, one can obtain new insights into level schemes of Pr-Sm and Gd-Se nuclei, still further from stability, via narrow bins in mass asymmetry and the coincident γ-ray spectra.

6.3 Methods

We propose to study ^{252}Cf spontaneous fission using the Gammasphere and a new fission fragment TKE chamber, the design of which is complete and the electronics already procured. The chamber establishes TKE via Time-of-Flight (TOF) and identifies the fission

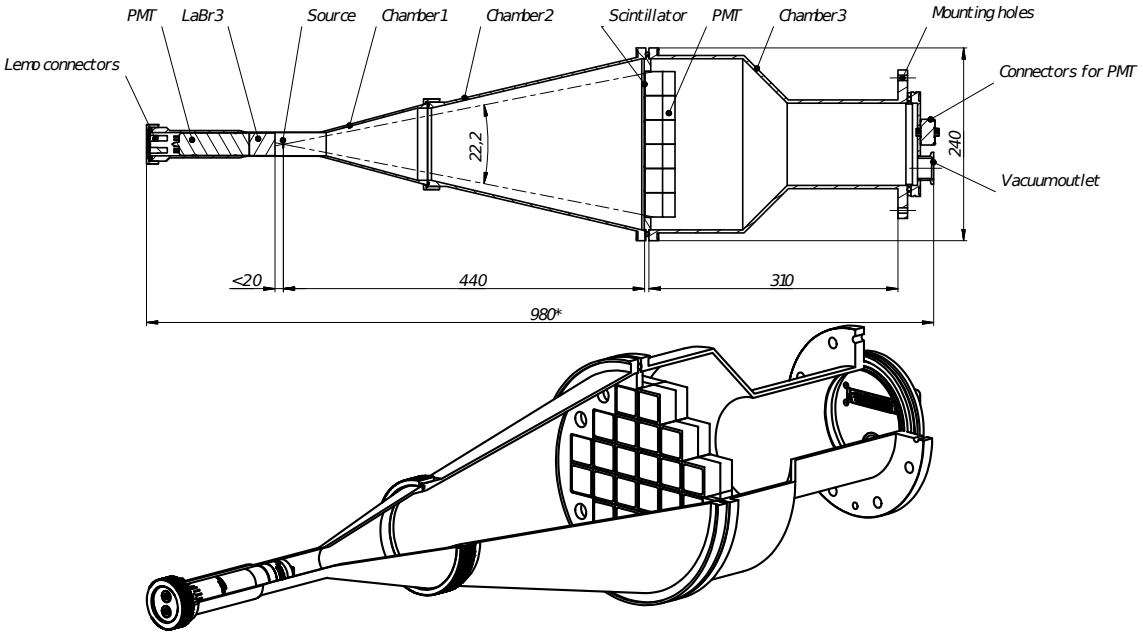

Figure 6.1: Sketch of the proposed Fission Dynamics Chamber.

axis with a precision of 3°. The TKE chamber is designed with respect to the inner cavity of the Gammasphere, design shown in Figures 6.1 , and the materials and dimensions to be used were recently tested for TOF resolution and efficiency at the JINR in Dubna, Russia.

The chamber will house a ^{252}Cf source deposited on a 10 μm platinum backing and placed at a distance of 19 mm from a LaBr3 scintillator and 400 mm from an array of plastic scintillators. The source diameter will be 5 mm and the open side of the source will not be covered as covering material causes energy loss of the moving fragments but does not fully prevent sputtering. Sputtering is a process by which fragments of the source material are knocked free of the backing by energetic reactions following a decay event. This source setup will result in one of the fission fragments being stopped in the source backing while the other flies freely towards an array of plastic detectors. The motion of the unstopped fragment will require their γ-rays detected by the Gammasphere to be Doppler corrected. With complete data from the TKE chamber of flight time and fission axis, the estimated overall energy resolution (FWHM) obtained after Doppler correction is 3.5 and 5.0 keV for 500 and 1000 keV γ-rays, respectively, 2.5 keV is typical for the Gammasphere germanium detectors for 200 - 1000 keV γ-rays from static sources. The LaBr3 crystal is a scintillator with good response time and efficiency and will be used to obtain a start signal via the observation of the prompt γ-rays following a fission event. For a 25.4 mm diameter, 76.2 mm length LaBr3 crystal at a distance of 19 mm from the source, such a start signal will be obtained for 35(1)% of the fission events. The stop detectors are a square plastic scintillator 0.025 mm thick and 20 mm on a side mounted on a dedicated PMT. An array of 24 such detectors will be placed at a distance of 400 mm from the source. Their size and distribution will enable the fission axis to be defined to within three degrees. The solid angle covered by the array of stop detectors will be $\approx$0.06 sr. With the given coverage of the stop signal array, for which the efficiency for fission fragment detection is effectively 100%, and the efficiency of the start signal, the expected counts per kBq(SF) second is $\approx$3.3. The timing RMS error for this setup will be $\approx$180 ps yielding a RMS error in the

fragment velocity of ≈0.5%. The chamber will need to be pumped down to 0.001 mbar via the vacuum port located behind the array of plastic scintillators. It is the opinion of our collaboration that the given resources and their capabilities are sufficient to achieve the goals of this experiment.

The detection of γ-rays emitted at the spontaneous fission of ^{252}Cf by the Gammasphere array will be triggered by the coincidence of signals coming from the LaBr3 and plastic scintillators. The data treatment will follow those methods described in references [55] and will yield detailed γ-γ coincidence spectra built for different bands taken in the measured spectrum of fragment TOF. The TOF bandwidths will define the widths of the TKE bands. The positions of these bands on the TKE scale will be defined separately for different charge splits. The analysis of the so built γ-γ coincidence spectra will reveal numerous individual peaks of characteristic γ rays emitted in coincidence by the fragment pairs, and the yields of these secondary fragment pairs will be deduced from the count rates measured for the γ-γ peaks.

Yield patterns obtained for the individual secondary fragment pairs in different TKE bands will be used to extract the primary fragment distributions by unfolding the experimental data. The unfolding procedure used, based on the least squares method, is described in detail in the following references: *et al.* [55, 58]. The mean TKE value, its variance σ_{TKE}, the mean mass value of heavy primary fragments, A_H^{mean}, the mass variance σ_{AH}, and the mean excitation-energy values of heavy and light primary fragment E_{th}^H and E_{th}^L will also be determined.

Appendix A

Appendix: Onset of Deformation

In 1950 Rainwater [12] proposed that a spheroidal nuclear shape would be more stable than a spherical shape for the description of nuclei as they move away from closed shell values. Rainwater argued that the entirety of the nucleus is reformed into a self consistent spheroidal box in response to the addition of the next nucleon, not only the orbit of that nucleon. At that time, there was already evidence of such deformation in the rare earth and heavy mass regions. Evidence for stable deformation of the mass A≈110 region was later observed by Johansson in 1965 [59]. Later in 1970, measurements by Cheifetz, *et al.* [60] refined the region of stable deformation in light isotopes to A≈100 in response to theoretical predictions by Ragnarsson and Nilsson [61] and Arseniev, *et al.* [62]. These calculations suggested the existence of additional deformed nuclei lighter than those in the rare earth and heavy element region. Since the late 1940s, numerous studies have been done to investigate the mechanisms of deformation. Of interest to this proposal are those focusing on the onset of deformation.

As a lower border to the region of rapid onset of deformation, Albers, *et al.* [63] demonstrated smooth onset of deformation for the neutron-rich Kr isotopes. Additionally, in 2015 Sotty, *et al.* [64] posited ^{97}Rb as the cornerstone of deformation in the A≈100 region. The A≈100 region of deformation is well highlighted by the shift in 2 neutron separation energy and difference in mean-square charge radii detaled by Naimi, *et al.* [65] in 2010. The A≈100 region of interest can be seen in the non-linear behavior of nucleon separation energies and nuclear charge radius near N=60.

Federman and Pittel (1979) [66] modeled deformation in the A≈100 region via a unified shell-model where by the Hartree-Fock-Bogoliubov and shell methods they ascribe deformation in the region to neutron proton interactions. They stipulate, however, that such

interactions would likely be less important for nuclei of the rare earth and transuranic regions. Hamilton, *et al.* [67] attributed the sudden onset of deformation to proton shell gaps reinforcing deformation due to neutron shell gaps at the same deformation. In the region of A≈100, this corresponds to a deformed shell gap at Z=38 reinforcing a deformed shell gap at N=60. They further point out that this reinforcing behavior drops off rapidly as either nucleon number moves away from Z=38, N=60. More recently Otsuka, *et al.* [68] argued a case for neutron proton interactions driving deformation via the tensor force. A result of this approach was the prediction of the increasing of the energy of the centroid of the $1h_{11/2}$ neutron shell. In 2008 Verma, *et al.* [69] argued that in their projected shell model study of strontium and zirconium near A≈100 the mechanisms of rapid onset or deformation are worked out for N=60, taking into account both neutron proton interactions and intruder orbitals. Verma, *et al.* [69] ascribed the development of deformation to four aspects, the simultaneous polarization of $2p_{1/2}$, $2p_{3/2}$, and $1f_{5/2}$ proton orbits, the sharp increase in $g_{9/2}$ proton occupation as N goes from 58 to 60, the occupation of low K components of $1h_{11/2}$ and $2f_{7/2}$ neutron orbits and the $2d_{5/2}$ and $1g_{7/2}$ neutron subshells being less than half full.

In the process of deformation, intruder/extruder energy levels are observed in the structure of the nucleus. The term intruder/extruder here referring to a single particle energy level of a deformed shell model, which has either intruded into the ordering of lower energy levels or extruded up into higher energy levels. Down sloping energy levels are interpreted as deformation-driving states while upward sloping energy levels are interpreted as spherical-driving states.

In 1974 Kleinheinz, *et al.* [36] proposed that intruder/extruder states explain the onset of deformation near A≈150. Kleinheinz reasoned that the transitioning of a neutron in the spherical-driving $11/2^-[505]$ state into the deformation-driving $i_{13/2}$ orbital results in shape coexistence in the odd-A nucleus of ^{151}Gd. Urban, *et al.* [70] investigated an $11/2^-[505]$ neutron extruder state in ^{159}Sm in comparison with systematics of several nearby A≈150 nuclei with $11/2^-[505]$ neutron extruder states to extend the description of deformation

onset as related to extruder states. Previous to their 2009 work, Urban, *et al.* investigated the $9/2^{+}[404]$ neutron extruder state in the A≈100 region identifying such states in ^{99}Zr and ^{101}Zr [37]. They relate these zirconium states to an observed extruder state in ^{97}Sr by Hwang, *et al.* [38].

Finding that while ^{99,101}Zr and ^{97}Sr continue to highlight the role of the extruder state in resisting deformation, resulting in a sudden onset of deformation when the extruder state is vacated, the onset in strontium is more rapid than that of the onset in zirconium. No conclusive explanation has yet been given describing why the rate of deformation differs between ^{99,101}Zr and ^{97}Sr. Intruder states have also been ascribed to some of the rapid onset near N=60 as detailed above in the work of Verma, *et al.* [69] and by Lhersonneau, *et al.* [71] who identifed the $\nu 3/2^{-}[541]$ state in the structure of ^{99}Zr. Further studies on intruder states in the A≈100 region also include Rzca-Urban, *et al.*s 2009 work [72] identifying excitations involving the $\nu(g_{7/2}, h_{11/2})$ configuration, with the goal of improving calculations of the energy of the centroid of the $1h_{11/2}$ neutron shell.

Throughout the descriptions of the onset of deformation in the mass A≈100 and A≈160 regions the excitation energy of intruder/extruder states are key pieces of structural information. While there exists additional unobserved intruder/extruder states in neutron rich nuclei, they belong to more exotic and therefore, less studied structures. So long as the study of the shape defining qualities of the A≈100 and A≈160 region continue, the need for direct observations of detailed nuclear structure will persist.

Appendix B

Appendix: Command Files

Throughout this work, the ability to issue commands via pre-written macros, or command files in the DAMM software tool set, has been of great value. What follows are examples of the two primary command sequences used. The first is a short process by which a spectra is called and a background spectra is created to subtract from the spectra of interest. By using this dynamic background subtraction method, the gates which were chosen to represent background could be adjusted in the event they were corresponding to coincident transitions and ensuring that contributions from contaminant isotopes in the beam were removed from the analysis. To ensure that this gate based background subtraction method did not introduce bias or otherwise obscure transitions that should be visible within the data, both the spectra of interest and the background spectra are displayed in overlay at the same time the corrected spectra is displayed. While syntax will vary with software, Figure B.1 shows the method of background subtraction used with the version of DAMM implemented in this analysis.

The second command file is one of the files used for evaluation of the relative transition intensities. A number of stops are built into this code to allow the user to visually check that each fit conforms to the peak it is meant to, as the auto fit may not always converge to the desired peak. Output following this command file could then be imported into any spreadsheet software and the necessary calculations for establishing the relative intensities carried out.

As coincidence analysis is ultimately about forming logical relationships between transitions observed within a given nucleus, it can often be very important that a researcher have access not only to the knowledge that previous researchers observed specific coincidence relationships but also be able to review those spectra that lead to that relationship.

```
in 30Tick_A163_LDF3and4.his
fig 12
win 1
gx 1680 40 40
swap
gx 1680 46 46
a12
gx 1680 44 45

d m 1 2
dl 20 600
d

win 2
swap
a12 -1
d m 2
dl 20 600
d
```

Figure B.1: Example Command file for DAMM to create a set of spectra, background subtracted gate and gate with background overlay.

```
in 30TickTimes2_LDF3and4only.his
fig 11
pzot
T=2000
mult=2
Gate=96
Width=1
VARL1=Gate*mult-width
VARH1=Gate*mult+width
gx 1680 VARL1 VARH1
pk 144
pk 150
pk 152
fit m 1 140 155
Wait T
pzot
pk 383
pk 427
fit m 1 370 450
Wait T
pzot
pk 801
fit m 1 780 820
wait T
pzot
pk 951
fit m 1 920 980
Wait T
```

Figure B.2: Example Command file for DAMM to calculate peak areas for a selection of peaks coincident with the 96 keV transition.

Thus, the primary drive for use of these command files was reproducibility, as they allow any other person with access to the data to view the same spectra and fits that were used during this analysis. While both RADWARE and DAMM allow for dynamic command by command gating to be done, it is easy for even the person doing the bulk of the analysis to forget key projections without careful note taking. The use of these command files ensure that not only is the analysis well documented but any other user could quickly review and implement these gates themselves.

BIBLIOGRAPHY

[1] J. H. Hamilton, S. H. Liu, N. T. Brewer, Y. X. Luo, J. O. Rasmussen, S. J. Zhu, and R. Donangelo. New vistas from nuclei far from stability. *Phys. Rev. C*, 82:034308, Sep 2010.

[2] E. M. Burbidge, G. R. Burbidge, W. A. Fowler, and F. Hoyle. Synthesis of the elements in stars. *Rev. Mod. Phys.*, 29:547–650, Oct 1957.

[3] J. J. Cowan, F. Thielemann, and J. W. Truran. The r-process and nucleochronology. *Physics Reports*, 208(4):267 – 394, 1991.

[4] R. Surman, J. Engel, J. R. Bennett, and B. S. Meyer. Source of the rare-earth element peak in *r*-process nucleosynthesis. *Phys. Rev. Lett.*, 79:1809–1812, Sep 1997.

[5] Nathan T. Brewer. *Measurements of the Prompt and Delayed Radiation from Fission Fragments: Deformation Properties of Neutron Rich Nuclei*. PhD thesis, Vanderbilt University, 2013.

[6] R. B. Firestone and V. S. Shirley. Table of isotopes, 2 volume set. *Table of Isotopes, 2 Volume Set, by Richard B. Firestone, Virginia S. Shirley (Editor), pp. 3168. ISBN 0-471-33056-6. Wiley-VCH, December 1998.*, page 3168, 1998.

[7] W. Elsasser. *J. De Phys. Et Rad.*, 5:625, 1934.

[8] M. G. Mayer. On closed shells in nuclei. *Phys. Rev.*, 74:235–239, Aug 1948.

[9] Maria Goeppert Mayer and J. Hans D. Jensen. *Elementary theory of nuclear shell structure*. Wiley, 1955.

[10] M. G. Mayer. Nuclear configurations in the spin-orbit coupling model. i. empirical evidence. *Phys. Rev.*, 78:16–21, Apr 1950.

[11] O. Haxel, J. H. D. Jensen, and H. E. Suess. Modellmäßige deutung der ausgezeichneten nukleonenzahlen im kernbau. *Zeitschrift für Physik*, 128(2):295–311, Apr 1950.

[12] J. Rainwater. Nuclear energy level argument for a spheroidal nuclear model. *Phys. Rev.*, 79:432–434, Aug 1950.

[13] Kai Siegbahn. *Alpha-, beta-and gamma-ray spectroscopy*. Elsevier, 2012.

[14] Fujia Yang and Joseph H Hamilton. *Modern Atomic and Nuclear Physics: Revised*. World Scientific Publishing Company, 2010.

[15] T. Bengtsson and I. Ragnarsson. Rotational bands and particle-hole excitations at very high spin. *Nuclear Physics A*, 436(1):14 – 82, 1985.

[16] M. Matsuda T. K. Sato S. Jeong A. Osa, S. Ichikawa. Ion source development for the on-line isotope separator at jaea. *Nuclear Instruments and Methods in Physics Research Section B: Beam Interactions with Materials and Atoms*, 266:4394–4397, 2008.

[17] K. Tsukada M. Asai H. Hayashi Y. Kojima M. Shibata T. K. Sato, A. Osa and S. Ichikawa. Jaea-review 2006-029. page P31, 2006.

[18] J. D. Baker R. J. Gehrke, R. C. Greenwood and D. H. Mekrantz. Advanced system for separation of rare-earth fission products. *Journal of Radioanalytical and Nuclear Chemistry*, 74(1-2):117–124, 1982.

[19] R. Grzywacz. Applications of digital pulse processing in nuclear spectroscopy. *Nuclear Instruments and Methods in Physics Research Section B: Beam Interactions with Materials and Atoms*, 204:649–659, 2003. 14th International Conference on Electromagnetic Isotope Separators and Techniques Related to their Applications.

[20] Display, analysis and manipulation module (damm) in the upak distribution from: ftp://ftp.phy.ornl.gov/pub/upak/ accessed 2019.

[21] D. C. Radford. Escl8r and levit8r: Software for interactive graphical analysis of hpge coincidence data sets. *Nuclear Instruments and Methods in Physics Research Section A: Accelerators, Spectrometers, Detectors and Associated Equipment*, 361:297–305, 1995.

[22] J. M. Allmond. Priv. comm.

[23] H. Hayashi, Y. Akita, O. Suematsu, M. Shibata, M. Asai, T. K. Sato, S. Ichikawa, I. Nishinaka, Y. Nagame, A. Osa, K. Tsukada, T. Ishii, Y. Kojima, and A. Taniguchi. Qβ measurements of 158, 159pm , 159, 161sm , 160-165eu , 163gd and 166tb using a total absorption bgo detector. *The European Physical Journal A*, 34(4):363–370, Dec 2007.

[24] R. K. Sheline, W. N. Shelton, H. T. Motz, and R. E. Carter. Energy levels of dy^{165}. *Phys. Rev.*, 136:B351–B365, Oct 1964.

[25] A. K. Jain, A. Ghosh, and B. Singh. Nuclear data sheets for a = 165. *Nuclear Data Sheets*, 107(5):1075 – 1346, 2006.

[26] W. N. Shelton and R. K. Sheline. Levels in ^{164}dy from deuteron stripping and inelastic proton scattering experiments. *Phys. Rev.*, 133:B624–B631, Feb 1964.

[27] R. C. Greenwood, R. J. Gehrke, J. D. Baker, D. H. Meikrantz, and C. W. Reich. Identification of a new isotope, ^{165}Tb. *Phys. Rev. C*, 27:1266–1270, Mar 1983.

[28] E. Kaerts, P. H. M. van Assche, S. A. Kerr, F. Hoyler, H. G. Börner, R. F. Casten, and D. D. Warner. A study of the low-energy level structure of ^{165}dy. *Nuclear Physics A*, 514(2):173–224, 1990.

[29] H. Nabielek. *Untersuchung von Obergangsraten Elektromagnetischer Ubergange durch Messung der Lebensdauer Angeregter Kernniveaus nach Neutroneneinfang*. Physikinstitut, Reaktorzentrum Seibersdorf, Austria; SGAE-PH-78/1968, 1968.

[30] K. Alder and R. M. Steffen. Emission and absorption of electromagnetic radiation. In *The electromagnetic interaction in nuclear spectroscopy*. 1975.

[31] J. H. Hamilton. Priv. comm.

[32] E. H. Wang. Priv. comm.

[33] P.E. Garrett and D.G. Burke. Nuclear structure of ^{159}tb, ^{161}tb and ^{163}tb studied with the (t,) reaction. *Nuclear Physics A*, 550(1):1–20, 1992.

[34] E. R. Sugarbaker. *Proton Intrinsic States in ^{153}Pm, ^{163}Tb, and ^{169}Ho Studied via the (d,^{3}He) Reaction*. PhD thesis, University of Michigan, 1976.

[35] Glenn F. Knoll. *Radiation detection and measurement*. John Wiley & Sons, 2000.

[36] P. Kleinheinz, R. K. Sheline, M. R. Maier, R. M. Diamond, and F. S. Stephens. Shape coexistence and its cause in ^{151}Gd. *Phys. Rev. Lett.*, 32:68–71, Jan 1974.

[37] W. Urban, J. A. Pinston, J. Genevey, T. Rzaca-Urban, A. Złomaniec, G. Simpson, J. L. Durell, W. R. Phillips, A. G. Smith, B. J. Varley, I. Ahmad, and N. Schulz. The $\nu 9/2[404]$ orbital and the deformation in the a 100 region. *The European Physical Journal A - Hadrons and Nuclei*, 22(2):41–252, Nov 2004.

[38] J. K. Hwang, A. V. Ramayya, J. H. Hamilton, D. Fong, C. J. Beyer, P. M. Gore, Y. X. Luo, J. O. Rasmussen, S. C. Wu, I. Y. Lee, C. M. Folden, P. Fallon, P. Zielinski, K. E. Gregorich, A. O. Macchiavelli, M. A. Stoyer, S. J. Asztalos, T. N. Ginter, S. J. Zhu, J. D. Cole, G. M. Ter Akopian, Yu. Ts. Oganessian, and R. Donangelo. Identification of $\nu 9/2[404]$ band in ^{97}Sr. *Phys. Rev. C*, 67:054304, May 2003.

[39] Enhong Wang. *Studies of Neutron-Rich Nuclei From ^{252}Cf and ^{238}U+^{9}Be Fission Fragments*. PhD thesis, Vanderbilt University, 2015.

[40] Y. X. Luo, J. O. Rasmussen, A. V. Ramayya, J. H. Hamilton, X. Q. Zhang, J. K. Hwang, C. J. Beyer, J. Kormicki, G. M. Ter-Akopian, Yu. Ts. Oganessian, A. V. Daniel, K. E. Gregorich, T. N. Ginter, P. Zielinski, C. M. Folden, I. Y. Lee, P. Fallon, A. Macchiavelli, R. Donangelo, M. A. Stoyer, S. Asztalos, and S. C. Wu. Fission γ spectra and levels in ^{139}Ba. *Phys. Rev. C*, 64:054306, Oct 2001.

[41] K. Schreckenbach, A.I. Namenson, W.F. Davidson, T. Von Egidy, H.G. Brner, J.A. Pinston, R.K. Smither, D.D. Warner, R.F. Casten, M.L. Stelts, D.H. White, and W. Stffl. Rotational-vibrational band structure in 155sm. *Nuclear Physics A*, 376(2):149–182, 1982.

[42] N. T. Brewer. Priv. comm. regarding ^{159}sm studies out for publication.

[43] A. Staszczak, J. Dobaczewski, and W. Nazarewicz. *Acta Phys. Pol. B*, 38:1589, 2007.

[44] J. C. Pei, M. V. Stoitsov, G. I. Fann, W. Nazarewicz, N. Schunck, and F. R. Xu. Deformed coordinate-space hartree-fock-bogoliubov approach to weakly bound nuclei and large deformations. *Phys. Rev. C*, 78:064306, Dec 2008.

[45] J. Erler, P. Kluepfel, P.-G. Reinhard, and J. A. Maruhn. Systematics of collective correlation energies from self-consistent mean-field calculations. *The European Physical Journal A*, 37(3):343–355, 2008.

[46] R. K. Gupta, M. Balasubramaniam, C. Mazzocchi, M. La Commara, and Werner Scheid. Decay of excited ^{116}ba* formed in the ^{58}Ni+^{58}Ni reaction via the emission of intermediate mass fragments. *Phys. Rev. C*, 65:024601, Jan 2002.

[47] O. Litaize, O. Serot, and L. Berge. Fission modelling with fifrelin. *The European Physical Journal A*, 51(12):177, Dec 2015.

[48] K.-H. Schmidt, B. Jurado, C. Amouroux, and C. Schmitt. General description of fission observables: Gef model code. *Nuclear Data Sheets*, 131:107–221, 2016.

[49] F. Ivanyuk, F.-J. Hambsch, and N. Carjan. Scission-point model predictions of fission-fragment mass and total kinetic energy distributions for 236u and 252cf. In *EPJ Web of Conferences*, volume 146, page 04055. EDP Sciences, 2017.

[50] A. Tudora, F. Hambsch, and G. Giubega. Particular aspects related to the even-odd effects in prompt emission. *The European Physical Journal A*, 52(6):182, 2016.

[51] W. M. Gibson T. D. Thomas and G. J. Safford. *Proceedings of Symposium Physics and Chemistry of Fission, Vol. 1*. Vienna: IAEA, 1966.

[52] F. Gonnenwein. Even-odd effects of fragment yields in low energy fission. *Physics Procedia*, 47:107–114, 2013.

[53] A. Göök, F.-J. Hambsch, and M. Vidali. Prompt neutron multiplicity in correlation with fragments from spontaneous fission of ^{252}Cf. *Phys. Rev. C*, 90:064611, Dec 2014.

[54] J. H. Hamilton, A. V. Ramayya, J. Kormicki, W.-C. Ma, Q. Lu, D. Shi, J. K. Deng, S. J. Zhu, A. Sandulescu, W. Greiner, G. M. Ter Akopian, Y. T. Oganessian, G. S. Popeko, A. V. Daniel, J. Kliman, V. Polhorsky, M. Morhac, J. D. Cole, R. Aryaeinejad, I. Y. Lee, N. R. Johnson, and F. K. McGowan. Zero neutron emission in spontaneous fission of ^{252}Cf: a form of cluster radioactivity. *Journal of Physics G Nuclear Physics*, 20:L85–L89, August 1994.

[55] G. M. Ter-Akopian, J. H. Hamilton, Yu. Ts. Oganessian, A. V. Daniel, J. Kormicki, A. V. Ramayya, G. S. Popeko, B. R. S. Babu, Q.-H. Lu, K. Butler-Moore, W.-C. Ma, E. F. Jones, J. K. Deng, D. Shi, J. Kliman, M. Morháč, J. D. Cole, R. Aryaeinejad, N. R. Johnson, I. Y. Lee, and F. K. McGowan. Yields of correlated fragment pairs in spontaneous fission of ^{252}cf. *Phys. Rev. C*, 55:1146–1161, Mar 1997.

[56] F.-J. Hambsch, H.-H. Knitter, and C. Budtz-Jrgensen. The positive odd-even effects observed in cold fragmentation are they real? *Nuclear Physics A*, 554(2):209–222, 1993.

[57] C. J. Zachary, J. H. Hamilton, E. Wang, G. Ter-Akopian, and Yu. Ts. Oganessian. Talk presented to the int. symp. exon-2018.

[58] A.V. Daniel, C. Goodin, K. Li, A.V. Ramayya, N.J. Stone, J.K. Hwang, J.H. Hamilton, J.R. Stone, Y.X. Luo, J.O. Rasmussen, M.A. Stoyer, S.J. Zhu, G.M. Ter-Akopian, and I.Y. Lee. Technique for measuring angular correlations and g-factors of excited states with large multi-detector arrays: An application to neutron rich nuclei produced by the spontaneous fission of 252cf. *uclear Instruments and Methods in Physics Research Section B: Beam Interactions with Materials and Atoms*, 262(2):399–406, 2007.

[59] S. A. E. Johansson. Gamma de-excitation of fission fragments: (ii). delayed radiation. *Nuclear Physics*, 64(1):147–160, 1965.

[60] E. Cheifetz, R. C. Jared, S. G. Thompson, and J. B. Wilhelmy. Experimental information concerning deformation of neutron rich nuclei in the $a \sim 100$ region. *Phys. Rev. Lett.*, 25:38–43, Jul 1970.

[61] I. Ragnarsson and S. G. Nilsson. Private communications to e. cheifetz.

[62] D. A. Arseniev, A. Sobiczewski, and V. G. Soloviev. Equilibrium deformations of neutron-rich nuclei in the a 100 region. *Nuclear Physics A*, 139(2):269–276, 1969.

[63] M. Albers, N. Warr, K. Nomura, A. Blazhev, J. Jolie, D. Mücher, B. Bastin, C. Bauer, C. Bernards, L. Bettermann, V. Bildstein, J. Butterworth, M. Cappellazzo, J. Cederkäll, D. Cline, I. Darby, S. Das Gupta, J. M. Daugas, T. Davinson, H. De Witte, J. Diriken, D. Filipescu, E. Fiori, C. Fransen, L. P. Gaffney, G. Georgiev, R. Gernhäuser, M. Hackstein, S. Heinze, H. Hess, M. Huyse, D. Jenkins, J. Konki,

M. Kowalczyk, T. Kröll, R. Krücken, J. Litzinger, R. Lutter, N. Marginean, C. Mihai, K. Moschner, P. Napiorkowski, B. S. Nara Singh, K. Nowak, T. Otsuka, J. Pakarinen, M. Pfeiffer, D. Radeck, P. Reiter, S. Rigby, L. M. Robledo, R. Rodríguez-Guzmán, M. Rudigier, P. Sarriguren, M. Scheck, M. Seidlitz, B. Siebeck, G. Simpson, P. Thöle, T. Thomas, J. Van de Walle, P. Van Duppen, M. Vermeulen, D. Voulot, R. Wadsworth, F. Wenander, K. Wimmer, K. O. Zell, and M. Zielinska. Erratum: Evidence for a smooth onset of deformation in the neutron-rich kr isotopes [phys. rev. lett. 108, 062701 (2012)]. *Phys. Rev. Lett.*, 109:209904, Nov 2012.

[64] C. Sotty, M. Zielińska, G. Georgiev, D. L. Balabanski, A. E. Stuchbery, A. Blazhev, N. Bree, R. Chevrier, S. Das Gupta, J. M. Daugas, T. Davinson, H. De Witte, J. Diriken, L. P. Gaffney, K. Geibel, K. Hadyńska-Klęk, F. G. Kondev, J. Konki, T. Kröll, P. Morel, P. Napiorkowski, J. Pakarinen, P. Reiter, M. Scheck, M. Seidlitz, B. Siebeck, G. Simpson, H. Törnqvist, N. Warr, and F. Wenander. $^{97}_{37}\mathrm{Rb}_{60}$: The cornerstone of the region of deformation around $a \sim 100$. *Phys. Rev. Lett.*, 115:172501, Oct 2015.

[65] S. Naimi, G. Audi, D. Beck, K. Blaum, Ch. Böhm, Ch. Borgmann, M. Breitenfeldt, S. George, F. Herfurth, A. Herlert, M. Kowalska, S. Kreim, D. Lunney, D. Neidherr, M. Rosenbusch, S. Schwarz, L. Schweikhard, and K. Zuber. Critical-point boundary for the nuclear quantum phase transition near $a = 100$ from mass measurements of ^{96,97}Kr. *Phys. Rev. Lett.*, 105:032502, Jul 2010.

[66] P. Federman and S. Pittel. Unified shell-model description of nuclear deformation. *Phys. Rev. C*, 20:820–829, Aug 1979.

[67] J. H. Hamilton, A. V. Ramayya, C. F. Maguire, R. B. Piercey, R. Bengtsson, P. Moller, J. R. Nix, Jing-ye Zhuang, R. L. Robinson, and S. Frauendorf. Effects of reinforcing shell gaps in the competition between spherical and highly deformed shapes. *Journal of Physics G: Nuclear Physics*, 10(5):L87–L91, May 1984.

[68] T. Otsuka, T. Suzuki, R. Fujimoto, H. Grawe, and Y. Akaishi. Evolution of nuclear shells due to the tensor force. *Phys. Rev. Lett.*, 95:232502, Nov 2005.

[69] S. Verma, P. A. Dar, and R. Devi. Projected shell model study of neutron-rich deformed isotopes of sr and zr. *Phys. Rev. C*, 77:024308, Feb 2008.

[70] W. Urban, J. A. Pinston, G. S. Simpson, A. G. Smith, J. F. Smith, T. Rzaca-Urban, and I. Ahmad. The $11/2^-[505]$ neutron extruder orbital in ^{159}Sm. *Phys. Rev. C*, 80:037301, Sep 2009.

[71] G. Lhersonneau, B. Pfeiffer, K.-L. Kratz, T. Enqvist, P. P. Jauho, A. Jokinen, J. Kantele, M. Leino, J. M. Parmonen, H. Penttilä, and J. Äystö. Evolution of deformation in the neutron-rich zr region from excited intruder state to the ground state. *Phys. Rev. C*, 49:1379–1390, Mar 1994.

[72] T. Rzaca-Urban, K. Sieja, W. Urban, F. Nowacki, J. L. Durell, A. G. Smith, and I. Ahmad. $(h_{11/2}, g_{7/2})_{9^-}$ neutron excitation in ^{92,94,96}Sr. *Phys. Rev. C*, 79:024319, Feb 2009.